



FIZINIŲ IR
TECHNOLOGIJOS MOKSLŲ
CENTRAS

14

FIZINIŲ IR TECHNOLOGIJOS
MOKSLŲ CENTRO

DOKTORANTŲ IR
JAUNUJŲ MOKSLININKŲ

KONFERENCIJOS TEZĖS

2024 m. spalio 15-17 d.



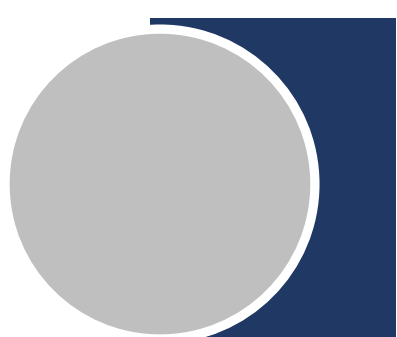
TURINYS

CONTENTS

-
- O1** **Gitana Valeckytė.** Nikelio ir jo lydinių cheminis nusodinimas ir taikymas.
- O2** **Yaroslau Padrez.** Machine learning algorithms for thyroid cancer diagnosis based on second harmonic generation microscopy.
- O3** **Sukomol Barua.** Bimetallic 3D Nickel-Manganese Coatings: High-performance HER and Stable OER Electrocatalysts for Alkaline Water Splitting and Overall Seawater Splitting.
- O4** **Virginija Ulevičienė.** Hidrazino oksidacijos ant Nikeliu ir Azotu legiruotų anglies katalizatorių tyrimas.
- O5** **Huma Amber.** Electrocatalytic performance of cobalt-phosphorus catalyst for overall water splitting in alkaline media.
- O6** **Pamela Rivera Rivera.** Bismuth Plated Laser-Induced (Bi-LIG) Graphene Electrochemical Sensor for Zinc Detection in Plant Tissues.
- O7** **Mohamed Abdelkader Fawzy Abdelkader.** From equations to neural networks: the application of physics-informed neural networks (PINNs) to electrochemical sensor microarray modelling.
- O8** **Viktorija Reinikovaitė.** Microbial and electrochemical characterization of individual granules for fixed bed electrodes in microbial electrochemical technologies
- O9** **Greta Kasputė.** Essential oils as components of drug delivery systems: electrochemical studies.
- O10** **Enayat Mohsenzadeh.** Optimised Molecularly Imprinted Polymer for detection of salicylic acid by DFT and Molecular Mechanics calculations.
- O11** **Greta Pilvenytė.** MIP formavimas polipirolo pagrindu.
- O12** **Gyautė Sirgėdaitė.** Plazmoninių dalelių sintezė biologinių molekulių SERS nustatymui.
- O13** **Greta Zambžickaitė.** Magnetito nanodalelių sintezė ir dekoravimas sidabro nanodalelėmis.
- O14** **Ilya Navitski.** Electrochemical detection of cadmium ions in aqueous solutions using MXene-based sensor.
- O15** **Kristina Mikalauskienė.** Development of the Compton-to-peak methodology for the analyze of gamma spectra for the characterisation of metallic radioactive wastes.
- O16** **Mahrosh Javed.** Development of chitosan-graphene oxide-based nanocomposites for removal of nano- and micro-plastics from fresh water.
- O17** **Abdullah Khan.** The role and potential of green infrastructure in filtering transport-generated microplastics.
- O18** **Sonata Pleskytė.** Application of TiO₂-based nanocomposites for the photocatalytic degradation of LDPE microplastics.
- O19** **Agnė Minderytė.** The role of the sea transport for submicron aerosol chemical composition.
- O20** **Vita Petrikaitė.** KCl slenkstinių koncentracijos ribų tyrimas lazerinėje nanodalelių generacijoje, siekiant pagerinti stabilumą ir SERS stiprinimą.
- O21** **Kernius Vilkevičius.** Lazeriu suformuotų nanodarinių morfologinis valdymas paviršiumi sustiprintai Ramano spektroskopijai.
- O22** **Daria Astrauskytė.** Skaidrinančių dangų formavimas ant 3D mikrooptinų komponentų naudojant atominių sluoksnių nusodinimo technologiją.

- O23** **Aivaras Kazakevičius.** Nonlinear heat distribution in high average power end-pumped Yb:YAG active medium amplifiers and its effect on depolarization.
- O24** **Miglė Mackevičiūtė.** Soda-lime stiklo apdirbimas lazeriu nuo apatinės bandinio pusės pasitelkiant GHz papliupų režimą.
- O25** **Laimis Zubauskas.** Lydyto kvarco abliacijos efektyvumo didinimas naudojant papliupų režimą.
- O26** **Modestas Sadauskas.** Lazeriu asistuotas vario mikrotakeliu nusodinimas ant dielektriko paviršiaus.
- O27** **Jaroslav Kodz.** Sanjako efektu pagrįstas optinis izoliatorius skirtas plataus spektro šviesai.
- O28** **Ignas Bitinaitis.** Reactive magnetron sputtering of Sr₂FeMoO₆ film.
- O29** **Greta Tartėnė.** The role of cell wall in organic-solvent lipid extraction from oleaginous yeasts assisted by Pulsed Electric Fields.
- O30** **Tomas Mockaitis.** MFC Efficiency with E. meliloti and Redox Mediators.
- O31** **Laisvidas Striška.** Sensing mechanical properties by AFM: comparative analysis of polymer samples.
- O32** **Tadas Jelinskas.** Atominių jėgų mikroskopijos metodikos lastelių struktūriniams ir viskoelastinių savybių tyrimams bioimitacinėse aplinkose.
- O33** **Artūras Polita.** Aplinkai jautrių fluorescuojančių BODIPY jutiklių kūrimas ligų detekcijai.
- O34** **Ivan Halimski.** Fluorescence concentration quenching in solutions of Zinc- and Free Base Phthalocyanines.
- O35** **Mohammad Esmaeil Daraei.** Optoelectronic Simulation of Conventional and Plasmonic Photoconductive Antennas based on Finite Element Method (FEM).
- O36** **Ihor Krapivin.** Application of Terahertz Time-Domain Spectroscopy for Observation Of Polymer Curing Chemical Reactions.
- O37** **Maxim Moscotin.** Modified EdgeFET design for sensitive room-temperature terahertz detection.
- O38** **Lukas Stakėla.** Supergardelės plazmoninių tikrinių modų ypatybės Blocho stiprinimo režime.
- O39** **Barbora Škélaitė.** Terahertz Spectroscopy of Rectangular Metasurfaces Formed on n-GaAs/GaAs Structures.
- O40** **Karolis Daugevičius.** Aperture photometry limits in star cluster studies.
- O41** **Eimantas Kriščiūnas.** Star clusters in the disk of Andromeda galaxy.
- O42** **Pavel Piatrou.** Magnetic field dynamics during magnetic pulse forming and crimping.
- O43** **Povilas Jurkšaitis.** Paviršinio plazmono ir r6g eksitono emisija stipriosios sąveikos režime.
- O44** **Mantas Drazdys.** Tamm'o plazmon - poliaritonų rezonansinio bangos ilgio derinimas naudojant atominio storio sluoksnio nusodinimą.
- O45** **Andrea Zelioli.** Fabrication of the first GaAsBi based Vertical-External-Cavity Surface-Emitting Laser for NIR.
- O46** **Lamiaa Salah Zaki Abdelrazik.** Evaluation of Limiting Factors that Influence the Quantum Cutting Efficiency of Ytterbium-Doped Halide Perovskite.
- O47** **Ihor Zharchenko.** Evidence of Hot Carrier Effect in a Silicon Solar Cell.
- O48** **Deividas Vainauskas.** SbSel plonų dangų formavimas terminiu užgarinimu.
- O49** **Muhammad Mujahid.** Investigation of Photovoltage Formation in Perovskite Solar Cells.
- O50** **Kazimieras Petrauskas.** Properties of planar and mesoporous perovskite solar cells.

- P1** **Shahid Nawaz.** Innovative Bimetallic 3D Nickel-Iron/Titanium Bifunctional Electrocatalysts for Efficient Hydrogen Evolution Reaction in Acidic Media.
- P2** **Gabrielė Rankelytė.** Electrostatic Interactions in Photosynthetic Complexes.
- P3** **Rodrigas Liudvinavičius.** Hibridinių mikrogumbelių gardelių dydžio įtaka plazmonų rezonanso sužadinimo kokybei.
- P4** **Simonas Driukas.** Polymer-based metalenses for THz beam engineering.
- P5** **Durre Nayab Habib.** Unraveling the impact of biomass burning through isotopic composition.
- P6** **Justina Žemgulytė.** Mašininis mokymasis – potencialus įrankis antenų modeliavime.
- P7** **Simona Raišytė.** Self-Assembled Monolayers for Electrode Surface Coating: Formation and Evaluation.
- P8** **Tayyab Tahir.** Removal of lead (ii) from aqueous solution by buckwheat (*Fagopyrum esculentum*) hull as a low-cost biosorbent: kinetic, equilibrium and thermodynamic studies.
- P9** **Karolis Adomavičius.** Pilno lauko optinė koherentinė tomografija su mažais koherentiniais triukšmais.
- P10** **Justinas Minkevičius.** Femtosekundinio lazerio impulsų sąveikos su anglies pluoštu susprintu plastiku (CFRP) tyrimai.
- P11** **Karina Pokaliuk.** Optical and electrical properties of GaAs/AlGaAs laser diodes with weak and strong optical mode confinement.
- P12** **Aistė Štaupienė.** Internal quantum efficiency of GaAsBi/GaAs MQW structures.
- P13** **Justina Vaičaičytė.** Kvantinių ir klasikinių sistemų analogijos.
- P14** **Aivaras Špokas.** GaAsBi NIR Emitters for Integrated Biosensors in Wearable Technology.
- P15** **Monika Jokubauskaitė.** Relation between photoluminescence intensity of InGaAs quantum wells and design of AlGaAs barriers.
- P16** **Kristina Sobol.** Synthesis and Application of Ti₃C₂T_x MXenes for Determination of Drinking Water Quality and Pollutant Removal.
- P17** **Justas Žuvelis.** Exploring the feasibility of bismuth δ-doping of GaAs/AlAs quantum wells: an optical study.
- P18** **Aistis Melnikas.** Fabrication of a Cu₂O thin film via oxidation for application in SbSe heterojunctions.
- P19** **Austėja Trečiokaitė.** Full-field optical coherence tomography with digital defocus correction in highly scattering samples.
- P20** **Dovilė Vasiliauskaitė.** Study of organic bulk heterojunction solar cells by kinetic photoconductivity method.
- P21** **Erikas Tarvydas.** Biomedical imaging with nano Full-field Optical Coherence Tomography.
- P22** **Aldo Degollado-Vasalauskas.** Palladium-modified cobalt-phosphorus and cobalt-iron-phosphorus coatings for oxygen evolution reaction.
- P23** **Dmytro Shyshkin.** Hydrogen and oxygen evolution on nickel-iron coatings.
- P24** **Jonas Paukštys.** Di-tert-alkyl phosphine synthesis and investigation of chemoenzymatic reactions of their precursors - tertiary acetates.
- P25** **Kasparas Stanaitis.** Structured light beam shaping for terahertz imaging system optimization.
- P26** **Karolis Redeckas.** THz metalens development and application for object imaging.
- P27** **Danielius Ragoža.** Surface Roughness dependence on Specimen Positioning.
- P28** **Germantė Paulikaitė.** Azure A and Methylene Blue dyes removal using adsorption method and MXene nanostructures.



NIKELIO IR JO LYDINIŲ CHEMINIS NUSODINIMAS IR TAIKYMAS

Gitana Valeckytė, Zita Sukackienė, Virginija Kabenienė, Irena Stalnionienė,
Vitalija Jasulaitienė, Jūratė Vaičiūnienė, Loreta Tamašauskaitė-Tamašiūnaitė,
Vidas Pakštas ir Eugenijus Norkus

Fizinių ir technologijos mokslų centras, Katalizés skyrius
Saulėtekio al. 3, LT-10257 Vilnius, el. p.: gitana.valeckyte@ftmc.lt

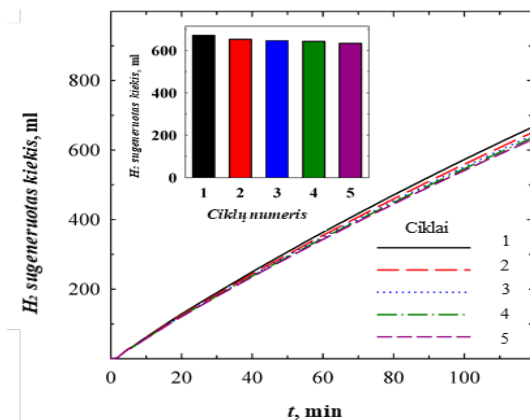
1766 m. anglų mokslininkas Henris Kavendišas pirmasis atrado vandenilį. Vandenilis (H_2) yra paprasčiausias, lengviausias ir gausiausias elementas visatoje. Jis pasižymi dideliu energijos tankiu, todėl yra idealus kuro šaltinis transporto priemonėse. 1888 m. pirmą kartą elektros srovę leidžiant per vandenį buvo pastebėta, kad vandens molekulė skyla į deguonį ir vandenilį. 1960-1970 m. dėl išaugusio elektros poreikio bei atsiradusių pigių gamtinių dujų pradėta gamyba iš iškastinio kuro. Šiuo metu apie 95 proc. pasaulio vandenilio pagaminama iš iškastinio kuro, o tai prisideda prie globalinio atšilimo. Planuojama, kad ateityje vandenilio bus gaminama vis daugiau – ir panaudojimas jo bus platesnis. Dabar didžiausia vandenilio paklausa yra trąšų ir naftos perdirbimo sektoriuose. Vandenilis vis dažniau naudojamas kaupti perteklinei elektros energijai, pagamintai iš atsinaujinančių šaltinių, pvz., vėjo ir saulės energijos. Taip pat vandenilis naudojamas gaminant jvairius cheminius junginius, valant naftos produktus ir apdirbant metalus. Kosminių raketų varikliuose ir jvairiuose eksperimentinėse transporto priemonėse vandenilis kol kas naudojamas ribotai, bet ateityje tai gali pasikeisti [1].

Viena iš svarbiausių vandenilio kaupimo medžiagų savybių yra didelė gravimetrinė vandenilio talpa. Natrio borohidridas laikomas viena tinkamiausių medžiagų vandenilio generavimui, taip pat yra pigus, draugiškas aplinkai, stabilus šarminiuose tirpaluose, nedegus, netoksiškas, nereikia sudėtingų sąlygų proceso vykimui [2, 3]. Pažymėtina, kad borohidrido hidrolizės reakcijos metu gaunamas ypač grynas vandenilis, kuris gali būti tiesiogiai naudojamas vandenilio kuro elementas. Kuro elementai, naudojantys gryną vandenilį, beveik neišskiria kitų teršalų, išskyrus vandenį [4]. Todėl selektyvių šios reakcijos katalizatorių atradimas yra svarbi tyrimo dalis, siekiant išvengti elektrodo paviršiaus užteršimo proceso metu ir vandenilio saugojimo bei transportavimo trūkumų.

Šio darbo tikslas buvo suformuoti NiMo(1)/Cu, NiMo(5)/Cu, NiMo(10)/Cu, NiMo(15)/Cu ir NiMo(20)/Cu katalizatorius, juos charakterizuoti išvertinti jų katalizes savybes natrio borohidrido hidrolizės reakcijai. Visos NiMo dangos buvo nusodintos ant Cu pagrindo paprastu cheminiu nusodinimo metodu, naudojant morfolino boraną kaip reduktorių. Buvo gauti katalizatoriai su skirtingu molibdeno masės procentiniu kiekiu: 1, 5, 10, 15 ir 20. Katalizatorių paviršiaus morfologija, struktūra ir cheminė sudėtis buvo ištirta naudojant

skenuojančią elektronų mikroskopiją (SEM) ir indukuotos plazmos optinės emisijos spektroskopiją (ICP-OES), Rentgeno spindulių fotoelektronų spektroskopiją (XPS), Rentgeno spindulių difrakcijos spektroskopiją (XRD) ir Rentgeno spindulių energijos dispersinę analizę (EDS). Natrio borohidrido hidrolizės reakcijos katalizinis aktyvumas buvo ivertintas išmatuojant vandenilio kiekį, išskiriantį iš katalizuojamos natrio borohidrido hidrolizės reakcijos.

Darbo metu buvo suformuoti visi minėti NiMo/Cu katalizatoriai. Buvo ištirta jų morfologija ir struktūra. Nustatyta, kad paruoštos dangos susideda iš jvairaus dydžio dalelių, kurios susijungia į ovalo formos aglomeratus. Jų vidutinis dydis siekia nuo 0,286 iki 2,143 μm . Taip pat visos tirtos dangos yra kompaktiškos, be jokių ištrūkumų ar defektų ir pasižymėjo kataliziniu aktyvumu natrio borhidrido hidrolizės reakcijai. Nustatyta, kad dviejų komponentų NiMo(20) danga pasižymėjo didžiausiu kataliziniu aktyvumu. Nustatyta, kad vandenilio susidarymo greitis priklauso nuo molibdeno kieko katalizatoriuse ir darbinio tirpalio temperatūros. Vandenilio susidarymo greitis nuo 3,55 iki 6,32 ml/min buvo pasiektas esant 343 K temperatūrai, naudojant NiMo/Cu katalizatorius su jvairaus molibdeno kiekiu, atitinkamai nuo 1 iki 20 masės %.



1 pav. NiMo(20)/Cu katalizatoriaus pakartotinis panaudojimas po penkių ciklų 5 masės % NaBH4 + 0,4 masės % NaOH tirpale.

Literatūra:

1. <https://ambergrid.lt/zaliosios-dujos/vandenilis/trumpai-apie-vandeniliu/957>
2. G. Bozkurt, A. Ozer, A. B. Yurtcan, Energy, 180, 702-713 (2019).
3. Z. Chen, K. O. Kirlikovali, K. B. Idrees, M. C. Wasson, O. K. Farha, Chemistry, 8, 693-716 (2022).
4. L. Van Hoecke, L. Laffineur, R. Campe, P. Perreault, S. W. Verbruggen, S. Lenaerts, Energy and Environ. Science, 14, 815-843 (2021).

MACHINE LEARNING ALGORITHMS FOR THYROID CANCER DIAGNOSIS BASED ON SECOND HARMONIC GENERATION MICROSCOPY

Yaraslau Padrez¹, Lena Golubewa¹, Igor Timoshchenko¹, Lucian G. Eftimie^{2,3}, Radu Hristu⁴ Danielis Rutkauskas¹

¹Center for Physical Sciences and Technology, Department of Molecular Compound Physics,
LT-10257 Vilnius, Lithuania,

²Central University Emergency Military Hospital, Pathology Department, 134 Calea Plevnei,
RO-010825 Bucharest, Romania,

³Department of Special Motricity and Medical Recovery, The National University of Physical Education and Sports,
Strada Constantin Noica 140, RO-060057 Bucharest, Romania,

⁴Center for Microscopy-Microanalysis and Information Processing, National University of Science and Technology
Politehnica Bucharest, 313 Splaiul Independentei, RO-060042 Bucharest, Romania,
email: yaraslau.padrez@ftmc.lt

Papillary thyroid carcinoma (PTC) and follicular thyroid carcinoma (FTC) account for up to 88% of all cases of thyroid cancer [1]. Both types of thyroid cancer are well differentiated, meaning that the cancer cells retain essential characteristics of normal cells. However, it is very important to correctly classify the type of cancer, as the effectiveness of treatment, patient survival and overall patient condition are highly dependent on the accuracy and timeliness of diagnosis. Cancer progression is associated with a change in the extracellular matrix, an altered balance between collagen synthesis and degradation, and the possible formation of a collagen barrier between PTC or FTC cells and normal tissue. Therefore, the specificity of the cancer-related collagen network can serve as a diagnostic biomarker for a specific type of thyroid cancer. Second harmonic generation (SHG) microscopy enables non-destructive, label-free characterization of the collagen fibers that form the extracellular matrix of tissue [2]. Supported by machine learning (ML) algorithms, it can contribute, for example, to the identification of capsular invasions in PTC [3]. The application of supervised ML models in conjunction with SHG imaging of cancer tissue can provide additional automated diagnosis, reveal biomarkers of early cancer progression and avoid human error. In the present study, we aimed to develop supervised ML models to discriminate between SHG microscopy images of PTC and FTC based on the intensity and texture parameters of SHG images of both cancers. The texture parameters were calculated on the basis of the gray-level co-occurrence matrix and the gray level run-length matrix. From a wide range of ML classification algorithms, we selected two monolithic (Multi-layer Perceptron (MLP), Support Vector Classifier (SVC)) and two ensemble models (Random Forest (RF), Extreme Gradient Boosting (XGBoost)). The latter models are considered advantageous compared to monolithic models, as they represent a combination of individual classifiers and have proven to be more stable against data changes. Stratified K-fold cross-validation [4] was performed to estimate the best sets of key hyperparameters that provide the best

predictive performance of each model. The diagnostic potential of the developed models was then estimated using the test dataset. The test dataset was scaled using the scaling parameters estimated with the training dataset. All calculations were performed in Python using open source libraries.

The estimated values of diagnostic accuracy and specificity of all models obtained with the training and test datasets are shown in Table 1. For the training dataset, the classification accuracy varies between 79.4% for MLP and 100% for RF. However, the significant drop in the accuracy of RF for the unknown test data indicates a possible overtraining. Thus, RF cannot be considered as an optimal model for PTC/FTC classification. The diagnostic accuracy of the remaining ML models ranges from 72.17% for XGBoost to 76.95% for SVC, suggesting that SVC is the optimal ML model for PTC/FTC classification. Moreover, SVC outperforms the other models in both sensitivity and accuracy (Table 1).

Table 1. Results of classification

| ML model type | ML model | Testing accuracy, % | Training accuracy, % | Sensitivity, % | Specificity, % |
|---------------|----------|---------------------|----------------------|----------------|----------------|
| Monolithic | SVC | 76.95 | 84.62 | 82.27 | 69.65 |
| | MLP | 74.34 | 79.40 | 83.07 | 62.38 |
| Ensemble | XGBoost | 72.17 | 82.60 | 79.65 | 60.45 |
| | RF | 71.55 | 100 | 78.15 | 63.96 |

The results indicate that SHG microscopy of thin thyroid tissue sections, combined with machine learning algorithms, allows for automatic classification of samples as either PTC or FTC, achieving an accuracy of over 76% and a sensitivity of over 82%. This approach could therefore provide significant clinical benefits for the diagnosis and appropriate treatment of thyroid cancer patients.

References:

- [1] L. Boucai, M. Zafereo, and M. E. Cabanillas, *JAMA* **331**, 425 (2024).
- [2] Y. Padrez, L. Golubewa, T. Kulahava, T. Vladimirskaia, G. Semen-kova, I. Adzerikho, O. Yatsevich, N. Amaegberi, R. Karpicz, Y. Svirko, P. Kuzhir, and D. Rutkauskas, *Sci Rep* **12**, 7330 (2022).
- [3] L. G. Eftimie, Y. Padrez, L. Golubewa, D. Rutkauskas, and R. Hristu, *Biomed. Opt. Express* **15**, 4705 (2024).
- [4] A. Seraj, M. Mohammadi-Khanaposhtani, R. Daneshfar, M. Naseri, M. Esmaeili, A. Baghban, S. Habibzadeh, and S. Eslamian, in *Handbook of Hydroinformatics* (Elsevier, 2023), pp. 89–105.

Bimetallic 3D Nickel-Manganese Coatings: High-performance HER and Stable OER Electrocatalysts for Alkaline Water Splitting and Overall Seawater Splitting

Sukomol Barua, Aldona Balčiūnaitė, Daina Upskuvienė, Jūratė Vaičiūnienė,

Loreta Tamašauskaitė-Tamašiūnaitė and Eugenijus Norkus

Center for Physical Sciences and Technology (FTMC), Department of Catalysis

Saulėtekio av. 3, LT-10257 Vilnius, email: sukomol.barua@ftmc.lt

The perfect strategy for producing green and renewable hydrogen (H_2) fuel is the direct electrocatalytic splitting of abundant seawater rather than scarce freshwater. The half-reactions that take place during the electrocatalytic splitting of freshwater/seawater are the hydrogen evolution reaction (HER) and the oxygen evolution reaction (OER). However, the OER is affected by the slow four-electron transfer kinetics and the competitive chlorine evolution reaction (CER) in seawater. To overcome the kinematic and competitive barriers of seawater splitting and to achieve an excellent and stable overall performance of seawater splitting, we herein report a facile, low-cost, one-step fabrication of 3D structured nickel-manganese (NiMn) bimetallic coatings using a dynamic hydrogen bubble template technique. The electrocatalytic activities of these synthesized catalytic materials were investigated in alkaline media (1 M KOH), simulated seawater (0.5 M NaCl + 1 M KOH, denoted as SSW) and alkaline natural seawater (natural seawater + 1 M KOH, denoted as ASW) for HER and OER using linear sweep voltammetry (LSV) at temperatures ranging from 25 °C to 75 °C. Scanning electron microscopy (SEM) and inductively coupled plasma optical emission spectroscopy (ICP-OES) were used to examine the surface morphology and composition of the prepared catalysts.

The as-prepared NiMn/Ti-5 electrocatalyst, electro-deposited using a chemical bath with a $\text{Ni}^{2+}:\text{Mn}^{2+}$ molar ratio of 1:5, exhibits excellent HER activity with ultra-low overpotentials of **64.2** mV and **79.3** mV to reach the benchmark current density of 10 mA cm $^{-2}$ in SSW and ASW, respectively. In contrast, the NiMn/Ti-1 catalyst, prepared from a plating bath containing $\text{Ni}^{2+}:\text{Mn}^{2+}$ molar ratio of 1:1 with the lowest Mn loading of 13.43 $\mu\text{g cm}^{-2}$, exhibits reasonable OER activity, requiring overpotentials of 386 and 388 mV, to achieve the benchmark current density of 10 mA cm $^{-2}$ in Cl $^-$ ions rich SSW and ASW, respectively. This optimal bimetallic electrocatalyst also demonstrated superior long-term stability, maintaining a constant potential of 1.81 V (vs. RHE) and a constant current density of 10 mA cm $^{-2}$ for

24 hours in both working electrolytes. It is worth-mentioning that the both optimal electrocatalysts assembled in a two-electrode electrolyzer namely, $[\text{NiMn/Ti-5}_{(-)}||\text{NiMn/Ti-1}_{(+)}]$ required only **1.619 V** to deliver current density of 10 mA cm^{-2} for overall alkaline seawater splitting at room temperature, which is even 75 mV lower than the noble metal-based electrolyzer assembly $\text{Pt}_{(-)}||\text{NiMn/Ti-1}_{(+)}$.

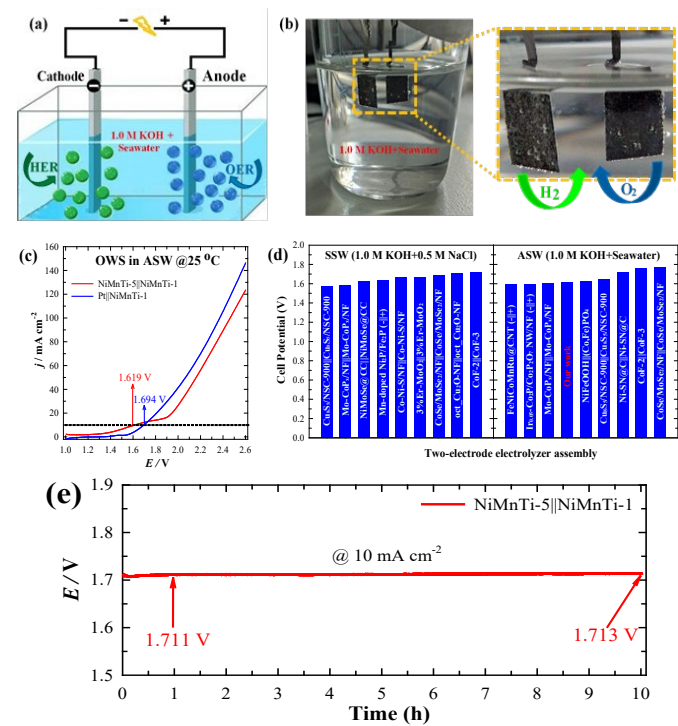


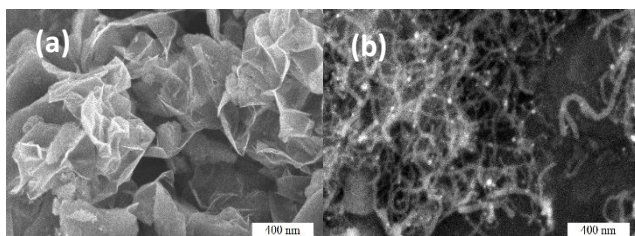
Fig. 1. Schematic representation of overall alkaline seawater splitting (a), the digital photograph of the assembled two-electrode cell (left) and the bubbles on the electrodes (right) (b), LSVs for the overall alkaline seawater splitting at 25 °C (c), a comparison of activity of the assembled electrolyzer with recently reported catalysts (d) and long-term durability test of the assembled two-electrode NiMn/Ti-5(-)||NiMn/Ti-1(+) electrolyzer for overall alkaline natural seawater splitting (e).

HIDRAZINO OKSIDACIJOS ANT NIKELIU IR AZOTU LEGIRUOTŲ ANGLIES KATALIZATORIŲ TYRIMAS

Virginija Ulevičienė, Loreta Tamašauskaitė Tamašiūnaitė

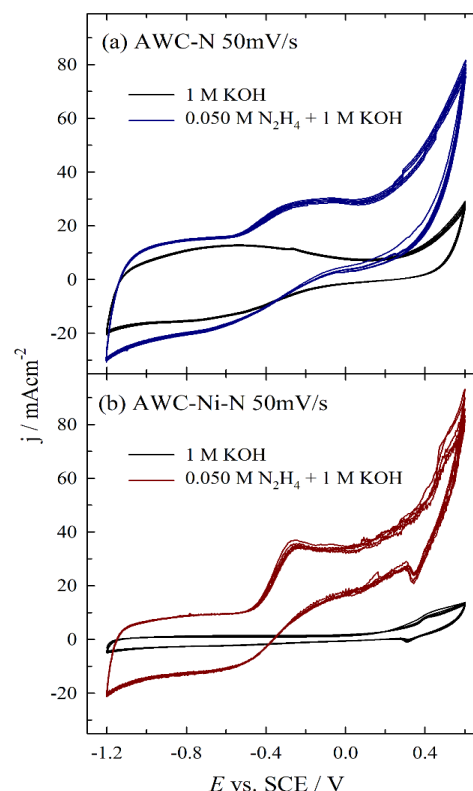
Fizinių ir technologijos mokslų centras, Katalizés skyrius
Saulėtekio al. 3, LT-10257 Vilnius, el. p.: virginija.uleviciene@ftmc.lt

Iš biomasės gauta anglis yra perspektyvi alternatyva tradiciškai gaminamiems anglies pagrindo katalizatoriams. Ši medžiaga turi didelį potencialą kaip tvarus anglies šaltinis, skirtas atsinaujinantiems energijos šaltiniams naujos kartos energijos kaupimo ir konversijos sistemose. Biomasė yra svarbus anglies pirmtakas dėl savo atsinaujinamumo, gausumo Žemėje, ekologiškumo, mažų sąnaudų, netoksiškumo, tvarumo, paprastos gamybos bei heteroatomų (N, P, S ir kt.) jvairovės savo vidinėje sudėtyje. Šiame darbe pristatoma paprasta ir nebrangi katalizatorių sintezės strategija, pagrindu naudojant susintetintus anglies katalizatorius iš medienos atliekų bei juos legiruojant nikeliu ir azotu. Iš beržo skiedrų susintetinti anglies milteliai buvo chemiškai aktyvuojami NaOH 800°C temperatūroje ir po to legiruojami azotu ir nikelio (Ni) dalelėmis, naudojant dicianodiamidą (DCDA) kaip azoto prekursorių ir nikelio acetatą kaip Ni²⁺ jonų prekursorių, naudojant rotacinio garinimo metodą. Susintetintų AWC-N ir AWC-Ni-N katalizatorių paviršiaus morfologija, struktūra bei sudėtis buvo detaliai ištirta, naudojant peršviečiamos elektroninės mikroskopijos (TEM), Rentgeno spinduliuų fotoelektronų spektroskopijos (XPS), skenuojančiosios elektronų mikroskopijos (SEM), Indukuotos plazmos optinės emisijos spektroskopijos (ICP-OES) ir Raman sprekstroskopijos metodus, o elektrokatalizinis aktyvumas hidrazino (N₂H₄) elektrooksidacijai buvo įvertintas, naudojant ciklinę voltamperometriją. Nustatyta, kad susintetintas AWC-Ni-N katalizatorius susideda iš 95,73 at.% C, 0,77 at.% N, 1,56 at.% O ir 1,94 at.% Ni. Be to, šis katalizatorius turi labai didelį specifinių paviršiaus plotą – 2050 m² g⁻¹.



1 pav. SEM vaizdai AWC-N (a) ir AWC-Ni-N (b) katalizatorių.

2 paveiksle pavaizduotos ciklinės voltamperogramos ant AWC-N (a) ir AWC-Ni-N (b) katalizatorių 1 M NaOH ir 0,05 M N₂H₄ + 1 M KOH tirpaluose, skleidžiant elektrodo potencialą 50 mV s⁻¹ greičiu. AWC-Ni-N katalizatorius pasižymi didesniu elektrokataliziniu aktyvumu N₂H₄ oksidacijos reakcijai nei AWC-N katalizatorius: išmatuotos N₂H₄ oksidacijos srovės tankio vertės yra didesnės ant AWC-Ni-N katalizatoriaus lyginant su AWC-N katalizatoriumi. N₂H₄ oksidacija ant AWC-Ni-N katalizoriaus vyksta, esant neigiamesnėms elektrodo potencijalo vertėms nei ant AWC-N katalizoriaus.



2 pav. CVs užrašyti ant AWC-N (a) ir AWC-Ni-N (b) katalizatorių 1 M NaOH ir 0,05 M N₂H₄ + 1 M KOH tirpaluose, skleidžiant elektrodo potencialą 50 mV s⁻¹ greičiu, T = 25°C.

Nepertraukiamo ciklinimo eksperimentai parodė, kad AWC-Ni-N pasižymi aktyvumu ir stabilumu N₂H₄ elektrooksidacijos reakcijai ir gali būti naudojamas kaip anodo katalizatorius tiesioginiuose hidrazino kuro elementuose (DHFC).

ELECTROCATALYTIC PERFORMANCE OF COBALT-PHOSPHORUS CATALYST FOR OVERALL WATER SPLITTING IN ALKALINE MEDIA

Huma Amber, Loreta Tamasauskaite-Tamasiunaite

Center for Physical Sciences and Technology, Department of Catalysis
Saulėtekio av. 3, LT-10257 Vilnius, email: huma.amber@ftmc.lt

The process of electrochemical water splitting has the potential to offer a sustainable energy conversion method that does not result in environmental contamination. The development of active, stable, and low-cost electrocatalysts is a crucial objective for practical applications that must meet scalability and durability requirements. This work summarizes the research on the electrocatalytic performance of cobalt phosphorus (Co-P) in two important water splitting reactions: the hydrogen evolution reaction (HER) and the oxygen evolution reaction (OER).

Herein, Co-P catalysts with different compositions were synthesized by the electroless metal deposition method on a copper sheet substrate. Sodium hypophosphite (NaH_2PO_2) was used as the reducing agent. Scanning electron microscopy (SEM) and energy-dispersive X-ray spectroscopy (EDX) were used to characterize the surface morphology, structure, and composition of the prepared catalysts.

The Co-P catalysts were obtained with different P contents of 5, 8, and 11 wt%. The performance of the Co-P coatings for the HER and OER was evaluated by linear sweep voltammetry (LSV) in 1 M KOH solution.

It was found that the Co-P coating with the 11 wt% of P exhibited the lowest overpotential value of -115.4 mV for the HER to obtain a current density of 10 mA cm⁻² compared to the Co-P coatings with 8 wt% (-121.5 mV) and 5 wt% (-182.9 mV) of P. On the other hand, the lowest OER overpotential (419.46 mV) was observed for the Co-P coating with the 8 wt% of P to obtain a current density of 10 mA cm⁻² as compared with the Co-P coatings with 5 wt% (430.51 mV) and 11 wt% (466.86 mV) of P. The obtained catalysts seem to be suitable candidates for HER and OER in alkaline media.

BISMUTH PLATED LASER-INDUCED (Bi-LIG) GRAPHENE ELECTROCHEMICAL SENSOR FOR ZINC DETECTION IN PLANT TISSUES

^{1*} Pamela Rivera, ² Šarūnas Mickus, ² Aivaras Sartanavičius,
² Romualdas Trusovas, ¹Rasa Pauliukaite

¹Department of Nanoengineering, ²Department of Laser Technology,
Center for Physical Sciences and Technology (FTMC), Savanoriu ave. 231, LT-02300 Vilnius
e-mail: pamela.rivera@ftmc.lt

Zinc is a vital micronutrient for plants as it plays a role in metabolic and physiological processes, enzyme activation, and maintaining ion balance [1]. A lack of zinc can interfere with basic metabolic functions, resulting in stunted growth and reduced nutrient absorption. Conversely, excessive zinc can hinder germination, reduce biomass, and negatively impact yield and quality [2]. To optimize zinc fertilization, accurate measurements of zinc levels in both plant tissues and growing substrates are crucial to ensure fertilization efficiency and avoid overapplication.

Currently, zinc content in plant tissues is typically measured using atomic absorption spectrophotometry following acid digestion, a method that is both costly and time-consuming [3]. Electrochemical sensors offer a faster, more accurate, and on-site alternative for measuring zinc levels, which would provide more timely data for decision-makers involved in fertilization management.

Previous studies have demonstrated the sensitivity of bismuth films for detecting Zn(II) [4], while laser-induced graphene (LIG) has shown promise as a flexible sensor material [5]. In this study, we explore the use of bismuth-plated laser-induced graphene (Bi-LIG) as a potential electrode material for detecting zinc in plant tissues via square wave anodic stripping voltammetry (SWASV). The LIG is produced from polyimide film, onto which a bismuth film is electroplated.

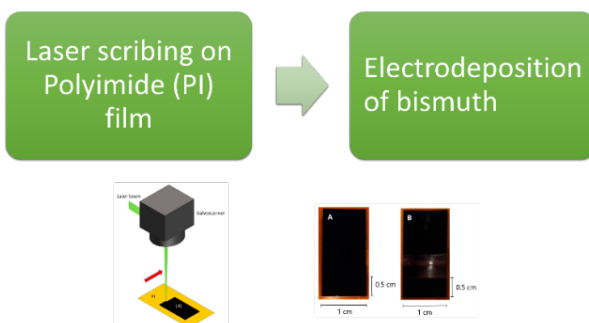


Fig. 1. Scheme of the fabrication process of the Bi/LIG electrodes. The LIG was produced from polyimide (PI) film under the following laser parameters: CO₂, 0.5 W laser power, 20 mm/s speed and 100 KHz frequency. Bismuth was electrodeposited onto the LIG from a 20 mM Bi solution.

The obtained LIG is studied using Raman spectroscopy to determine the quality of the graphene. Additionally, the electrochemical properties of synthesized sensing material will be investigated utilizing cyclic voltammetry (CV) and electrochemical impedance spectroscopy (EIS). Finally, the sensing material will be applied for the detection of Zn content in plant tissues.

References

1. M. Yang et al., *The Plant Journal* 2020, 103, 1695-1709.
2. H. Kaur and N. Garg, *Planta* 2021, 253, no. 6, 129.
3. C. Wei et al., *Science of The Total Environment* 2022, 807, 150992.
4. G. Grincienė, A. Selskiénė, R. Verbickas, E. Norkus and R. Pauliukaite, *Electroanalysis* 2009, 21, 1743-1749.
5. V. Žutautas, R. Trusovas, A. Sartanavičius, K. Ratautas, A. Selskis and R. Pauliukaite, *Chemosensors* 2023, 11, 329.

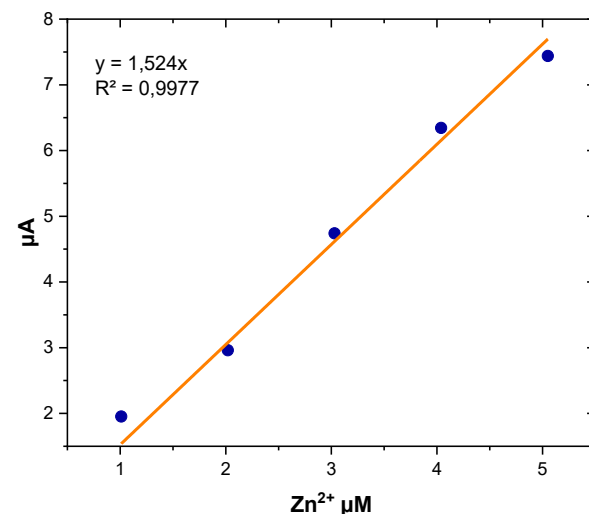


Fig. 2. Calibration curve obtained with the Bi-LIG for Zn²⁺

Acknowledgements:

This research is supported by RTO Lithuania, project No. RTO_AgroNanoSens_JVS_2 023.

FROM EQUATIONS TO NEURAL NETWORKS: THE APPLICATION OF PHYSICS-INFORMED NEURAL NETWORKS (PINNs) TO ELECTROCHEMICAL SENSOR MICROARRAY MODELLING

Mohamed Abdelkader¹, Haotian Chen², Richard G. Compton², Rasa Pauliukaitė¹,

1-Center for Physical Sciences and Technology, Department of Nanoengineering,
Savanořių pr. 231, LT-02300 Vilnius, email: mohamed.fawzy@ftmc.lt

2-Department of Chemistry, Physical and Theoretical Chemistry Laboratory,
University of Oxford, South Parks Road, Oxford OX1 3QZ, UK

Electrochemical detection of Zn(II) is crucial because it is an essential microelement in plants and animals as well as humans [1]. This study focuses on understanding of Zn metabolism in plants using beetroot leaves as model systems. ZnO nanoparticles (ZnONPs) are used as fertilisers sprayed on leaves and the task is to detect if leaves digest ZnO to Zn²⁺. The task of this work is modeling and simulating of microarray electrodes for electrochemical detection of Zn(II) ions in beetroot leaves. A combination of classical diffusion models and Physics-Informed Neural Networks (PINNs) [2] is employed to simulate electrode array geometry related ionic transport processes to enhance detection sensitivity. Fick's second law serves as the foundational model for diffusion, while PINNs integrate physical laws directly into deep learning models for higher predictive accuracy in complex electrochemical systems [3].

The finite-difference method [4] was applied to simulate the chronoamperometric response of microarray electrodes starting with a single microdisk electrode. MATLAB and COMSOL software were used for validation against theoretical and experimental data, as shown in Figure 1 the electrolyte species concentration across the microdisk electrode geometry. This simulation investigated both thin-layer and microdisk electrode configurations, optimizing parameters such as diffusion coefficients, electrode spacing, and concentration gradients. PINNs, which combine data-driven approaches with physical principles, are particularly beneficial for modelling when experimental data are sparse or noisy.

The diffusion of Zn(II) ions was modelled in beetroot leaves, where nanoparticles tend to accumulate along the leaf edges due to physical and chemical factors. The study also compares uniform grid and hexagonal microarray electrode designs, optimizing electrode placement for uniform electric field distribution and improved detection sensitivity. Combining PINNs with classical models provides a robust framework for advancing the electrochemical detection of Zn(II) and other ions in biological systems.

Figure 1 shows the COMSOL finite element simulation for the microdisk electrode.

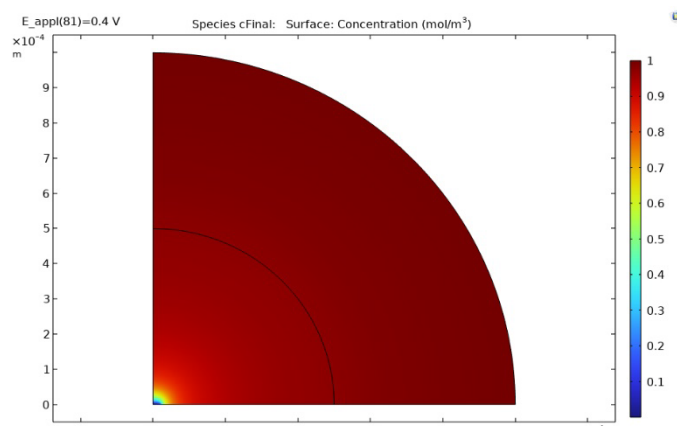
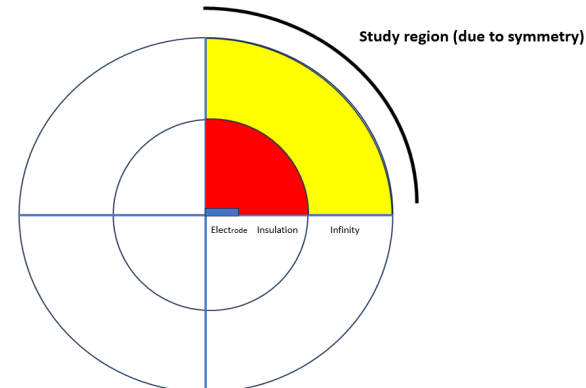


Fig. 1 Simulation of the microdisk electrode using COMSOL

References

1. G. Ringgit, S. Siddiquee, S. Saallah et al. Sci Rep. **12**, 18582 (2022).
2. S. Rezaei, K.P. Birke, Batteries, **9**, 301 (2023).
3. Raissi et al., J. of Comp. Phy., 2019.
4. P. Molina, F. Gonzalez, Pulse Voltammetry in Physical Electrochemistry and Electroanalysis (Springer, 2011).

MICROBIAL AND ELECTROCHEMICAL CHARACTERIZATION OF INDIVIDUAL GRANULES FOR FIXED BED ELECTRODES IN MICROBIAL ELECTROCHEMICAL TECHNOLOGIES

Viktorija Reinikovaite¹, Benjamin Korth², Arūnas Stirkė¹, Falk Harnisch²

¹Center for Physical Sciences and Technology, Department of Functional Materials and Electronics
Saulėtekio av. 3, LT-10257 Vilnius, email: viktorija.reinikovaite@ftmc.lt

²Helmholtz Centre for Environmental Research GmbH – UFZ, Department of Microbial Biotechnology
Permoser Str. 15, 04318 Leipzig, Germany

Electroactive microorganisms possess the remarkable ability to exchange electrons with electrodes, thereby integrating their metabolism with electrochemical systems¹. This fundamental mechanism, known as extracellular electron transfer (EET), underpins the exciting potential of microbial electrochemical technologies (MET)². These technologies have garnered significant attention over the past two decades due to their diverse applications and potential for sustainable energy and environmental solutions.

Among the various applications of MET, microbial fuel cells (MFCs) represent their archetype converting organic matter in wastewater into electrical energy³. In this process, electroactive microorganisms oxidize organic materials, transferring the released electrons to anodes. This not only results in wastewater treatment but also generates electrical energy, highlighting the dual benefits of MFCs. Beyond wastewater treatment, MFCs have potential applications in remote power generation, biosensing, and environmental monitoring. However, optimizing the performance of MET systems requires advances in reactor design and electrode materials, necessitating a multidisciplinary approach that encompasses engineering, microbiology, electrochemistry, and biochemistry.

Fixed bed electrode reactors are a promising configuration within the MET field⁴, known for their dense packing of graphite granules which are cheap, biocompatible, and offer high electrode surface-to-reactor volume ratio⁵. These reactors have demonstrated significant potential in various applications such as the removal of nitrate, sulfate, and other contaminants from groundwater and wastewater⁶. Despite offering a low-cost, robust, and sustainable solution, such reactors face challenges like activity stratification, which causes dead volumes and electrochemically inactive zones, limiting their efficiency⁷. To address these challenges, this study aimed to explore the bioelectrochemical interactions between individual graphite granule (GG) electrodes and the electroactive model organism *Geobacter sulfurreducens*, forming biofilms of up to 100 µm thickness at electrodes.

The main method used in this study was cyclic voltammetry (CV), as this is a well-established method for analyzing the electron transfer and mass transfer at electrodes. For electroactive

biofilms, three mass transfer processes are relevant and can potentially limit its activity: transport of the substrate, transport of the counter ion out of the biofilm and the electron transport within the biofilm. Therefore, biofilms of four different thicknesses were cultivated at GG, which were categorized by the produced charge.

To examine in detail the mass transfer of the substrate (acetate) and the counterions (Na⁺, K⁺, H⁺), two experimental media conditions were used i) 10 % substrate concentration and ii) 10 % buffer strength. In addition to turnover CV (i.e., in the presence of substrate) and non-turnover CV (i.e., in the absence of substrate) were performed, allowing the application of the Randles-Ševčík equation to obtain diffusion coefficient. For verifying the obtained results, similar experiments were performed with ideal electrodes: i) graphite plates and ii) metal spheres.

Understanding the mass transfer at GG and its limitations will support measures to improve the design and performance of fixed bed electrode reactors.

References

- (1) Koch, C.; Harnisch, F. Is There a Specific Ecological Niche for Electroactive Microorganisms? *ChemElectroChem* **2016**, 3 (9), 1282-1295. <https://doi.org/10.1002/celc.201600079>.
- (2) Logan, B. E.; Rossi, R.; Ragab, A.; Saikaly, P. E. Electroactive Microorganisms in Bioelectro-chemical Systems. *Nat Rev Microbiol* **2019**, 17 (5), 307-319. <https://doi.org/10.1038/s41579-019-0173-x>.
- (3) Kumar, S. S.; Kumar, V.; Malyan, S. K.; Sharma, J.; Mathimani, T.; Maskarenj, M. S.; Ghosh, P. C.; Pugazhendhi, A. Microbial Fuel Cells (MFCs) for Bioelectrochemical Treatment of Different Wastewater Streams. *Fuel* **2019**, 254, 115526. <https://doi.org/10.1016/j.fuel.2019.05.109>.
- (4) Rodrigo Quejigo, J.; Tejedor-Sanz, S.; Esteve-Núñez, A.; Harnisch, F. Bed Electrodes in Microbial Electrochemistry: Setup, Operation and Characterization. *ChemTexts* **2019**, 5 (1), 4. <https://doi.org/10.1007/s40828-019-0078-3>.
- (5) Caizán-Juanarena, L.; Sleutels, T.; Borsje, C.; Ter Heijne, A. Considerations for Application of Granular Activated Carbon as Capacitive Bioanode in Bioelectrochemical Systems. *Renewable Energy* **2020**, 157, 782-792. <https://doi.org/10.1016/j.renene.2020.05.049>.
- (6) Ceballos-Escalera, A.; Pous, N.; Chiluiza-Ramos, P.; Korth, B.; Harnisch, F.; Bañeras, L.; Balaguer, M. D.; Puig, S. Electro-Bioremediation of Nitrate and Arsenite Polluted Groundwater. *Water Research* **2021**, 190, 116748. <https://doi.org/10.1016/j.watres.2020.116748>.
- (7) Quejigo, J. R.; Korth, B.; Kuchenbuch, A.; Harnisch, F. Redox Potential Heterogeneity in Fixed-Bed Electrodes Leads to Microbial Stratification and Inhomogeneous Performance. *ChemSusChem* **2021**, 14 (4), 1155-1165. <https://doi.org/10.1002/cssc.202002611>.

ESSENTIAL OILS AS COMPONENTS OF DRUG DELIVERY SYSTEMS: ELECTROCHEMICAL STUDIES

Greta Kasputė^{1,2}, Deivis Plaušinaitis³, Urtė Prentice^{1,2,3}

¹ Center for Physical Sciences and Technology, Department of Nanotechnology
Saulėtekio Av. 3, LT-10257 Vilnius, el. p.: greta.kaspute@ftmc.lt and urte.prentice@ftmc.lt

² Innovative Medicine Center, Department of Personalised Medicine
Santariskiu St., 5, LT-08406 Vilnius

³ Department of Physical Chemistry, Institute of Chemistry, Faculty of Chemistry and Geosciences,
Vilnius University, Naugarduko St. 24, LT-03225 Vilnius, Lithuania, el.p.: urte.prentice@chgf.vu.lt;
deivis.plausinaitis@chf.vu.lt

Personalized medicine holds promise not only for treating rare diseases but also for improving outcomes in broader patient populations. Achieving its full potential requires the development of new drug delivery systems and advanced analytical methods.

Researchers are exploring natural-origin compounds, such as essential oils, which possess diverse biological properties, including antimicrobial, anti-inflammatory, and antioxidant effects. Essential oils, which are hydrophobic and fat-soluble, can cross the blood-brain barrier and penetrate the skin, making them valuable in drug delivery systems either as carriers or therapeutic agents. Studies have demonstrated that incorporating essential oils into drug delivery systems can enhance the efficiency of drug transport or amplify therapeutic effects. Thus, this research focuses on designing a polymer-based drug delivery system, evaluated using electrochemical techniques. The research material is geraniol – an acyclic monoterpene with antioxidant, antibacterial, and anti-inflammatory properties. Geraniol, present in essential oils like ginger, thyme, and geranium, has shown promise in various drug delivery applications, such as improving drug efficacy against *Candida Albicans* [1], enhancing neuroprotection in ischemia/reperfusion injury [2], treating osteoarthritis [3], and combating liver cancer [4].

Electrochemical studies play an important role in evaluating and optimizing drug delivery systems, providing insight into how essential oils, like geraniol, can enhance the efficiency and effectiveness of drug delivery using electrochemistry. This research focuses on exploring the potential of essential oils in innovative drug delivery technologies for improved therapeutic outcomes. Methods such as cyclic voltammetry, electrochemical impedance spectroscopy, and quartz-crystal microbalance are used to deliver valuable results.

The findings from this research pave the way for the development of advanced drug delivery systems with enhanced efficiency. These systems can be tailored for the delivery of a variety of drugs, depending on specific therapeutic needs. Geraniol, in particular, shows promise as both a carrier matrix for controlled drug release and as an active compound with significant biological effects. Additionally, an electrochemical sensor could be designed to detect specific essential oil molecules, addressing the critical issue of falsified oils. Such a sensor would be highly valuable for consumers and laboratories, providing a reliable tool for routine analysis of essential oil purity, including the detection of geraniol in mixtures.

References

1. Silva Pontes, C., Garcia de Carvalho, G., Rosa Perin Leite, A., Chorilli, M., Palomari Spolidorio, D. M. Improving Drug Delivery on *Candida Albicans* Using Geraniol Nanoemulsion. *Pharmaceutics* **2023**, 15 (10), 2475. <https://doi.org/10.3390/pharmaceutics15102475>.
2. M. Soliman, S., M. Sheta, N., M. M. Ibrahim, B., M. El-Shawwa, M., M. Abd El-Halim, S. Novel Intranasal Drug Delivery: Geraniol Charged Polymeric Mixed Micelles for Targeting Cerebral Insult as a Result of Ischaemia/Reperfusion. *Pharmaceutics* **2020**, 12 (1), 76. <https://doi.org/10.3390/pharmaceutics12010076>.
3. Pan, J., Cai, Y., Zhang, C., Xu, S. Intra-Articular Delivery of Geraniol Encapsulated by PH/Redox-Responsive Nanogel Ameliorates Osteoarthritis by Regulating Oxidative Stress and Inflammation. *J Mol Histol* **2023**, 54 (6), 579–591. <https://doi.org/10.1007/s10735-023-10163-4>.
4. Duan, S., Xia, Y., Tian, X., Cui, J., Zhang, X., Yang, Q., Zhao, T., Lin, Y.; Zhang, F.; Zhang, X., Cen, J. A Multi-Bioresponsive Self-Assembled Nano Drug Delivery System Based on Hyaluronic Acid and Geraniol against Liver Cancer. *Carbohydr Polym* **2023**, 310, 120695. <https://doi.org/10.1016/j.carbpol.2023.120695>.

OPTIMISED MOLECULARLY IMPRINTED POLYMER FOR DETECTION OF SALICYLIC ACID BY DFT AND MOLECULAR MECHANICS CALCULATIONS

Enayat Mohsenzadeh, Vilma Ratautaite, Arunas Ramanavicius

Centre for Physical Sciences and Technology, Department of Nanotechnology
Saulėtekio av. 3, LT-10257 Vilnius, email: enayat.mohsenzadeh@ftmc.lt

Molecularly imprinted polymers (MIP) are synthetic receptors with tailor-made binding sites for a specific target. The stepwise MIP fabrication process includes (1) the selection of optimal pre-polymerisation reagents, (2) polymerisation, (3) extraction of template (target) molecules from the polymer film, and (4) target molecules rebinding on the MIP. As a result, a functional polymer film comprising complementary binding sites is created enabling MIPs to detect the target selectively [1].

However, the choice of reagents and methods dramatically impacts the MIP performance. Therefore, the MIP preparation process requires exhaustive trial-error experiments, which are time-consuming, expensive and might be environmentally harmful. Computational methods pave the way for minimising the need for experiments. They provide smarter design of MIPs, which leads to better experiment results [2]. The atomistic level of simulations along with quantum mechanical calculations are widely used for the MIP design.

Molecular mechanics and density functional theory (DFT) calculations were applied to design the MIP for salicylic acid detection in this study. The selection of the best functional monomer was done. Then, the optimal molar ratio of monomer to template was calculated. The candidate solvents were assessed and the study of MIP interactions with the target was evaluated. This modelling provided an optimised pre-polymerisation mixture. Hence, this information is used to design a more advanced MIP with lower expenses and better performance.

References:

1. Pilvenyte, G. et al. Molecularly Imprinted Polymer-Based Electrochemical Sensors for the Diagnosis of Infectious Diseases. *Biosensors* 13, 620 (2023).
2. Mohsenzadeh, E. et al. Design of molecularly imprinted polymers (MIP) using computational methods: A review of strategies and approaches. *WIREs Computational Molecular Science* 14, e1713 (2024).

MIP FORMAVIMAS POLIPIROLO PAGRINDU

Greta Pilvenytė¹, Raimonda Bogužaitė¹, Vilma Ratautaitė¹, Arūnas Ramanavičius^{1,2}

Fizinių ir technologijos mokslų centras, Nanotechnologijų skyrius
Saulėtekio al. 3, LT-10257 Vilnius, el. p.: greta.pilvenyte@ftmc.lt

¹Vilniaus universitetas, Chemijos ir geomokslų fakultetas, Chemijos institutas
Naugarduko g. 24, LT 03225 Vilnius

Molekulių įspaudais modifikuoti polimerai (MIP) yra inovatyvi medžiagų klasė, gebanti atpažinti tikslines molekules pagal "rakto ir spynos" principą, kai atpažinimo vietas yra suformuojamos naudojant įspaudžiamas šablonines molekules [1]. Šiame pranešime dėmesys skiriamas į MIP formavimą elektrai laidaus polimero pagrindu. Elektrocheminio jutiklio formavimui naudojami keli elektrai laidūs polimerai tarp kurių yra ir polipirolas, kuris elektrochemiškai polimerizuojamas ant darbinio elektrodo. Tyrime vertinami tokie veiksnių kaip polimero paviršiaus morfologija ir sluoksnio storio įtaka jo stabilumui ant elektrodo [2].

Literatūra

1. Ramanavicius, S.; Jagminas, A.; Ramanavicius, A. Advances in Molecularly Imprinted Polymers Based Affinity Sensors (Review). *Polymers* 2021, 13, 974.
2. Boguzaite, R.; Pilvenyte, G.; Ratautaite, V.; Brazys, E.; Ramanaviciene, A.; Ramanavicius, A. Towards Molecularly Imprinted Polypyrrole-Based Sensor for the Detection of Methylene Blue. *Chemosensors* 2023, 11, 549.

PLAZMONINIŲ DALELIŲ SINTEZĖ BIOLOGINIŲ MOLEKULIŲ SERS NUSTATYMU

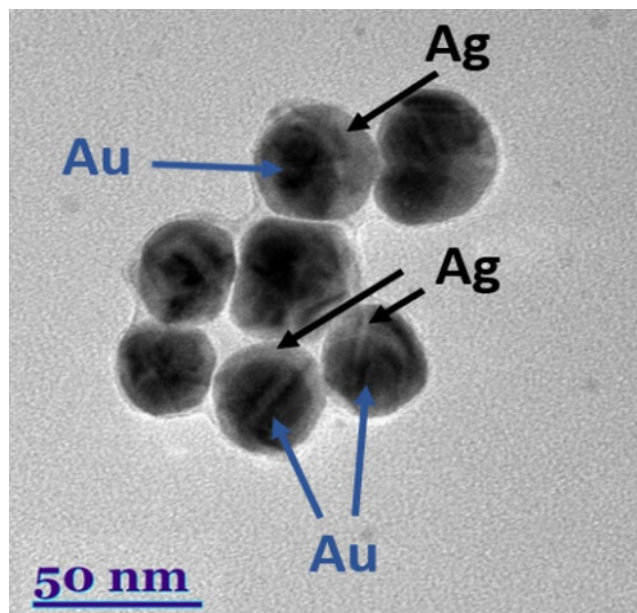
Gytautė Sirgėdaite^{1,2}, Martynas Talaikis^{1,2}, Lina Mikoliūnaitė^{1,2}

¹Fizinių ir technologijos mokslų centras, Organinės chemijos skyrius
Saulėtekio al. 3, LT-10257 Vilnius, el. p.: gytaute.sirgedaite@ftmc.lt

²Vilniaus Universitetas, Chemijos ir Geomokslų fakultetas, Chemijos Institutatas,
Naugarduko g. 24, LT-03225

Paviršiaus sustiprinta Ramano spektroskopija
SERS - virpesinės spektroskopijos metodas skirtas jautriai, nedestruktyviai ir selektyviai aptikti mažos koncentracijos analitės molekulę, pvz.: biologines molekules, organinius dažus, pesticidus. Metode, kaip SERS substratai, naudojamos metalinės aukso Au ir/ar sidabro Ag nanostruktūros savo plazmoninėmis savybėmis sustiprina Ramano sklaidą elektromagnetiniu (EM) ir/arba cheminiu stiprinimui. Siekiant praplėsti SERS metodo galimybes bandomos pritaikyti įvairios nanodalelių (ND) formos (sferinės, prizmės, kubinės, strypeliai, lazdelės), kiti metalai (Cu, Pt, Fe, Co) bei skirtingu metalų vienoje struktūroje derinimas (branduolio-apvalkalo, hibridinės ND).

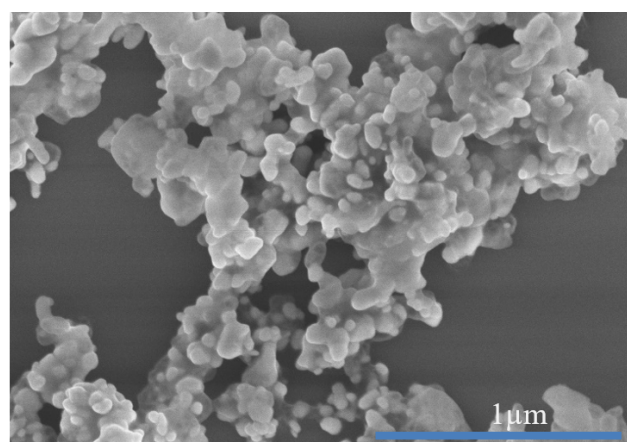
SERS tyrimams buvo susintetintos Au@Ag aukso branduolio ir sidabro apvalkalo nanodalelės. Keičiant sidabro druskos koncentraciją sintezėje, išgautas skirtingo storio sidabro sluoksnis. Au@Ag NP stiprinimas buvo išbandytas su 4-merkaptobenzoininės rūgšties (MBA) molekule bei gali būti pritaikomas adenino molekulės detekcijai.



1 pav. Au@Ag branduolio-apvalkalo nanodalelės
TEM vaizdas.

SERS plačiai ištirtas naudojant matomujų - artimoji infraraudonųjų spindulių sužadinimo bangų ilgiu diapazone. Tačiau daug svarbių organinių molekulių kaip balytmai, nukleobazės ir aromatinės amino rūgštys pasižymi stipria elektronine sugertimi ultravioletiniame (UV) bangų diapazone. [1] Dėl šių priežascių didėja susidomėjimas **ultravioletine paviršiaus sustiprinta Ramano spektroskopija UV-SERS**. Kai naudojamos sužadinimo bangos ilgis trumpesnis nei 400 nm, Au ir Ag praranda savo plazmonines savybes ir plazmoninis stiprinimo efektas nevyksta, tad UV-SERS tyrimams naudojami pereinamieji metalai, kaip platina Pt, paladis Pd, alumininis Al. Taip pat buvo pastebėtas UV-SERS stiprinimas naudojant ir vario nanodaleles. [2,3]

UV-SERS tyrimams mikrobangų reaktoriuje buvo susintetintos Cu nanostruktūros. Stiprinimas buvo išbandytas naudojant adenino molekulę, kai naudotas sužadinimo bangos ilgis 325 nm.



2 pav. Cu nanostruktūrų SEM vaizdas

Literatūra

1. R. Das, R.K. Soni, App. Surface Science **489**, p. 755-765 (2019).
2. A. Taguchi, Far- and Deep-Ultraviolet Spectroscopy. Springer, Tokyo, p. 145-158 (2014).
3. E.Kämmer, et al., The Journal of Physical Chemistry C, **116** (10), p. 6083-6091 (2012).

MAGNETITO NANODALELIŲ SINTEZĖ IR DEKORAVIMAS SIDABRO NANODALELĖMIS

Greta Zambžickaitė

Fizinių ir technologijos mokslų centras, Organinės chemijos skyrius
Saulėtekio al. 3, LT-10257 Vilnius, el. p.: greta.zambzickaite@ftmc.lt

Center for Physical Sciences and Technology, Department of Organic chemistry
Saulėtekio av. 3, LT-10257 Vilnius, email: greta.zambzickaite@ftmc.lt

Magnetinių dalelių sintezė sulaukia vis didesnio mokslininkų dėmesio dėl jų turimų savybių ir pritaikomumo, pradedant nuo MRT kontrastinių medžiagų, vaisto nešiklio sistemų, magnetinių separatorių, magnetinės hipertermijos medžiagų iki aplinkos, katalizės ir biologinių jutiklių sričių. Šios nanodalelės, pavyzdžiuui magnetitas, padengtos plazmoniniu, aukso ar sidabro, sluoksniu, gali būti naudojamos paviršiaus sustiprintoje Ramano spektroskopijoje. Magnetito dalelės yra tinkamos dėl savo stabilumo, biologinio suderinamumo, magnetiškumo savybių, nesudėtingos sintezės ir mažų finansinių resursų [1]. Sidabro nanodalelės (AgNP) pasižymi antimikrobinėmis ir priešvėžinėmis savybėmis ir yra naudojamos skatinti žaizdų, kaulų gjimą, kaip vakcinos pagalbinę medžiaga, antidiabetinis agentas ir biojutikliuose [2]. Taip pat buvo įrodyta, kad AgNP yra labai gerai pritaikomos katalizéje, fotokatalizéje ir įvairiuose plazmoniniuose įrenginiuose, pavyzdžiu, jutikliuose, kurie naudojami paviršiaus sustiprinto Ramano sklaidos efektui gauti[3].

Šiame darbe pristatomė magnetito nanodaleles, susintetintas mikrobangų reaktoriuje ir dekoruotas skirtingu formų ir dydžių sidabro nanodalėmis, kurios buvo susintetintos skirtingais sintezių metodais: šlapioji cheminė sintezė vandeninėje ar organinėje terpéje, sintezė mikrobangų technika naudojant dviejų pakopų temperatūros techniką. Susintetintos ir / arba dekoruotos nanodalelės buvo tiriamos rentgeno spektroskopija, skenuojamaja elektronine mikroskopija, transmisine elektronų mikroskopija, ultravioletine ir regimaja spektroskopija bei pritaikytos paviršiaus sustiprintoje Ramano spektroskopijoje.

The synthesis of magnetic particles triggers the interest of many scientists due to their relevant properties and wide range of applications in starting from MRI contrast agents, drug delivery systems, magnetic separators and hyperthermia agents and begging to the environmental, catalysis and biosensing fields. These nanoparticles capped with a plasmonic silver or gold layer could also be applied in surface-enhanced Raman spectroscopy due to signal enhancement for two reasons: the concentration of the sample using magnet and surface plasmons. Magnetite particles are suitable for such applications due to their stability, biocompatibility, simple synthesis, low price, and great magnetic response [1].

Silver nanoparticles (AgNP) have antimicrobial and anticancer properties and are applied in the promotion of wound repair and bone healing, or as the vaccine adjuvant, anti-diabetic agent, and biosensors [2]. AgNP have been proven to be very good candidates for applications in catalysis, photocatalysis and various plasmonics devices, for example in sensors utilizing surface-enhanced Raman scattering effect [3].

In this work, we present the magnetite nanoparticles, obtained via microwave assisted synthesis route and decorated by different shape and size silver nanoparticles which was synthesized using different synthesis methods: wet chemical synthesis in an aqueous or organic medium, synthesis by microwave through the two-step temperature technique. Obtained nanoparticles were investigated using X-Ray spectroscopy, scanning electron microscopy, transmission electron microscopy, ultraviolet-visible spectroscopy, and applied for surface-enhanced Raman spectroscopy.

References

1. Zambžickaitė G, Talaikis M, Dobilas J, Stankevič V, Drabavicius A, Niaura G, Mikoliunaite L, Microwave-Assisted Solvothermal Synthesis of Nanocrystallite-Derived Magnetite Spheres, Materials (2022); 15, 4008
2. Xu L, Wang YY, Huang J, Chen CY, Wang ZX, Xie H. Silver nanoparticles: Synthesis, medical applications and biosafety. Theranostics. (2020) 10(20); 8996-9031.
3. Wojtysiak S, Kudelski A, Influence of oxygen on the process of formation of silver nanoparticles during citrate/borohydride synthesis of silver sols, Colloids and Surfaces A: Physicochemical and Engineering Aspects (2012); 410,45-51

ELECTROCHEMICAL DETECTION OF CADMIUM IONS IN AQUEOUS SOLUTIONS USING MXENE-BASED SENSOR

Ilya Navitski¹, Šarūnas Žukauskas¹, Alma Ručinskienė², Arūnas Ramanavičius^{1,3}

1. Department of Nanotechnology, Center for Physical Sciences and Technology (FTMC), Sauletekio Av. 3, LT-10257 Vilnius, Lithuania, email: ilya.navitski@ftmc.lt
2. Department of Electrochemical Material Science, Center for Physical Sciences and Technology (FTMC), Sauletekio Av. 3, LT-10257 Vilnius, Lithuania
3. Department of Physical Chemistry, Institute of Chemistry, Faculty of Chemistry and Geosciences, Vilnius University (VU), Naugarduko g. 24, LT-03225 Lithuania

Heavy metal contamination has become a significant environmental and health problem caused by urbanization and industrialization. Among these heavy metals, cadmium is one of the particularly problematic due to its widespread use in various industries. The waste produced after its usage can contaminate water systems with cadmium ions, which pose a threat to both the environment and human health. Therefore, developing methods to accurately detect cadmium ions in aqueous solutions is crucial for public safety. One type of material that has garnered significant attention in the field of heavy metal ion sensing is MXenes [1,2]. Due to their advantages over other materials, we have chosen them for designing electrochemical sensor for cadmium ion detection.

The modification of the glassy carbon electrode (GCE) surface with a MXene-Nafion mixture was performed using the drop-casting method. Differential pulse voltammetry (DPV) was used to analyze the sensor's performance, focusing on factors such as sensitivity, limit of detection (LOD), and selectivity. All measurements were conducted in acetic buffer at pH 3.5 to 5.5. For stability testing, electrodes were prepared simultaneously and tested after varying periods of time have passed (up to 4 weeks).

The proposed mechanism for cadmium determination involves the reversible conversion between cadmium ions and cadmium oxide (CdO). The sensor demonstrated exceptional selectivity in the presence of various heavy metal ions. However, it also demonstrated its capability of detecting lead near cadmium signal. The sensing process was influenced by pH: the best sensitivity values with narrower and lower linear ranges were achieved in acidic environments. At pH 4.0, low LOD value of $0.45 \mu\text{M}$ and high sensitivity of $15.23 \mu\text{A}/(\mu\text{M} \cdot \text{cm}^2)$ were determined in the linear range of $0.5 \mu\text{M} - 2 \mu\text{M}$ (Fig. 1,2). Stability testing yielded consistent results for one week, followed by a gradual signal decline from the second week onward. This decline is primarily attributed to the oxidation of MXenes on the electrode surface.

In conclusion, the proposed sensor achieved relatively high sensitivity, low LOD, and exceptional selectivity in the presence of most

heavy metal ions. This work demonstrates an accurate and rapid method for detecting cadmium ions and lays the groundwork for future developments in this field.

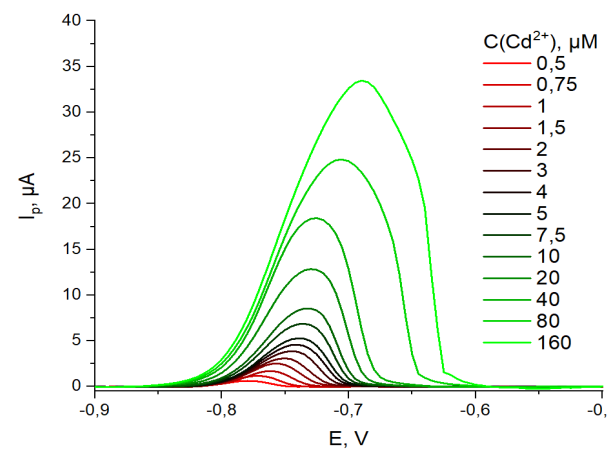


Fig. 1. Sensor's DPV signal after baseline subtraction at different cadmium concentration.

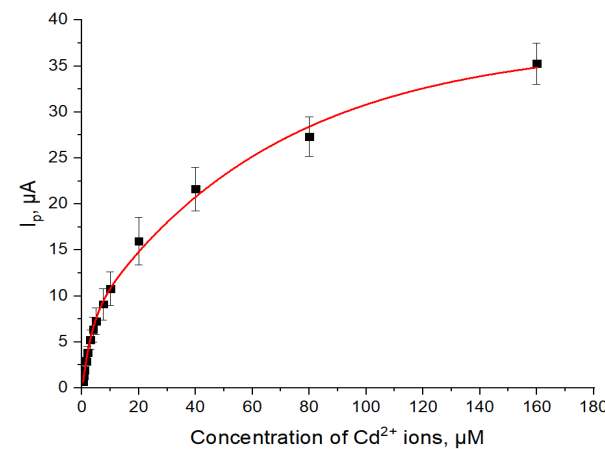


Fig. 2. Concentration curve of cadmium ion sensing ($n=3$) at pH 4.0.

References

1. Ilya Navitski et al. MXene-Based Chemo-Sensors and Other Sensing Devices (Nanomaterials, 14, 2024).
2. Sarunas Zukauskas et. al Electrochemical real-time sensor for the detection of Pb(II) ions based on $\text{Ti}_3\text{C}_2\text{T}_{x}$ MXene (Science of The Total Environment, 950, 2024).

DEVELOPMENT OF THE COMPTON-TO-PEAK METHODOLOGY FOR THE ANALYSIS OF GAMMA SPECTRA FOR THE CHARACTERISATION OF METALLIC RADIOACTIVE WASTES

Kristina Mikalauskienė, Marina Konstantinova, Darius Germanas,
Rita Plukienė, Elena Lagzdina, Artūras Plukis ir Vidmantas Remeikis

Center for Physical Sciences and Technology, Department of Nuclear Research
Saulėtekio av. 3, LT-10257 Vilnius, email: kristina.mikalauskiene@ftmc.lt

For the metallic radioactive waste (MRW) non-destructive characterization, the methodology based on gamma-ray spectrum analysis was developed by analyzing Compton-to-peak ratio to find out the photon attenuation due to absorption and scattering processes and interactions with matter in different geometry laboratory-made samples. This method allows separation of surface and volume contamination in metallic waste samples, which could latter on be applied for management, sorting and, if possible, deactivation of MRW.

Depending on the spectroscopy related problem to be solved the Compton-to-peak (or Peak-to-Compton) ratio is used in different studies, for instance: to improve determination of specific radionuclides from spectra applying Compton suppression technique [1], to improve determination of inventory of bituminized radioactive waste drums [2], to use for safeguards applications [3], etc.

In our study we combine theoretical MCNP6 modeling and experimental gamma spectra analysis to obtain the optimized parametres for source to material characterization by using different Compton scattering energy regions and full absorption peak ratios. Modeling of the different laboratory -made samples cases with two different detectors namely HPGe and CeBr₃ was performed by changing the radioactive source position, distance from the detector and shielding material thickness. Modeling have revealed which Compton energy region provides best information on the location of the radioactive nuclide in the metallic waste sample: is it distributed in the volume or at the surface of the metal, how to distinguish between homogeneous or heterogenous volumetric, point or planar contamination.

Two regions of interest (ROI): Compton backscatter and Compton edge have been investigated for two radionuclides ¹³⁷Cs (661.6 keV peak) and ⁶⁰Co (1173.2 keV peak):

Compton – to – Peak Ratio =

$$\frac{\text{ROI of Compton}}{\text{ROI of Peak}} \quad (1),$$

where ROI-region of interest.

The Compton backscattering region of the ¹³⁷Cs (661.6 keV) in the spectra obtained with the HPGe detector is around 180-195 keV, while the spectra obtained with the CeBr₃ detector have a much wider backscattering region (150-250 keV). The Compton edge region covers the energy range from the Compton maximum to the Compton edge, which

occurs at an energy of 477 keV for ¹³⁷Cs and 960 keV for ⁶⁰Co. These energy regions remain the same under different conditions for the same detector, such as different shielding thicknesses and different source geometries (point, volume, planar).

The method has been experimentally validated using known radioactive sources (point source ¹³⁷Cs A= 60.4±2.0 kBq and point sources of ⁶⁰Co A= 1209±70 kBq) for chosen measurement geometry and different shielding to mimic real metallic radioactive waste. Numerical simulations using MCNP6 were in good agreement comparing experimental data (Fig.1).

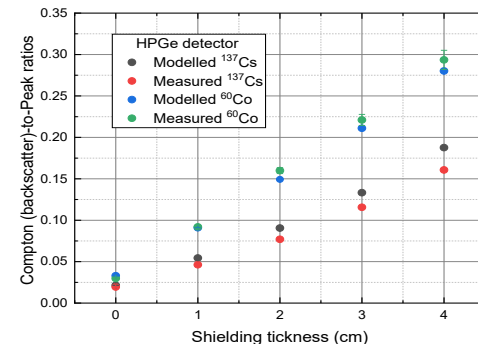


Fig. 1. Comparison of experimental and simulation of Compton (backscatter)-to-peak ratio for ⁶⁰Co and ¹³⁷Cs point sources using different shielding thickness acquired by the HPGe detector.

The results have shown that using Compton backscatter-to-peak ratio and peak intensity one can obtain better characterization of metal shielded source (up to the 6 cm) comparing with Compton edge-to peak ratio (up to 4 cm) for HPGe detector, and similarly for CeBr₃ detector: metal shielded source can be detected (up to the 5 cm) comparing with Compton edge-to peak ratio (up to 4 cm). The proposed analysis method can help to determine unknown ¹³⁷Cs and ⁶⁰Co sources distribution in the radioactive metal waste.

This research was partly funded by the 2020-2024 Euratom Research and Training Programme under grant agreement No 945098.

References

1. C. Egozi, S. Landsberger, W.S. Charlton, S.E. Betts, R. Winkler, Appl. Rad. And Isotop. 194 (2023) 110717
2. B. Perot, P. Pin, Nuclear Instruments and Methods in Physics Research A 671 (2012) 76-81.
3. R. A. El-Tayebany et al., IAEA Symposium on International Safeguards, 2015, 1-8
4. D.B. Pelowitz, MCNP6 User's Manual (2013), Version 1.0, Report LA-CP-13-00634, Los Alamos National Laboratory, New Mexico

DEVELOPMENT OF CHITOSAN-GRAFENE OXIDE-BASED NANOCOMPOSITES FOR REMOVAL OF NANO- AND MICRO-PLASTICS FROM FRESH WATER

Mahrosh Javed¹, Galina Lujanienė¹, Sergej Šemčuk¹, Vidas Pakštas², Kęstutis Mažeika³, Aušra Selskiene², Algirdas Selskis², Martynas Talaikis⁴

¹Department of Environmental Research, ²Department of Characterisation of Materials Structure,

³Department of Nuclear Research, ⁴Department of Organic Chemistry,

Center for Physical Sciences and Technology, Saulėtekio av. 3, LT-10257 Vilnius, Lithuania

email: mahrosh.javed@ftmc.lt

Flexible, durable and inexpensive synthetically produced materials, known as plastics, are made from polymers. Properties such as plasticity and their light weight make these plastics desirable for excessive use in all walks of life [1]. The wide use of these plastics also leads to improper disposal and uncontrolled degradation in the environment, resulting in fragmentation into smaller plastics as small as 100 nm in size nanoplastics (NPs), leading to white pollution. The presence of these plastic particles in water, air and soil has already been demonstrated in various studies [2]. Due to their small size (i.e. up to 100 nm) and the availability of many functional groups, these plastic particles can accumulate various heavy metals (such as lead, mercury, arsenic) and harmful pollutants, leading to water pollution. The harmful effects of NPs on nearby organisms and their occurrence in the aquatic environment have raised public health and environmental concerns worldwide.

In order to remove these nano-plastics, various methods such as magnetic separation, coagulation, adsorption and photolysis etc. have been used in recent years. Various adsorbents such as activated carbon, clay minerals, MOFs, silica, cellulose and chitosan-based composites, biochar, zeolites and graphene oxide composites have been used for the adsorption of nanoplastics [3]. Graphene oxide, which has many functional groups and large hydrophilicity, is a good catalyst and adsorbent, while chitosan, a deacetylated chitin, has many amino groups for adsorption [4]. Cellulose with available hydroxyl groups shows good adsorption ability. Various new research projects are currently looking at the differences in the properties of chemically pure plastic particles and real-life plastics.

This study deals with the preparation of chitosan-graphene oxide, magnetic chitosan-graphene oxide and cellulose-graphene oxide nanocomposites. For the preparation of these adsorbents, graphene oxide was synthesized using the modified Hummer's method and then crosslinked with a cellulose solution, a non-magnetic chitosan solution and a magnetic chitosan solution using glutaraldehyde as a crosslinking agent. For the preparation of

polyethylene terephthalate nano- and microplastics (PET-NMPs), discarded mineral water bottles were mechanically crushed and then ground using the Pulverisette 6 ball mill (FRITSCH, Germany) and settling techniques were applied. PET nanoplastics were also prepared by nanoprecipitation. For this purpose, PET plastics were dissolved in TCA and then 50 ml of this plastic solution was mixed with a 5 % PVA solution in a fume hood for 2 hours with constant stirring to allow nanoprecipitation and stabilize the nanoplastics. The resulting solution was then sonicated for 10 minutes to reduce the size of the nanoplastics and centrifuged at 4000 rpm to separate the nanoplastics. The technique of nanoprecipitation was also used to produce nano- and microplastics from food packaging polystyrene. The resulting composites and nano- and microplastics were characterized using XRD, FTIR and SEM techniques. The obtained composites were pre-tested for the adsorption of prepared nano- and microplastics samples and will be used in further studies of adsorption experiments.

References

1. Li, X., T.-C. Ling, and K.H. Mo, *Functions and impacts of plastic/rubber wastes as eco-friendly aggregate in concrete-A review*. Construction and building materials, 2020. 240: p. 117869. <https://doi.org/10.1016/j.conbuildmat.2019.117869>
2. Bibi, A., et al., *A review on state-of-the-art detection techniques for micro-and nano-plastics with prospective use in point-of-site detection*. Comprehensive Analytical Chemistry, 2023. 101: p. 143-196. <https://doi.org/10.1016/bs.coac.2022.11.003>
3. Tyagi, U., *Sustainable and low-cost biomass derived adsorbents for the removal of toxic contaminants from wastewater: Approaches and future perspective*. Waste Management Bulletin, 2024. <https://doi.org/10.1016/j.wmb.2024.05.010>
4. Ahmed, M., B. Hameed, and E. Hummadi, *Review on recent progress in chitosan/chitin-carbonaceous material composites for the adsorption of water pollutants*. Carbohydrate polymers, 2020. 247: p. 116690. <https://doi.org/10.1016/j.carbpol.2020.116690>

THE ROLE AND POTENTIAL OF GREEN INFRASTRUCTURE IN FILTERING TRANSPORT-GENERATED MICROPLASTICS

¹Abdullah Khan, ²Valda Araminienė, ¹Ieva Uogintė, ¹Lina Davulienė, ¹Austėja Burbulytė,
²Iveta Varnagirytė-Kabašinskienė, ²Valentinas Černiauskas, ²Valda Gudynaitė-Franckevičienė,
³Algis Džiugys, ³Edgaras Misiulis, ¹Steigvilė Byčenkienė

¹SRI Centre for physical sciences and technology (FTMC),
Saulėtekio Ave. 3, Vilnius, Lithuania, abdullah.khan@ftmc.lt

²Lithuanian Research Centre for Agriculture and Forestry,
Instituto al. 1, Akademija, LT-58344 Kėdainiai distr., Lithuania

³Lithuanian Energy Institute, Breslaujos st. 3, LT-44403 Kaunas, Lithuania

Tire and road wear particles (TRWPs) are major non-exhaust pollutants from vehicles, posing serious environmental and health risks [1]. Each year, approximately 6.1 million tons of TRWPs are released into the environment, with concentrations reaching up to 2.6 kg per person in Europe [2]. Due to their widespread dispersion and inhalation potential, these particles can lead to significant health problems. This study investigates how various green infrastructure components, such as vegetation and barriers, can effectively capture and reduce TRWPs. By assessing their efficiency, the research aims to provide insights for urban planning to mitigate microplastic pollution and improve public health in urban environments.

In Kaunas City ($54^{\circ}51'00.7''N$ $24^{\circ}01'46.5''E$), Lithuania, a hedge of *Thuja occidentalis* (0.6 m width, 1.5 m height, 19 m length) was employed to simulate green space (Fig. 1). Over 24 hours, airborne microplastics (MPs) were sampled using Petri dishes with glass fiber filters placed at distances of -1 m (adjacent to the street), 0 m (within the hedge), +1 m, and +2 m from the hedge. Samples were collected monthly from June to October 2023. The microscopic analysis assessed MPs' abundance, morphology, and color, while chemical composition was determined with a LUMOS II spectrometer.

The results show that MP levels vary from 2.8 to 0.25 MP/cm², depending on proximity to streets. Fragments and black-colored particles dominate the samples, accounting for 90-100% of the total. Most microplastics detected during the sampling were smaller than 100 microns. Modeling data for the real-world scenario revealed a minimal reduction in microplastic pollution, primarily limited to the area immediately behind the hedge, as most particles were able to pass over it. The MPs were predominantly composed of polypropylene and polyurethane (40.9%), materials commonly found in vehicle tires.

The MPPD model results indicate that polypropylene, polyethylene, polyurethane, and particulate organic matter (POM) predominantly deposit in the upper respiratory tract (URT), with deposition percentages of 93%, 94%, 96%, and 96%, respectively. The tracheobronchial (TB) region exhibits lower deposition rates, ranging from 3% to 5%, while the alveolar (AI) region shows the least deposition at 1% to 2%. These findings highlight the tendency of these particles to accumulate primarily in the URT and TB regions.

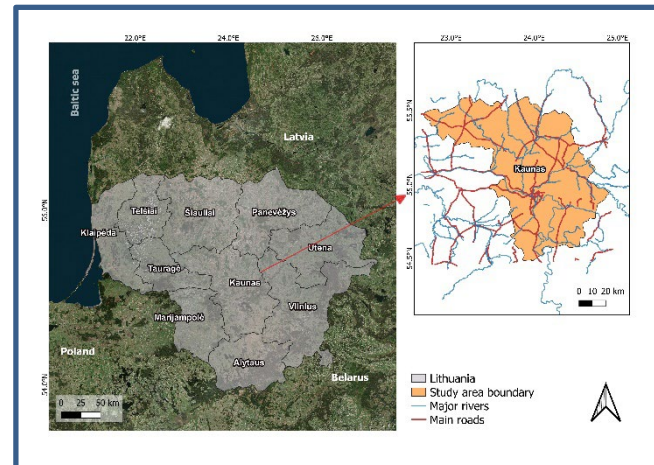


Fig. 1. Study area map in Kaunas city, Lithuania, to understand transport-related pollution dynamics.

References:

- Klöckner, Philipp, et al. "Characterization of tire and road wear particles from road runoff indicates highly dynamic particle properties." *Water Research* 185 (2020): 116262.
- Wang, Yu, et al. "A review of tire wear particles: Occurrence, adverse effects, and control strategies." *Ecotoxicology and Environmental Safety* 283 (2024): 116782.

APPLICATION OF TiO_2 -BASED NANOCOMPOSITES FOR THE PHOTOCATALYTIC DEGRADATION OF LDPE MICROPLASTICS

Sonata Pleskytė, dr. Ieva Uogintė, dr. Steigvilė Byčenkienė

Center for Physical Sciences and Technology, Department of Environmental Research
Saulėtekio av. 3, LT-10257 Vilnius, email: sonata.pleskyte@ftmc.lt

Microplastics, which are less than 5 mm in size, are widely recognized as a common micro-pollutant in various ecosystems. The existing methods for plastic waste management do not affect the reduction of plastics and most likely even increase the formation and presence of microplastics in the environment [1]. Therefore, there is an urgent need for new pathways and innovative materials that could be perceived as effective and less hazardous for the environment.

Photocatalytic degradation is considered one of the most promising techniques for microplastic removal, as it can be carried out under milder conditions, compared to chemical or biological degradation. One of the most widely used photocatalysts is TiO_2 due to its excellent photoactivity, chemical stability, and low-cost [2]. To improve the properties of TiO_2 , these particles are often modified with other metal oxides, noble metals, organic polymers, and natural or bio-based materials. However, little is known about the use of TiO_2 nanocomposites with clay minerals for the photocatalytic degradation of microplastics.

In this study, we examined an application of TiO_2 -based photocatalysts, including TiO_2 NPs, TiO_2 -kaolinite, and TiO_2 -montmorillonite for the photocatalytic degradation of LDPE (300 μm). The synthesized nanomaterials were characterized by XRD, TEM, and UV-VIS methods. The photocatalytic test was carried out in a closed reaction chamber at a wavelength of 365 nm. To better understand the interaction between LDPE and TiO_2 -based nanomaterials in aqueous solution, we investigated the influence of four variable parameters: reaction time, materials ratio, pH value, and ionic strength. The highest mass loss of LDPE was observed after 480 minutes, in an acidic medium with a mass loss of 30%. The analysis of the different conditions of the photocatalytic degradation reaction showed the importance of reaction optimization to achieve a higher degradation efficiency with less harsh treatment.

Overall, these results emphasize the potential of TiO_2 -based nanocomposites with clay minerals moving towards efficient, low-cost, and more environmentally friendly techniques to reduce microplastic pollution.

References

- [1] G. Suzuki et al., Environ. Pollut. 303, 2022.
- [2] W. Li, W. Zhao, H. Zhu, Z. J. Li, and W. Wang. J. Mater. Chem. A, 11, 2023.

THE ROLE OF THE SEA TRANSPORT FOR SUBMICRON AEROSOL CHEMICAL COMPOSITION

Agnė Minderytė¹, Axel C. Eriksson², Erik Ahlberg³, Steigvilė Byčenkienė¹, Adam Kristensson³ and Julija Pauraite¹

¹Center for Physical Sciences and Technology, Department of Environmental Research
Saulėtekio av. 3, LT-10257 Vilnius, email: agne.minderyte@ftmc.lt

²Lund University, Department of Physics, Lund, 221 00, Sweden

³Lund University, Department of Design Sciences, Lund, 221 00, Sweden

While there are significant advancements in characterizing aerosols over land at systematic long-term measurements and various continental and global network stations, there is still a need for further exploration of their chemical properties in marine regions. Aerosol particle chemical composition and mass concentrations undergo significant changes due to long-range air mass transport. In addition, the role of sea and oceans for aerosol chemical composition remains poorly understood. While previous studies have explored shipping-related aerosol properties [1] or aerosol size distributions during connected flow events across the Baltic Sea [2], few studies have comprehensively investigated the impact of PM₁ (particulate matter with a diameter smaller than 1 μm) removal over the sea, leaving a gap in our understanding of aerosol dynamics.

We have examined 4 months of data (December 2017 to March 2018) of PM₁ chemical composition in two observation stations: Hyltemossa (Sweden), set in a rural environment, and Preila (Lithuania), situated in a marine environment. Simultaneous measurements of aerosol chemical composition (organic matter, nitrate, ammonium, chloride, sulphate) were performed with Time-of-Flight Aerosol Chemical Speciation Monitor (ToF-ACSM, Aerodyne Research, Inc) in Hyltemossa and Q-ACSM in Preila. Equivalent black carbon (eBC) mass concentrations were measured using Aethalometers AE33 and AE31 (Magee Scientific) in Hyltemossa and Preila, respectively. The study investigated the impact of the sea on submicron particle composition during 14 long-range air mass transport events (in total 100 hourly trajectories) between Hyltemossa and Preila (Figure 1). The backward air mass transport trajectories were modelled using the Hybrid Single-Particle Lagrangian Integrated Trajectory (HYSPLIT) model with the Global Data Assimilation System (GDAS) meteorological databases at the NOAA Air Resources Laboratory's web server.

During the campaign, Hyltemossa consistently showed a lower PM₁ concentration (6.3 mg/m³) compared to Preila (11.2 mg/m³). However, during the observed events, Preila experienced cleaner air masses with PM₁ levels lower than those observed in Hyltemossa. The observed decrease of 40% in PM₁ concentration across the two sites

suggests that the aerosol mass is removed during the long-range transport over the Baltic Sea. The highest relative change per event hour was observed for sulphate (-4.9%). The aerosol mass removal per hour was stronger during the events with precipitation (-7.2%). As anticipated, chloride was the only component to consistently show an increase (3.9%) after the long-range transport over the sea.

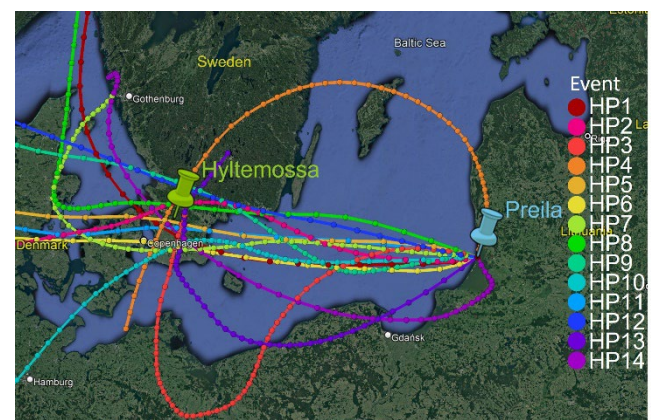


Fig. 1. Map over the southern Baltic Sea and the path of one selected 48-hour backward air mass trajectory for each of the investigated HP events.

The study, with two locations across the Baltic Sea and overlapping measurements of a similar nature, provides highly interesting material for studies of atmospheric chemistry. The event classification suggested in our study allows us to assess the effects of sea, precipitation and land on the PM₁ concentration and composition.

This work was supported by ACTRIS Sweden, which is a National Research Infrastructure funded jointly by the Swedish Research Council (Grant 2021-00177) and the six Swedish Research Performing Organizations involved. Co-funded by the Erasmus+ programme of the European Union for student mobility.

References

1. Ausmeel, S., Eriksson, A., Ahlberg, E., Sporre, M. K., Spanne, M., Kristensson, A. (2020) Atm. Chem. Phys. 20, 15, 9135-9151.
2. Kecorius, S., Kivekäs, N., Kristensson, A., Tuch, T., Covert, D. S., Birmili, W., Lihavainen, H., Hyvärinen, A. P., Martinsson, J., Sporre, M. K., Swietlicki, E., Wiedensohler, A., Ulevicius, V. (2016) Oceanologia 58, 1, 1-12.

KCL SLENKSTINĖS KONCENTRACIJOS RIBŲ TYRIMAS LAZERINĖJE NANODELELIŲ GENERACIJOJE, SIEKIANT PAGERINTI STABILUMĄ IR SERS STIPRINIMĄ

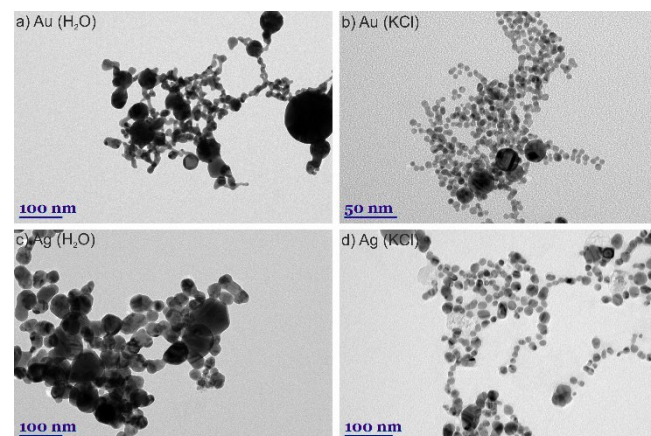
Vita Petrikaitė, Evaldas Stankevičius

Fizinių ir technologijos mokslų centras, Lazerinių technologijų skyrius
Savanorių per. 231, LT-02300 Vilnius, el. p.: vita.petrikaite@ftmc.lt

Aukso ir sidabro nanodalelės pasižymi plačiomis elektromagnetinės sugerties juostomis ir lokalizuotu paviršiaus plazmonų rezonansu, kuris lemia jų optines savybes. Dėl unikalių savybių [1] jos naudojamos jutikliams, biologinėms technologijoms, paviršiaus sustiprintai Ramano sklaidai (SERS) [2], katalizatoriams, nanotechnologijoms, ženklinimui ir elektronikai. Lazerinė abliaacija igavo pagreitį kaip švarus ir aplinkai nekenksmingas nanodalelių gamybos būdas, nereikalaujantis papildomo toksiškų medžiagų valymo [3]. Tačiau lazerinės abliacijos metu sunkumų kelia nanodalelių polikis i agregacija, kuris riboja tolimesnį jų panaudojimą. Siekiant išvengti dalelių agregacijos, naudojamos pridėtinės medžiagos, kurios užteršia švarų gamybos metodą. Šiame tyrime nagrinėjamas biologiškai suderinamos medžiagos - kalio chlorido (KCl) - veiksmingumas siekiant išvengti dalelių agregacijos. Nors žinoma, kad druska sukelia aggregaciją [4], pastebėjome, kad tam tikros KCl koncentracijos gali sulėtinti šį procesą. Tokios ribinės koncentracijos buvo analizuojamos šiame darbe.

Šio tyrimo metu buvo stebimas aukso, sidabro ir jų mišinio nanodalelių, susidariusių skirtinės koncentracijos KCl tirpaluose, aggregacijos greitis ir ekstinkcija 8 savaičių laikotarpiu. Aukso ir sidabro nanodalelės buvo generuojamos iš tūrinių taikinių, panardintų į 20 ml skirtinės koncentracijos KCl druskos tirpalus: 0 mM - 20 mM. Taikiniai buvo apdoroti fokusuotu Nd:YAG lazeriu. Kas savaitę buvo registratoriu gautų koloidinių tirpalų ekstinkcijos spektrai ir nuotraukos. Taip pat buvo analizuojama dalelių morfologija, SERS signalo stiprumas ir zeta potencialas. Mūsų rezultatai rodo, kad lazerio abliaacija vandenye ir druskų tirpaluose sukuria sferinės formos nanodaleles su neigiamu zeta potencialu (nuo -16 mV iki -58,8 mV).

Palyginimas pateiktas 1 paveiksle. Adsorbuoti chlorido jonai ant sidabro nanodalelių pasireiškė žemo dažnio SERS juosta ties 242 cm^{-1} . Geresnis KCl koncentracijos poveikio tauriųjų metalų nanodalelių savybėms supratimas gali padėti patobulinti generavimo procesus ir sukurti nanodalelių sistemas, pasižyminčias didesniu stabilumu ir SERS aktyvumu.



1 pav. Aukso (a-b) ir sidabro (c-d) nanodalelių TEM vaizdai: (a) Au ND vandenye; (b) Au ND KCl tirpale; (c) Ag ND vandenye; (d) Ag ND KCl tirpale.

Literatūra

1. N. Li, P. Zhao, D. Astruc, Anisotropic gold nanoparticles: synthesis, properties, applications, and toxicity, *Angew. Chem., Int. Ed. Engl.*, 53, 1756–1789 (2014).
2. E. Stankevičius, I. Ignatjev, V. Petrikaitė, A. Selskis, G. Niaura, Gold Nanoparticles Generated Using the Nanosecond Laser Treatment of Multilayer Films and Their Use for SERS Applications, *ACS omega*, 6, 33889-33898 (2021).
3. S. Dolgaev, A. Simakin, V. Voronov, G.A. Shafeev, F. Bozon-Verduraz, Nanoparticles produced by laser ablation of solids in liquid environment, *Applied surface science*, 186 (2002) 546-551.
4. G. Wang, W. Sun, Optical limiting of gold nanoparticle aggregates induced by electrolytes, *J. Phys. Chem. B*, 110, 20901-20905 (2006).

LAZERIU SUFORMUOTŲ NANODARINIŲ MORFOLOGINIS VALDYMAS PAVIRŠIUMI SUSTIPRINTAI RAMANO SPEKTROSKOPIJAI

Kernius Vilkevičius, Ilja Ignatjev, Evaldas Stankevičius

Fizinių ir technologijos mokslų centras, Lazerinių technologijų skyrius
Savanorių pr. 231, LT-02300 Vilnius, el. p.: kernius.vilkevicius@ftmc.lt

Tiesioginis lazerinis rašymas yra perspektyvus greito ir tikslaus mikroapdirbimo metodas. Apdorojant plonas metalo dangas pavieniais itin trumpais lazerio impulsais, dangos paviršiuje suformuojami metaliniai dariniai [1]. Darinių morfologija labai priklauso nuo impulso energijos - didėjant energijai struktūros keičiasi nuo sferinio iškilimo, vadinamo gumbeliu, iki pailgos antenos [2]. Apšvitinus šias metalines struktūras spinduliuote, jose itin sustiprinamas lokalus elektromagnetinis laukas, kuris gali būti išnaudotas paviršiaus sustiprintoje Ramano spektroskopijoje (SERS). Dėl šio stiprinimo žymiai padidinamas ant metalinio paviršiaus esančių molekulių neelastinės sklaidos signalas, tad padidėja aptikimo jautrumas ir pagerėja minimali aptikimo riba. Signalo sustiprinimas priklauso nuo struktūros morfologijos, kadangi struktūros su aštriaisiais kampais ir taip vadinamais „karštaisiais taškais“ gerokai padidina signalo intensyvumą [3].

Tyrimo metu buvo suformuotos nuo energijos priklausančios periodinės auksinės struktūros ant skirtinį aukso dangos storiją. Formavimui buvo naudojami 343 nm bangos ilgio impulsai. Ant suformuotų darinių buvo nusodintas 4-merkaptobenzoinės rūgšties (4-MBA) monosluoksnis, kuris buvo naudojamas sustiprinto

Ramano signalo nustatymui. Matavimų metu buvo tiriamas tiek darinių morfologijos, tiek metalo storio įtaka SERS signalo stiprinimui. Nustatyta, jog keičiant darinių formą galima tiksliai valdyti signalo stiprinimą. Apdirbimui naudojant didesnes impulsų energijas ir suformuojant antenos formos struktūras, pasiekiamas didžiausias signalo stiprinimas, kadangi ties darinių viršūnėmis susidaro „karštieji taškai“. Keičiant aukso dangos storiją, papildomai galima kontroliuoti tokijų antenų morfologiją bei dar labiau sustiprinti fiksuojamą Ramano signalą. Pastarųjų darinių SERS signalo stiprinimo faktorius siekia 10^7 eilę, kuri gali būti pakankama pritaikyti tiksliam molekulių aptikimui ir nustatymui mažomis koncentracijomis.

Finansavimą skyrė Lietuvos mokslo taryba, sutarties Nr. S-MIP-23-32.

Literatūra

1. E. Stankevičius, K. Vilkevičius, M. Gedvilas, E. Bužavaitė-Vertelienė, A. Selskis, Z. Balevičius, Adv. Opt. Mater., **9**, 2100027, (2021).
2. D. Pavlov, S. Syubaev, A. Kuchmizhak, S. Gurbatov, O. Vitrik, E. Modin, S. Kudryashov, X. Wang, S. Juodkazis, M. Lapine, Appl. Surf. Sci., **469**, 514-520, (2019).
3. Z. Y. Li, Adv. Opt. Mater., **6**, 1701097, (2018).

SKAIDRINANČIŲ DANGŲ FORMAVIMAS ANT 3D MIKROOPTINŲ KOMPONENTŲ NAUDODJANT ATOMINIŲ SLUOKSNIŲ NUSODINIMO TECHNOLOGIJĄ

D. Astrauskyte¹, K. Galvanauskas², D. Gailevicius², M. Drazdys¹, M. Malinauskas², L. Grineviciute¹

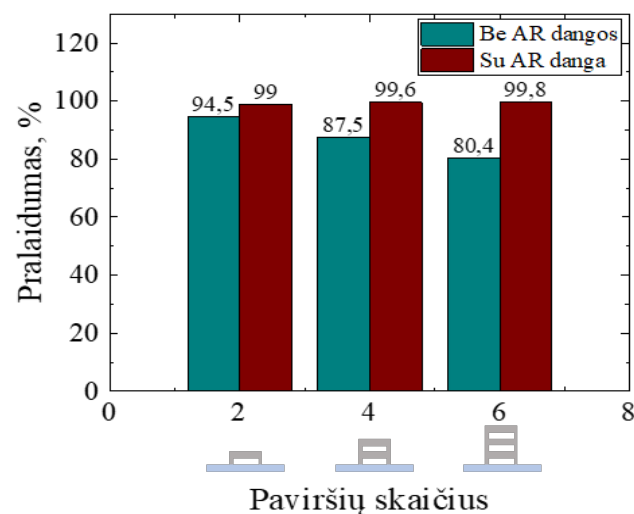
¹ Fizinių ir technologijos mokslų centras, Lazerinių technologijų skyrius
Savanorių pr. 231, LT-02300 Vilnius
El.p.: dariaja.astrauskyte@ftmc.lt

² Vilniaus universitetas, Fizikos fakultetas, Lazerinių tyrimų centras
Saulėtekio al. 10, LT-10223, Vilnius

Tiesioginio lazerinio rašymo (LDW – angl. k. *laser direct writing*) metodas leidžia suformuoti sudėtingos formos mikrooptinius komponentus, pavyzdžiui, mikroobjektyvus, susidedančius iš kelias aukštais išdėstytais mikrolėšių [1]. Tokios daugiaaukštės struktūros dėl didelio paviršių skaičiaus pasižymi dideliais atspindžių nuostoliais. Mikrooptikos atspindžių sumažinimui ir pralaidumo padidinimui gali būti naudojamos skaidrinančios (AR - angl. k. *antireflective*) dangos. Tačiau dažniausiai optinių dangų formavimui naudojami fizinių garų nusodinimo (PVD - angl. k. *physical vapor deposition*) metodai yra neefektyvūs nusodinant dangas ant 3D pagrindų. Atominių sluoksnių nusodinimo (ALD - angl. k. *atomic layer deposition*) technologija yra preciziškas plonų sluoksnių formavimo metodas, leidžiantis nusodinti dangas ant sudėtingos formos pagrindų [2]. Šios technologijos principas yra atomo storio sluoksnio suformavimas vieno ALD ciklo metu vykstant pirmatakių reakcijoms su paviršiumi. Šiame darbe buvo pademonstruotos ALD technologijos galimybės formuojant plonus sluoksnius ant daugiaaukštų mikrooptinių elementų. Optinės dangos buvo formuojamos ant 3D mikrooptinių komponentų naudojant plazminę ALD metodą. Mikrooptika buvo pagaminta naudojant LDW metodą iš hibridinio organinio-neorganinio polimero SZ2080™. AR danga susidėjo iš 23 nm storio titano oksido sluoksnio ir 132 nm storio aluminio oksido sluoksnio. TiO₂ ir Al₂O₃ plonų sluoksnių formavimui buvo naudojami tetrakisdimetilaminotitanato ir trimetilaluminio pirmatakai, atitinkamai. Oksidavimui buvo naudojama deguonies plazma. Visos dangos buvo nusodinamos 60°C temperatūroje. Mikrostruktūrų paviršiaus morfologija buvo jvertinta naudojant atominių jėgų mikroskopiją. Plonų sluoksnių įtaka mikrolėšių geometrijai buvo nustatyta naudojant optinę profilometriją.

Daugiaaukštų komponentų pralaidumas buvo išmatuotas naudojant optinę mikroskopiją.

AR danga nusodinta naudojant ALD technologiją sumažino hibridinio polimero SZ2080™ vieno paviršiaus atspindį nuo 3.3% iki 0.1% 633 nm bangos ilgyje. Taip pat buvo pastebėta, kad AR danga nepakeitė mikrolėšių geometrijos ir sumažino mikrostruktūrų paviršiaus šiurkštumą nuo 3.4 nm iki 2.6 nm. Be to, 1-ame paveiksle yra pateiktos daugiaaukštų mikrostruktūrų pralaidumo vertės prieš ir po AR dangos nusodinimo. AR danga padidino trijų aukštų mikrostruktūrų pralaidumą nuo 80% iki 99%.



1 pav. Skirtingų paviršių skaičių turinčių mikrostruktūrų pralaidumas 633 nm bangos ilgyje.

Literatūra

1. K. Galvanauskas, et al. High-transparency 3D micro-optics of hybrid-polymer SZ2080™ made via Ultrafast Laser Nanolithography and atomic layer deposition. *Opt. Open* 104228 (2023).
2. D. Astrauskytė, et al. Anti-Reflective Coatings Produced via Atomic Layer Deposition for Hybrid Polymer 3D Micro-Optics. *Nanomaterials* 13(16):2281 (2023).

NONLINEAR HEAT DISTRIBUTION IN HIGH AVERAGE POWER END-PUMPED Yb:YAG ACTIVE MEDIUM AMPLIFIERS AND ITS EFFECT ON DEPOLARIZATION

Aivaras Kazakevičius^{1,2}, Andrejus Michailovas^{1,2}

¹Center for Physical Sciences and Technology, Department of Laser Technologies
Saulėtekio al. 3, LT-10257 Vilnius, email: aivaras.kazakevicius@ftmc.lt

² UAB Ekspla, Savanorių pr. 237, LT-02300 Vilnius

Lasers are already established tools for various applications spanning industrial material processing, measurement and metrology devices, instrumentation for scientific experiments and many others. Many applications require ever increasing pulse energy and average power of the laser sources to either increase the speed of the process in which the laser is applied or to create ultrahigh intensity radiation that allows to perform novel scientific research.

Regardless of the optical setup geometry and gain medium material, the output power of a solid-state laser device is limited by the thermally induced stress in the gain medium. Under high pump power, the non-uniform material heating induces elastic stress in the gain medium. The induced elastic stress causes the amplifier to act as a birefringent material and distort the polarization state of the signal that is passing through the amplifier, which leads to losses.

Several methods are commonly used to compensate the thermally induced depolarization losses in linear amplifier and resonator setups. One of the most straightforward approaches is to use 90° polarization rotation either between two identical active elements or between the first and the second pass through the same active element. This can be achieved by using a Faraday rotator or a quarter wave-plate in the amplifier optical setup. However, both approaches are ineffective at high signal and pump average powers. Faraday rotators are susceptible to thermal lensing at high signal powers and B integral accumulation at high signal pulse energy levels. The insertion of the quarter wave plate does not fully compensate the depolarization losses due to the fact that this approach changes the relation between the depolarized light level and dissipated heat in the amplifier crystal. It was shown that this method is only effective at relatively low dissipated heat levels [1]. Alternatively, a uniaxial crystal can be used to compensate depolarization. While this method has the advantage to be used in a single pass geometry, the compensation is incomplete similarly to the quarter wave plate method [1]. Also, an optical setup not limited by the average output power has been suggested, in which a parallel axicon was used as a compensating element. Although the method has numerous advantages, the major challenge is the manufacture of a parallel axicon [1].

An ideal depolarization compensation method would allow to mimic the phase shift introduced by the thermally stressed active medium and thus completely eliminate the depolarization losses. Therefore, a solution to compensation problem requires an exact description of phase distortion in the gain medium and an optical element or an optical setup that allows precise compensation of the introduced phase shifts. Recent development in directly laser written optical components allowed to craft such laser components. It was shown, that under high intensity laser irradiation, the structure of

glass can be rearranged into a periodic self-organized structure consisting of decomposed material planes and exhibiting birefringence [2]. This discovery allowed to manufacture various phase shifting elements including a spatially variable wave plate (SVWP), which can be characterized by varying retardance as a function of wave plate radius.

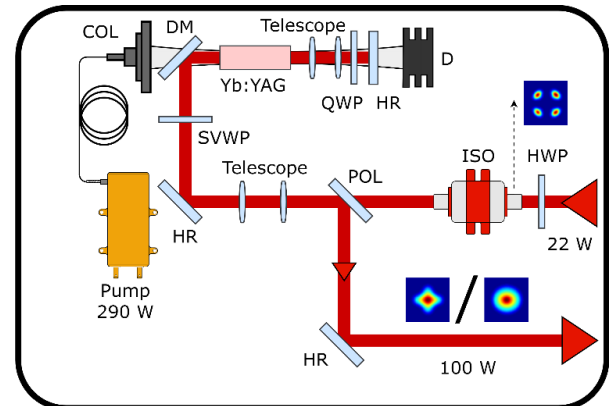


Fig. 1. Experimental setup of the Yb:YAG amplifier analyzed by the model. QWP and HWP - quarter-wave and half-wave plates, COL - beam collimator, ISO - optical isolator, POL - thin-film polarizer, DM - dichroic mirror, SM - spherical mirror, HR - high reflectivity mirror, SVWP - spatially variable wave plate, D - beam dump.

Successful demonstrations of depolarization losses compensation using spatially variable wave plates in high average power end-pumped rod-type amplifiers have been previously demonstrated by our group [3]. Although substantial reduction of depolarization losses has been achieved, the effect of this compensation method on the output beam parameters, especially on the output beam profile and quality, is important to study for routine application of SVWPs in industrial grade lasers.

We report the results of theoretical simulation of a 10 mJ, 100 W average power end-pumped Yb:YAG amplifier (fig. 1). The simulation resulted in good quantitative and qualitative agreement with the experiment in terms of depolarization losses, the output beam quality and the features of the output beam. The results suggest a strategy to improve depolarization losses compensation. It is commonly assumed that the phase retardance profile inside a thermally stressed gain medium is parabolic. However, our simulations suggest that the retardance profile can be described with a high order polynomial function with better accuracy.

References

- [1] A. Starobor, O. Palashov, *Opt. Commun.* **40**, 468 (2017).
- [2] M. Beresna, M. Gecevičius, P. G. Kazansky, *AOP*, **6**, 293 (2014)
- [3] L. Veselis, R. Burokas, o. Ulčinas, T. Gertus, K. Michailovas, A. Michailovas, *Appl. Opt.* **60**, 7164 (2021).

SODA-LIME STIKLO APDIRBIMAS LAZERIU NUO APATINĖS BANDINIO PUSĖS PASITELKIANT GHZ PAPLIUPŪ REŽIMĄ

Miglė Mackevičiūtė, Juozas Dudutis, Paulius Gečys

Fizinių ir technologijos mokslų centras, Lazerinių tyrimų skyrius
Savanorių pr. 231, LT-02300 Vilnius, el. p.: migle.mackeviciute@ftmc.lt

Lazerinis papliupū (angl. *burst*) režimas gali pagerinti įvairių medžiagų apdirbimą (stiklo [1], polimerų [2], metalų [3], puslaidininkų [4]), pluoštą fokusujant į viršutinį bandinio paviršių. Tačiau tiesioginės abliacijos efektyvumą riboja plazmos bei apdirbimo produkto ekravimas [5]. Taip pat dėl pluošto sklaidos nuo jau išabliuotų sienelių, suformuojamos V formos sienelės. Todėl storesnių medžiagų pjovimui reikalingas platesnis pjūvio plotis, prailginantis proceso trukmę.

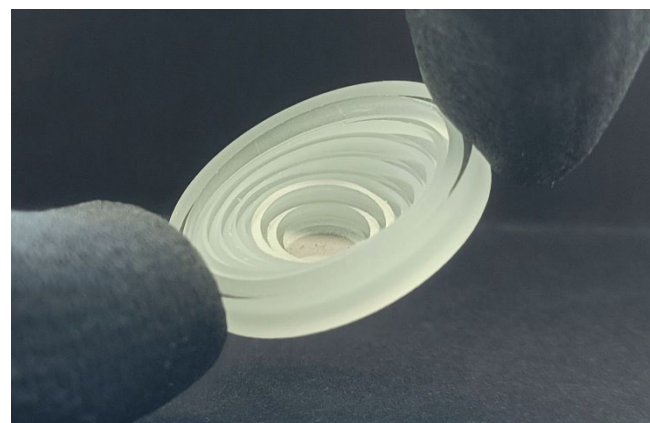
Medžiagas apdirbant nuo apatinės pusės, galima išvengti plazmos ir išabliuotų dalelių ekranavimo bei suformuoti stačias sienelės. Todėl ši apdirbimo technologija leidžia pasiekti aukštesnį pjovimo efektyvumą bei greitį. Tačiau šis pjovimo būdas gali būti pritaikomas tik skaidrioms naudojamai lazerio spinduliuotei medžiagoms. Todėl lazerinis apdirbimas nuo apatinės pusės dažniausiai taikomas stiklams. Tačiau vis dar trūksta publikacijų tiriančių stiklo apdirbimą nuo apatinės pusės naudojant papliupų režimą. Šio darbo tikslas – ištirti 4.8 mm storio soda-lime stiklo pjovimą lazeriu nuo apatinės bandinio pusės naudojant GHz papliupų režimą.

Eksperimentas atliktas su Carbide CB3-40W femtosekundiniu lazeriu („Light Conversion“) generuojančiu 2.5 GHz papliupas. Tyryme naudotas 1030 nm lazerio bangos ilgis ir 5 – 20 ps impulso trukmės (charakterizuotos FWHM intensyvumo aukštyje). Pluošto pozicija X, Y ašyse buvo valdoma galvanometriniu skeneriu (excelliScan 14, Scanlab). Galvanoskenerio ir 100 mm židinio nuotolio telecentrinio lėšio pozicijos Z ašyje buvo valdomos su linijinio poslinkio sistema (8MT165, Standa).

Pjovimo pradžioje pluoštas buvo sufokusuotas į apatinį bandinio paviršių. Tuomet atliekamas pluošto skenavimas XY plokštumoje spiralės algoritmu kartu keičiant ir pluošto židinio poziciją Z ašyje. Kiekvienai papliupų energijos bei

impulso trukmės kombinacijai, buvo ieškomi optimalūs atstumai tarp šuvii XY plokštumoje ir pluošto pozicijos pokyčiai Z ašyje, norint pasiekti didžiausią pjovimo greitį.

Tyrimas parodė, jog didesnis pjovimo greitis pasiekiamas su aukštesne papliupų energija. Didėjant papliupų energijai, optimalūs atstumai tarp šuvii ir impulsų trukmės taip pat didėja. Papliupų režimas leido pasiekti 4.2 mm/s pjovimo greitį 4.8 mm storio soda-lime stikle. Taip pat pademonstruoti 1 – 18.8 mm storio, sudėtingų kontūrų (pav. 1) ir iki 35 laipsnių pasvirusių objektų pjovimai.



1 pav. Išpjauto elemento nuotrauka. Elemento diametras 30 mm, storis – 4.8 mm.

Literatūra

1. P. Balage, M. Lafargue, T. Guilberteau, G. Bonamis, C. Hönninger, J. Lopez, and I. Manek-Hönniger, *Micromachines* **14**(9), 1754 (2023).
2. E. Kažukauskas, S. Butkus, P. Tokarski, V. Jukna, M. Barkauskas, and V. Sirutkaitis, *Micromachines* **11**(12), 1093 (2020).
3. A. Žemaitis, M. Gaidys, P. Gečys, M. Barkauskas, and M. Gedvilas, *Opt. Express* **29**(5), 7641 (2021).
4. B. Neuenschwander, B. Jaeggi, D. J. Foerster, T. Kramer, and S. Remund, *J. Laser Appl.* **31**(2), 022203 (2019).
5. G. Račiukaitis, M. Brikas, P. Gečys, B. Voisiat, and M. Gedvilas, *J. Laser Micro/Nanoengineering* **4**(3), 186–191 (2009).

LYDYTO KVARCO ABLIACIJOS EFEKTYVUMO DIDINIMAS NAUDOJANT PAPLIUPŪ REŽIMĄ

Laimis Zubauskas, Edgaras Markauskas, Paulius Gečys

Fizinių ir technologijos mokslų centras, Lazerinių technologijų skyrius
Savonorių pr. 231, LT-02300, Vilnius, el. p.: laimis.zubauskas@ftmc.lt

Šiuolaikiniai ultratrumpų impulsų lazeriai yra perspektyvus įrankis sparčiam stiklų apdirbimui išlaikant aukštą gaminio kokybę. Perspektyviausios lazerinės stiklų apdirbimo technologijos yra tradicinė tiesioginė abliacija (nuo viršaus į apačią) bei apdirbimas nuo apatinės pusės (nuo apačios į viršų). Šios technologijos turi savų privalumų ir trūkumų.

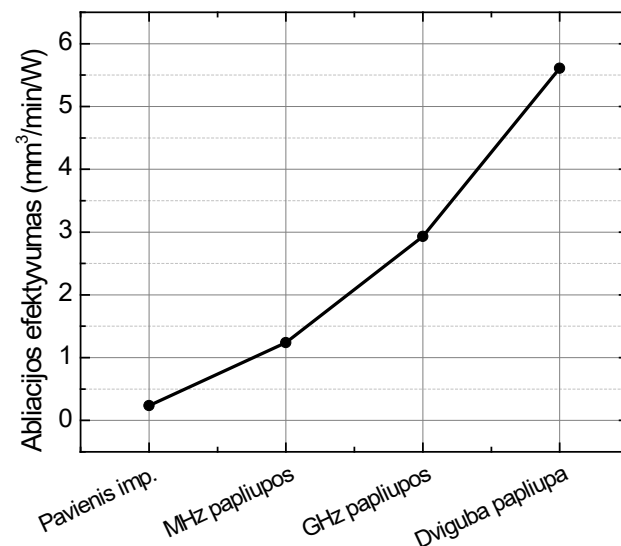
Stiklų apdirbimas nuo apatinės pusės pasižymi didele proceso sparta, nes išvengiama lazerinės spinduliuotės ekranavimo plazma ar sugeneruotas abliacijos produktas. Taip pat, lazerio energija yra panaudojama ne garinimui o trūkių generavimui stikle ir medžiagos pašalinimui didesnėmis dalelėmis [1]. Visa tai lemia, kad ši technologija leidžia formuoti vertikalias pjūvio sienelės, o proceso efektyvumas siekia $7.8 \text{ mm}^3/\text{min}/\text{W}$ [2], tai yra apie 10 kartų efektyviau nei naudojant tiesioginę abliaciją. Kita vertus, gaunami didesni stiklo apskeldėjimai, didesnis abliuotos vienos šiurkštumas, o pati technologija netinka lazerinę spinduliuotę sugeriantiems stiklams pjauti bei 3D abliacijai, kai stiklą reikia apdirbti iš abiejų pusų.

Priešingai, tiesioginė abliacija yra universalesnė technologija leidžianti apdirbti įvairias medžiagas išlaikant aukštą abliacijos kokybę. Tačiau, pjūvio sienelės nėra vertikalios – kanalo profilis atitinka „V“ formą. Taip pat, technologija pasižymi lėta apdirbimo sparta.

Naujausi tyrimai parodė, kad tiesioginės abliacijos sparta bei efektyvumas gali būti padidinti naudojant GHz papliupų režimą [3]. Buvo pademonstruota, kad silikono abliaciją dar labiau pavyko paspartinti naudojant GHz papliupas MHz papliupose (naudojant dvigubų papliupų režimą) [4]. Tačiau dar yra mažai tyrimų, kur šiais papliupų režimais būtų abliuotas stiklas. Tuo labiau, dar nėra aišku, kas lemia spartesnę ir efektyvesnę stiklų abliaciją.

Todėl eksperimentų metu buvo abliuojami $2 \times 2 \text{ mm}^2$ dydžio ploteliai lydytame kvarce naudojant įvairius papliupų režimus. Tam buvo pasitelktas femtosekundinis lazeris generuojantis 176 fs trukmės ir 1030 nm bangos ilgio impulsus. Po abliacijos buvo matuojami gautų plotelių gyliai,

paviršių šiurkštumai S_a , sienelių polinkio kampai, apskeldėjimas. Atsižvelgiant į išmatuotus parametrus buvo įvertinami proceso sparta ir efektyvumas. Efektyvumo priklausomybė nuo naudojamo režimo yra pavaizduota 1 paveiksle. Gauti duomenys parodė, kad papliupų režimas leido pakeisti stiklo pašalinimo mechanizmą iš stiklo garinimo į skaldymą. Procesas tapo panašus į apdirbimą nuo apatinės stiklo pusės. Papildomai, buvo pastebėta, kad spartos bei efektyvumo padidėjimui įtakos turėjo lazerinės spinduliuotės savifokusaciją stikle.



Pav. 1. Ablaciros efektyvumo priklausomybė nuo naudojamo impulsų generavimo režimo.

Literatūra

1. P. Gečys, J. Dudutis, and G. Račiukaitis, Journal of Laser Micro Nanoengineering, 10(3), 254-258 (2015).
2. V. Tomkus, V. Girdauskas, J. Dudutis, P. Gečys, V. Stankevič, and G. Račiukaitis, Optics Express, 26(21), 27965-27977 (2018).
3. S. Schwarz, S. Rung, C. Esen, and R. Hellmann, Optics Letters, 46(2) (2021).
4. K. Obata, F. Caballero-Lucas, S. Kawabata, G. Miyaji, and K. Sugioka, Int. J. Extrem. Manuf., 5, 025002 (2023).

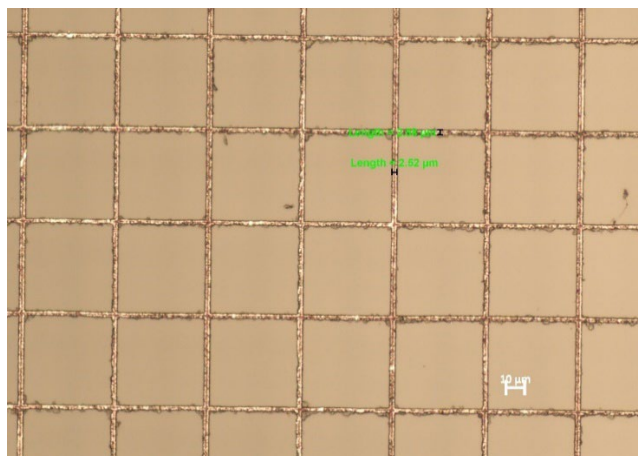
LAZERIU ASISTUOTAS VARIO MIKROTAKELIU NUSODINIMAS ANT DIELEKTRIKO PAVIRŠIAUS

Modestas Sadauskas¹, Karolis Ratautas¹, Evaldas Kvietkauskas¹,
Viktorija Vrubliauskaitė¹, Gediminas Račiukaitis¹

Fizinių ir technologijos mokslų centras, ¹Lazerinių technologijų skyrius, ²Katalizés skyrius
Savanorių pr. 231, LT-02300 Vilnius, el. p.: modestas.sadauskas@ftmc.lt

Elektronikos pramonė nuolat ieško būdų, kaip sukurti mažesnius ir funkcionalesnius įrenginius. Vario mikrotakeliai galėtų būti naudojami kaip vieni iš pagrindinių sudedamųjų dalių skaidriems elektrodamams, šildymo plėvelėms ar įvairiems jutikliams (Pav. 1). Mikronų dydžio elektrinės grandinės suformuotos ant stiklo paviršiaus yra esminė dalis pažangiam elektronikos pakavimui/ sluoksniavimui ir integravimui. Mikronų ar net submikronų dydžio takeliai suformuoti ant stiklo paviršiaus galėtų padaryti proveržį pakavimo technologijose.

Viena iš perspektyvių technologijų, galinčių prisdėti prie šio tiksloto, yra selektivus paviršiaus aktyvavimas lazerine spinduliuote arba SSAIL (*Selective Surface Activation Induced by Laser*) [1]. Šis procesas leidžia ant įvairių dielektrinių paviršių, pavyzdžiui stiklo ar plastiko, formuoti elektrai laidžius takelius. SSAIL procesą sudaro trys pagrindiniai etapai: lazerinis paviršiaus modifikavimas impulsinio lazerio spinduliuote, aktyvavimas specialiu tirpalu ir besrovis cheminis vario nusodinimas. Šio proceso efektyvumas labai priklauso nuo lazerinių parametruų paviršiaus apdirbimo metu: impulsų pasikartojimo dažnis, impulsų trukmė, impulsų persiklojimo skenuojant pluoštą, impulsų energijos, pluošto dydžio ar jo poliarizacijos ant paviršiaus.

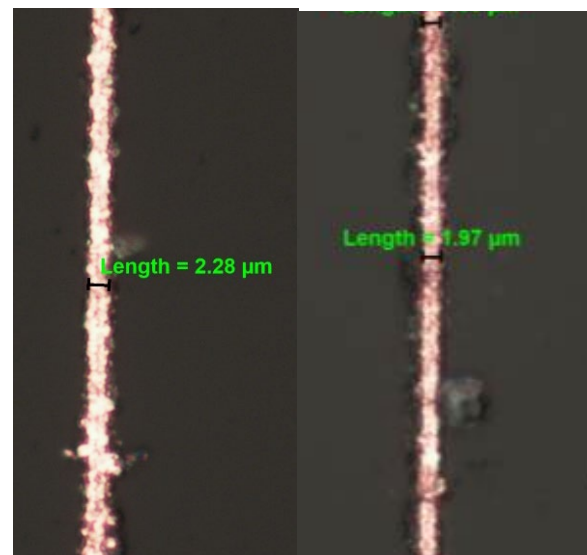


Pav. 1. Metalinis tinkliukas ant silikatinio stiklo suformuotas naudojant SSAIL technologiją.

Tokių struktūrų formavimui ant silikatinio stiklo bei plonos, lanksčios polietileno tereftalato (PET) plėvelės buvo naudojamas šviesos konversijos Pharos lazeris su 320 fs impulsu trukme, bei 515 nm spinduliuotės bangos ilgiu. Lazerio pluoštas

buvo fokusuojamas mirkoskopiniu objektyvu į maždaug 4 mm dydžio démę. Pluošto skenavimui buvo judinami XY stalai ant kurių buvo pritvirtinti dielektriko bandiniai. Skaidraus dielektriko paviršius buvo modifikuojamas naudojant skirtinges impulsų energijas, impulsų pasikartojimo dažnį, impulsų persiklojimą, impulsų trukmę ar poliarizaciją norint išvertinti kaip priklauso suformuotos ir metalizuotos linijos plotis nuo šių lazerinių parametrų. Paviršiaus modifikavimui taip pat buvo naudotas ir eksikonas, kurio buvo formuojamas Beselio pluoštas norint sumažinti suformuotos linijos pločio priklausomybę nuo pluošto išfokusavimo pakitus atstumui tarp apdirbamo paviršiaus ir fokusuojančio elemento.

Eksperimentiškai pademonstruota, jog naudojant SSAIL technologiją, ant skaidraus dielektriko galima suformuoti kelių mikrometrų pločio elektrai laidžias struktūras - Pav. 2.



Pav. 2 Metalizuoti takeliai ant silikatinio stiklo bei PET plastiko suformuoti naudojant SSAIL technologiją.

Literatūra:

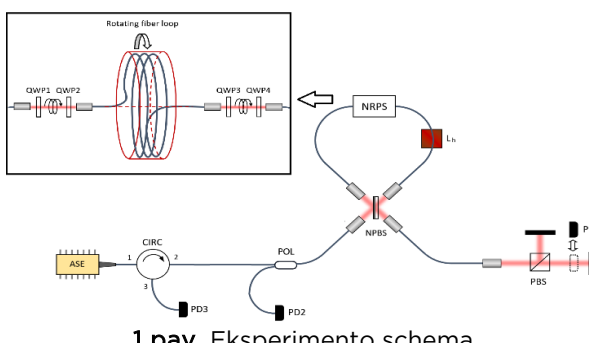
1. K. Ratautas, A. Jagminienė, I. Stankevičienė, M. Sadauskas, E. Norkus, and G. Račiukaitis, Evaluation and optimisation of the SSAIL method for laser-assisted selective electroless copper deposition on dielectrics, *Results Phys.*, vol. 16, p. 102943, (2020).

SANJAKO EFEKTU PAGRĮSTAS OPTINIS IZOLIATORIUS SKIRTAS PLATAUS SPEKTO ŠVIESAI

Jaroslav Kodz, Kęstutis Regelskis, Nikolajus Gavrilinas, Julijanas Želudevičius

Fizinių ir technologijos mokslų centras, lazerinių technologijų skyrius
Savanorių pr. 231, 02300 Vilnius, el. p.: jaroslav.kodz@ftmc.lt

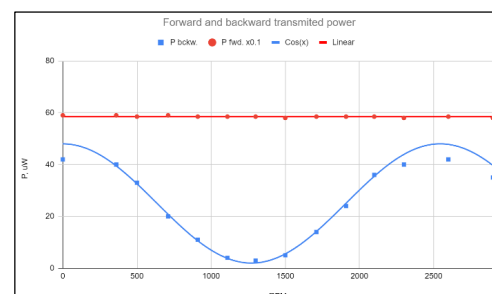
Dauguma šiandien naudojamų optinių izoliatoriu bei cirkulatorių veikia dėl magneto-optinio Faradéjaus efekto. Tačiau egzistuoja ir kiti fiziniai efektai, kuriuos panaudojant galima užtikrinti neapgręžiamą šviesos perdavimą. Ankstesniame darbe mūsų grupė pademonstravo keturių kanalų cirkulatorių, kurio veikimas yra pagristas Sanjako efektu [1]. Sanjako efektas yra patrauklus tuo, jog nėra susijęs su konkrečiu optiniu medžiagų panaudojim, o atsiranda dėl paties erdvėlaikio savybių. Taigi jis yra fundamentaliai universalus ir pasiūlytas optinio izoliatoriaus principas gali būti pritaikomas visam elektromagnetinės spinduliuotės diapazonui, nuo radio bangų iki rentgeno. Žiūrint dar plačiau, Sanjako efektas pasireiškia su bet kokiomis de Broglie bangomis, pvz. elektronais, o taipogi akustinėmis ar net gravitacinėmis bangomis. Taigi teoriškai pasiūlyto prietaiso pritaikymo galimybės yra labai plačios. Ankstesniuose tyrimuose Sanjako interferometras buvo sukonstruotas panaudojant polarizacini pluošto dalikli. Tokia schema gerai veikia su siauro spekto spinduliuotę. Vis dėl to nepavyko pademonstruoti prietaiso veikimo su plataus spekto nekoherentine šviesa. Šiame darbe buvo sukonstruota ir ištirinėta optinio izoliatoriaus pagristo Sanjako efektu schema su nepolarizuojančiu pluoštu dalikli (1 pav.).



1 pav. Eksperimento schema.

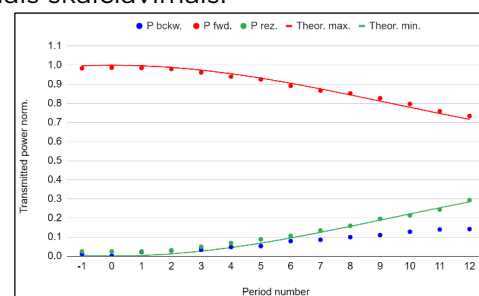
Kaip šviesos šaltinis buvo panaudotas sustiprintos spontaninės emisijos diodas. Sanjako interferometras buvo sudarytas iš nepolarizuojančio pluošto daliklio, keturių kolimatorių bei polarizaciją išlaikančio šviesolaidžio (Fujikura PM980, Panda tipo), kurio bendras ilgis - apie 4 metrai. Šviesolaidis buvo suvyniotas į ritę ir prityirtintas prie besisukančio aliumininio disko. Dvi ketvirčio bangos ilgio plokštelii poros buvo naudojamos tam, kad perduoti tiesinės polarizacijos šviesą tarp stacionarios ir besisukančios schemas dalių. Pro interferometrą praėjusi šviesa buvo praleidžiam pro polarizacinių kubų PBS ir atspindimą atgal į

interferometrą veidrodžio M pagalba. Priklausomai nuo polarizacijos atgal grįžtantį šviesa buvo nukreipama arba į detektorių PD1, arba į detektorių PD2. Eksperimento metu disko greitis buvo keičiamas įnešant fazės skirtumą dėl Sanjako efekto. Papildomai šviesolaidžio L_h atkarpa buvo šildoma, kas įnešdavo papildomą fazės poslinkį dėl skaidulos lėtosios ir greitosios polarizacinių ašių lūžio rodiklių skirtumo. Keičiant kaitintuvu temperatūrą prie skirtingu greičių buvo parenkamos sąlygos, kad tiesioginė kryptimi praėjusios šviesos polarizacija būtų visada vienoda, o pralaidumas pro polarizacinių kubų maksimalus. Šviesos pralaidumas pro interferometrą tiesioginę ir atgalinę kryptimis yra pavaizduotas 2 pav. Maksimalus pralaidumo skirtumas atgalinę kryptimi siekia 15 kartų.



2 pav. Išmatuota šviesos praėjusios pro interferometrą galios priklausomybė nuo disko sukimosi greičio (aps./min.).

Taipogi buvo ištirta priklausomybė nuo interferometro optinių kelių ilgių skirtumo (3 pav.). Didėjant interferometro šakų ilgio skirtumui suprastėja pluoščių interferencija, dėl ko šviesos izoliacija irgi pablogėja, kas gerai sutampa su teoriniaisiai skaičiavimais.



3 pav. Koherentiškumo ilgis.

Reikšminiai žodžiai: neapgręžiamas fazės poslinkis, Sanjako efektas, optinis izoliatorius.

Literatūra:

[1] K. Regelskis, J. Kodz, N. Gavrilinas, J. Želudevičius, Polarization-dependent four-port fiber optical circulator based on Sagnac effect, Optics Express 31(3), January 2023.

REACTIVE MAGNETRON SPUTTERING OF $\text{Sr}_2\text{FeMoO}_6$ FILM

Ignas Bitinaitis¹, Alexandr Belosludtsev¹, Gunnar Suchaneck²,
Christian Andreas Ullmann², Nikolai Sobolev³

¹Center for Physical Sciences and Technology, Department of Laser Technology
Saulėtekio al. 3, LT-10257 Vilnius, email: ignas.bitinaitis@ftmc.lt

²Technische Universität Dresden, Institut für Festkörperferelektronik, 01062, Dresden, Germany

³Universidade de AveiroCampus, Universitário de Santiago, 3810-193, Aveiro, Portugal

$\text{Sr}_2\text{FeMoO}_6$ (SFMO) due to its high degree of spin polarisation and high Curie temperature is promising material layer for room temperature spintronic and plasmonic devices. Variations in SFMO lattice and material composition greatly impacts its magnetic properties and application range of spintronic device. High-quality SFMO film is difficult to obtain due to unavoidable defects and nonstoichiometry related to oxides.

Using multitarget reactive magnetron sputtering technology it is possible to achieve high density and precise composition depositions of SFMO layers. Deposition parameters such as oxygen pressure, deposition rate, and target temperature can be varied to achieve optimal film composition and reduce amount of defects.

Aim of this work is to reach optimum SFMO film composition using reactive magnetron sputtering for further development of multilayered magnetic film structure for spintronic devices.

Film was deposited using industrial sputtering system (LS730S, VON ARDENNE, Dresden, Germany) on 150 mm diameter platinised silicon wafer using high-purity Sr, Fe and Mo targets. For precise control of partial oxygen pressure, plasma emission monitor (PEM) was used. Deposition parameters were adjusted and fine-tuned after each deposited SFMO film investigation. Deposited films were investigated using Scanning Electron Microscope (SEM), Energy Dispersive X-Ray Spectroscopy (EDX), Scanning Electron Microscopy (SEM), X-ray Diffraction (XRD), Atomic Force Microscope (AFM) and sample reflectance in UV-IR range.

Deposited SFMO film thickness was measured to be close to 440 nm, depending on adjusted target deposition power. Achieved SFMO film composition was close to optimal composition and samples were provided for further multilayered structure deposition to prototype and develop spintronic sensor.

Keywords: SFMO, Reactive magnetron sputtering.

Acknowledgment. The authors acknowledge the support of the work in frames of the European project H2020-MSCA-RISE-2017 - SPINMULTIFILM.

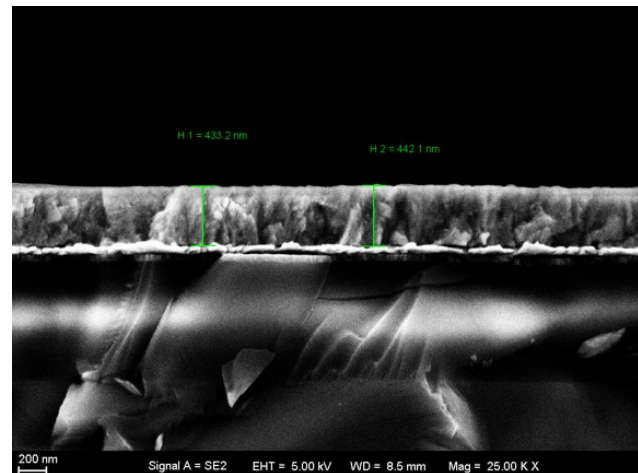


Fig. 1. Scanning Electron Microscope (SEM) image of deposited SFMO film, side view.

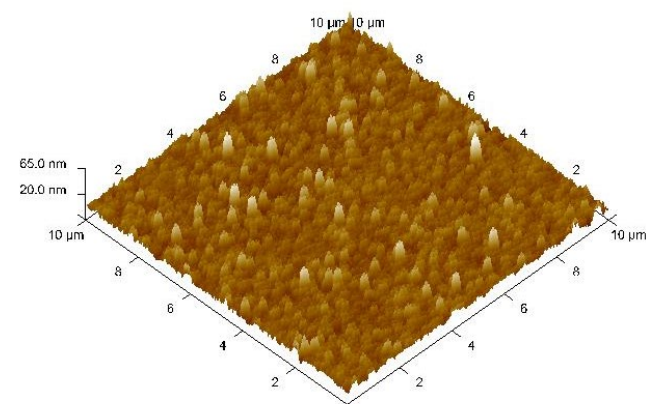


Fig. 2. Atomic Force Microscope (AFM) 3D topography of deposited SFMO film.

References

1. Gunnar Suchaneck, Evgenii Artiukh, Gerald Gerlach, Resistivity and Tunnel Magnetoresistance in Double-Perovskite Strontium Ferromolybdate Ceramics, physica status solidi (b), 10.1002/pssb. 202200012, 259, 8, (2022).
2. Andrulevičius, M.; Artiukh, E.; Suchaneck, G.; Wang, S.; Sobolev, N.A.; Gerlach, G.; Tamulevičienė, A.; Abakevičienė, B.; Tamulevičius, S. Multitarget Reactive Magnetron Sputtering towards the Production of Strontium Molybdate Thin Films. Materials 2023, 16, 2175. <https://doi.org/10.3390/ma16062175>

THE ROLE OF CELL WALL IN ORGANIC-SOLVENT LIPID EXTRACTION FROM OLEAGINOUS YEASTS ASSISTED BY PULSED ELECTRIC FIELDS

Greta Tartėnė¹, Carlota Delso Muniesa², Wolfgang Frey², Arūnas Stirkė¹

¹Center for Physical Sciences and Technology, Department of Functional Materials and Electronics
Saulėtekio av. 3, LT-10257 Vilnius, email: greta.tartene@ftmc.lt

²Institute for Pulsed Power and Microwave Technology, Karlsruhe Institute of Technology,
76344 Eggenstein-Leopoldshafen, Karlsruhe, Germany

Population growth and the resulting demand for energy and resources pose significant economic and societal challenges. As the need for plant-based oils increases, yet the available land shrinks, a search for alternatives has never been more dire.

Microbial oils, or single-cell oils (SCO), produced by microorganisms such as yeast, microalgae, fungi, and bacteria, present some of the most viable alternatives. SCOs can replace plant-based oils in various applications, including biofuels, food additives, cosmetics, and oleochemicals [1].

Among these microorganisms, yeasts are particularly noteworthy for their ability to accumulate over 70% of their dry cell weight in lipids. One of the novel techniques for optimization of lipid extraction from yeast is pulsed electric field (PEF) treatment. This method involves applying short, intense electric pulses, which enhances plasma membrane permeability. This effect is called electroporation or electropermeabilisation [2].

Experiments on *Saitozyma podzolica* yeasts have shown that PEF treatment can achieve lipid extraction yields of up to 97% after solvent extraction, a substantial improvement compared to just 10% without pre-treatment [3].

Apart from plasma membrane, which is a target organelle for lipid extraction, yeast cells are surrounded by a rigid outer cell wall. It provides structural integrity and protects against external stressors, one of them being changes in osmotic pressure. In our earlier works we have shown that PEF increases the permeability of cell wall alongside plasma membrane [3].

Furthermore, osmotic changes in electroporated yeasts environment greatly influence their survival.

In this work we show that combining PEF treatment with a subsequent 24-hour incubation period in various osmotic environments significantly affects lipid extraction yield. Specifically, hypoosmotic environment enhances lipid extraction. In the hypoosmotic environment yeast cells likely shed or thin their cell walls, thereby facilitating enhanced extraction. Conversely, the yield is significantly lower in hyperosmotic environment however the mechanism for this effect is not yet known.

In the future, we will directly investigate the mechanisms behind the changes in lipid extraction yields in combination with PEF treatment.

References

1. Carlota Delso, Aude Silve, Rüdiger Wüstner, Natalja Nazarova, Ignacio Álvarez, Javier Raso, and Wolfgang Frey, Post-incubation pH Impacts the Lipid Extraction Assisted by Pulsed Electric Fields from Wet Biomass of Auxenochlorella protothecoides, ACS Sustainable Chemistry & Engineering 2022 10 (37), 12448-12456.
2. Stirke A, Celiesiute-Germaniene R, Zimkus A, Zurauskienė N, Simonis P, Dervinis A, Ramanavicius A, Balevicius S. The link between yeast cell wall porosity and plasma membrane permeability after PEF treatment. Sci Rep. 2019 Oct 14;9(1):14731.
3. Gorte O, Nazarova N, Papachristou I, Wüstner R, Leber K, Syldatk C, Ochsenreither K, Frey W, Silve A. Pulsed Electric Field Treatment Promotes Lipid Extraction on Fresh Oleaginous Yeast *Saitozyma podzolica* DSM 27192. Front Bioeng Biotechnol. 2020 Sep 11;8:575379.

MFC EFFICIENCY WITH *E. meliloti* AND REDOX MEDIATORS

Tomas Mockaitis¹, Inga Morkvėnaitė-Vilkončienė¹

¹Center for Physical Sciences and Technology, Department of Nanotechnology
Saulėtekio av. 3, LT-10257 Vilnius, Lithuania email: tomas.mockaitis@ftmc.lt

Microbial fuel cells (MFCs) have received significant attention as a sustainable energy solution addressing both environmental and energy challenges. These bioelectrochemical systems generate electricity by utilizing electrical charges produced during the anaerobic oxidation of organic matter, such as environmental waste and renewable biomass [1]. MFCs use electrochemically active microorganisms to oxidize organic substances and convert them into electrical energy [2]. Additionally, certain organic pollutants can act as electron donors or acceptors, allowing for their removal through microbial oxidation at the MFC anode or electron acceptance at the cathode. Oxygen is commonly used as an electron acceptor due to its high oxidation potential and abundance, though recent studies have focused on exploring alternative electron acceptors to improve the efficiency of MFC reactions [3]. With promising ecological benefits and the potential for clean energy generation, MFCs are emerging as an attractive technology for sustainable waste management and renewable energy production.

The symbiotic relationship between *Ensifer meliloti* bacteria and legume plants plays a crucial role in nitrogen fixation, initiated when plants release betaines and flavonoids to attract the bacteria to their root hairs. The bacteria secrete nod factors, leading to the formation of infection threads and the development of bacteroids in root nodules. *E. meliloti* can fix nitrogen only as an endosymbiotic bacteroid, while leghemoglobin regulates oxygen levels to ensure the functionality of the nitrogenase enzyme [4].

This research aims to investigate the application of *E. meliloti* in MFCs and explore the charge transfer mechanisms between bacteria and electrodes, enhanced by two redox mediators—potassium ferricyanide and various types of quinone mediators

References:

1. Reinikovaite, V.; Zukauskas, S.; Zalneravicius, R.; Ratautaite, V.; Ramanavicius, S.; Bucinskas, V.; Vilkiene, M.; Ramanavicius, A.; Samukaite-Bubniene, U. Assessment of Rhizobium anhuiense Bacteria as a Potential Biocatalyst for Microbial Biofuel Cell Design. *Biosensors* 2023, 13, 66. <https://doi.org/10.3390/bios13010066>.
2. Rozene, J.; Morkvenaite-Vilkonciene, I.; Bruzaite, I.; Dzedzickis, A.; Ramanavicius, A. Yeast-based microbial biofuel cell mediated by 9,10-phenanthrenequinone. *Electrochim Acta* 2021, 373, doi: 10.1016/j.electacta.2021.137918
3. Ramanavicius, S.; Ramanavicius, A. Charge Transfer and Biocompatibility Aspects in Conducting Polymer-Based Enzymatic Biosensors and Biofuel Cells. *Nanomaterials* 2021, 11, 1–22. <https://doi.org/10.3390/nano11020371>.
4. Nyangau EO, Abe H, Nakayasu Y, Umetsu M, Watanabe M, Tada C. Iron azaphthalocyanine electrocatalysts for enhancing oxygen reduction reactions under neutral conditions and power density in microbial fuel cells. *Bioresour Technol Rep* 2023, <https://doi.org/10.1016/j.biteb.2023.101565>

SENSING MECHANICAL PROPERTIES BY AFM: COMPARATIVE ANALYSIS OF POLYMER SAMPLES

Laisvidas Striška¹, Inga Morkvėnaitė-Vilkončienė¹

¹Center for Physical Sciences and Technology, Department of Nanotechnology
Saulėtekio av. 3, LT-10257 Vilnius, Lithuania email: laisvidas.striska@ftmc.lt

Atomic force microscopy (AFM) is a powerful tool for measuring the mechanics of soft materials [1]. Mechanical properties are expressed as Young's modulus, obtained by fitting the contact mechanics model to force-indentation dependencies. For soft surfaces, like polymers and biological materials, the dependency of cantilever displacement vs. deflection is nonlinear when the tip is in contact with the sample. Because of that cantilever force and indentation become inaccurate, and models applied to determine Young's modulus cannot extract useful information. Also, the contact area increases with indentation. Therefore, it is unclear what part of the results depends on the geometry of the tip and what part on sample properties. Also, most models are designed with assumptions that the sample is homogeneous, isotropic, linear elastic half-space experiencing infinitesimally small strains. In contrast, biological (and soft) materials can demonstrate opposite behavior, such as inhomogeneity, anisotropy, and nonlinearity [2]. Moreover, the indentation size is several hundreds of nanometers, while the thickness of the sample is several micrometers and cannot be determined as infinitesimal [3]. The experimental problem is that sharp tips lead

to local strains that exceed the linear material regime [4].

The comparison of AFM measurement results with macroscopic techniques results could be a reliable way to find appropriate experimental conditions and mathematical processing of data.

References:

1. Galluzzi, M.; Biswas, C.S.; Wu, Y.; Wang, Q.; Du, B.; Stadler, F.J. Space-Resolved Quantitative Mechanical Measurements of Soft and Supersoft Materials by Atomic Force Microscopy. *NPG Asia Mater.* **2016**, *8*, doi:10.1038/am.2016.170.
2. Costa, K.D.; Yin, F.C.P.P. Analysis of Indentation: Implications for Measuring Mechanical Properties with Atomic Force Microscopy. *J. Biomech. Eng.* **1999**, *121*, 462–471, doi:10.1115/1.2835074.
3. Dzedzickis, A.; Rožėnė, J.; Bučinskas, V.; Viržonis, D.; Morkvėnaitė-Vilkončienė, I. Characteristics and Functionality of Cantilevers and Scanners in Atomic Force Microscopy. *Materials (Basel)*. **2023**, *16*, 6379, doi:10.3390/ma16196379.
4. Dimitriadis, E.K.; Horkay, F.; Maresca, J.; Kachar, B.; Chadwick, R.S. Determination of Elastic Moduli of Thin Layers of Soft Material Using the Atomic Force Microscope. *Biophys. J.* **2002**, *82*, 2798–2810, doi:10.1016/S0006-3495(02)75620-8.

ATOMINIŲ JĘGŲ MIKROSKOPIJOS METODIKOS LÄSTELIŲ STRUKTŪRINIAMS IR Viskoelastinių savybių tyrimams bioimitaciniše aplinkose

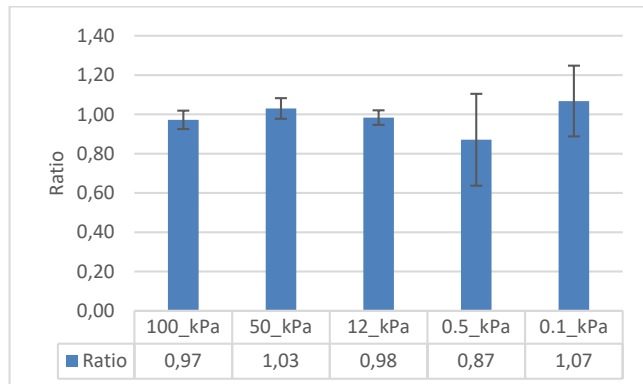
Tadas Jelinskas, Artūras Ulčinas

Fizinių ir technologijos mokslų centras, Naoinžinerijos skyrius
Savanorių pr. 231, LT-02300 Vilnius, el. p.: tadas.jelinskas@ftmc.lt

Lästelių mechanobiologija yra tarpdisciplininė mokslo sritis, kuri orientuojaasi į tyrimus skirtus suprasti, kaip mechaninės jėgos veikia lästelių elgseną, struktūrą ir funkcijas. Lästelės aplinkos mechaninės savybės, pavyzdžiuui, paviršiaus standumas gali paskatinti kamieninių lästelių diferenciaciją į chondrocytus arba osteoblastus [1], kita vertus pačių chondrocytu viskoelastinių savybių silpnėjimas matomas artrito pažeistoje kremzlėje ir senėjimo metu [2].

Su vis didėjančiais lūkesčiais tyrinėti kosmosą ir pasiekti gretimas saulės sistemos planetas yra svarbu suprasti tokį ekspedicijų rizikas. Vienas iš labiausiai jaučiamų efektų ekspedicijų metu yra mikrogravitacija (nesvarumas), dėl kurios dingsta apkrova kūnui. Sumažėjus mechaninei apkrovai prasideda kaulų demineralizacija, atsiranda kremzlės pažeidimai, raumenų atrofija, ir t.t [3] [4]. Tam, kad ateityje būtų galima išvengti rimtų sveikatos sutrikimų ilgose kosmoso ekspedicijose svarbu suprasti, koks yra mikrogravitacijos poveikio audiniams mechanizmas.

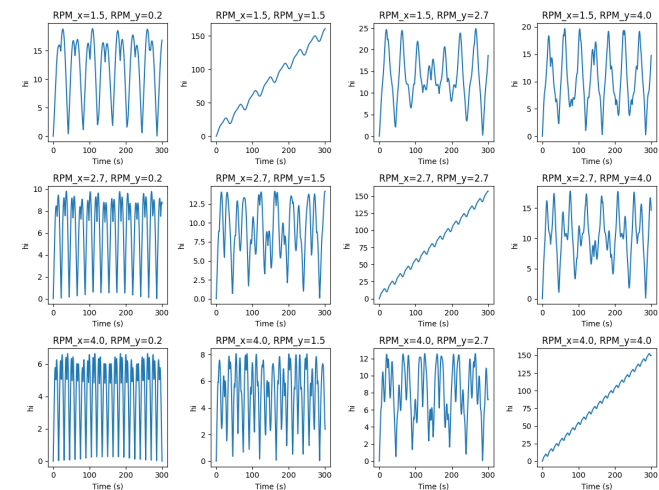
Atominės jėgos mikroskopas (AJM) yra vienas iš pagrindinių įrankių naudojamų mechaninių savybių matavimams, gali išmatuoti įvairius medžiagų ar lästelių mechaninius parametrus mikro ir nanoskalėje. Šios doktorantūros metu, bendradarbiaujant su Europos kosmoso agentūra, bus atliekami tyrimai susiję su chondrocytų ir kremzlės modelio mechaninių savybių analize simuliuotos mikrogravitacijos sąlygomis. Kadangi sąnario kremzlės struktūra, mechaniniu požiūriu, yra gan sudėtinga, jos standumas makro skalėje gali variuoti tarp 0,1-2MPa, mikro skalėje 40 - 70 kPa [5], o pačių chondrocytų standumas siekia vos kelis kPa. Norint tiksliai įvertinti kremzlės mikromechaninius parametrus pirmiausia buvo atlikti AJM matavimo protokolo optimizavimo darbai naudojant 0,1-100 kPa PAAm hidrogelių etaloninius bandinius (pav. 1).



Pav. 1. Išmatuoto ir deklamuojamo Jungo modulio santykis.

Mikrogravitacijai simuliuoti Nanoinžinerijos skyriuje buvo sukonstruotas 3D klinostatas. Šio prietaiso veikimas pagrįstas tuo jog dvi sukimo ašys atskirais žingsniais varikliais nuolatos keičia bandinio orientaciją 3D erdvėje. Prietaisas kontroliuojamas

Arduino Nano plokštė, bei specialiai parašyta programa. Klinostato sukimosi ciklas buvo charakterizuotas atlikus kompiuterinės simuliacijas ir apskaičiavus sukamo bandinio orientacijos kryptingumą.



Pav. 2. Bandinio orientacijos kryptingumas priklausomai nuo ašių sukimosi greičio simuliacijos metu. Kuo didesnė kreivės vertė tuo ilgiau išlaikoma orientacija tam tikra kryptimi.

Šiuo metu atlikti mechaninės analizės ir mikrogravitacijos simuliavimo darbai yra pagrindas tolimesniems tyrimams. Suformuotas mikromechanikos matavimo protokolas išbandytas su žinomo standumo standartais. Išmatuotos Jungo modulio vertės yra labai artimos dekrlaruotoms. Klinostato sukimosi ciklo modeliavimas parodė jog teoriškai geriausia ašių sukimosi greičio kombinacija yra 4 : 0.2 RPM.

Literatūra

- [1] R. O. Navarrete et al., 'Substrate stiffness controls osteoblastic and chondrocytic differentiation of mesenchymal stem cells without exogenous stimuli', PLoS One, vol. 12, no. 1, Jan. 2017, doi: 10.1371/journal.pone.0170312.
- [2] Q. Zhang, M. Zhang, N. Meng, X. Wei, and W. Chen, 'Mechanobiology of the articular chondrocyte', in Bone Cell Biomechanics, Mechanobiology and Bone Diseases, Elsevier, 2023, pp. 249-287. doi: 10.1016/B978-0-323-96123-3.00016-6.
- [3] B. Ganse, M. Cucchiari, and H. Madry, 'Joint Cartilage in Long-Duration Spaceflight', Jun. 01, 2022, MDPI. doi: 10.3390/biomedicines 10061356.
- [4] J. B. West, 'Physiology in microgravity.', J Appl Physiol (1985), vol. 89, no. 1, pp. 379-84, Jul. 2000, doi: 10.1152/jappl.2000.89.1.379.
- [5] W. Xu, J. Zhu, J. Hu, and L. Xiao, 'Engineering the biomechanical microenvironment of chondrocytes towards articular cartilage tissue engineering', Nov. 15, 2022, Elsevier Inc. doi: 10.1016/j.lfs.2022.121043.

APLINKAI JAUTRIJU FLUORESCUOJANČIU BODIPY JUTIKLIU KŪRIMAS LIGŲ DETEKCIJAI

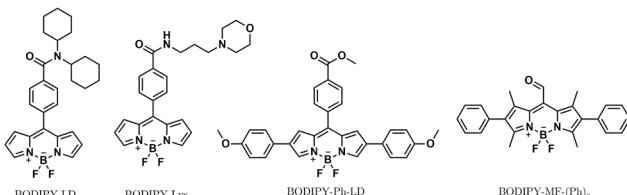
Artūras Polita^{1,2}, Rūta Bagdonaitė², Gintaras Valinčius²

¹ Fizinių ir technologijos mokslų centras, Organinės chemijos skyrius
Saulėtekio al. 3, LT-10257 Vilnius, el. p.: arturas.polita@ftmc.lt

² Vilniaus Universitetas, Gyvybės mokslų centras, Bioelektrochemijos ir biospektroskopijos skyrius
Saulėtekio al. 7, LT-10257 Vilnius

Mikroklampos, poliškumo bei balytmų koncentracijos vaizdinimas lipidinėse sistemose gali atskleisti ne tik reikšmingą informaciją apie ląstelės būseną, bet ir leisti identifikuoti ligas, kurių metu kinta ląstelių signaliniai kelai, metabolizmas bei balytmų raiška [1]. Vėžinių ligų atveju besikaupiantčios mutacijos bei padidėjęs metabolinis aktyvumas lemia lipidinių membranų kompozicinius pokyčius bei lipidų oksidaciją [1], suteikiančią galimybę detektuoti vėžinius susirgimus per lipidinių sistemų biofizikinių savybių vaizdinimą.

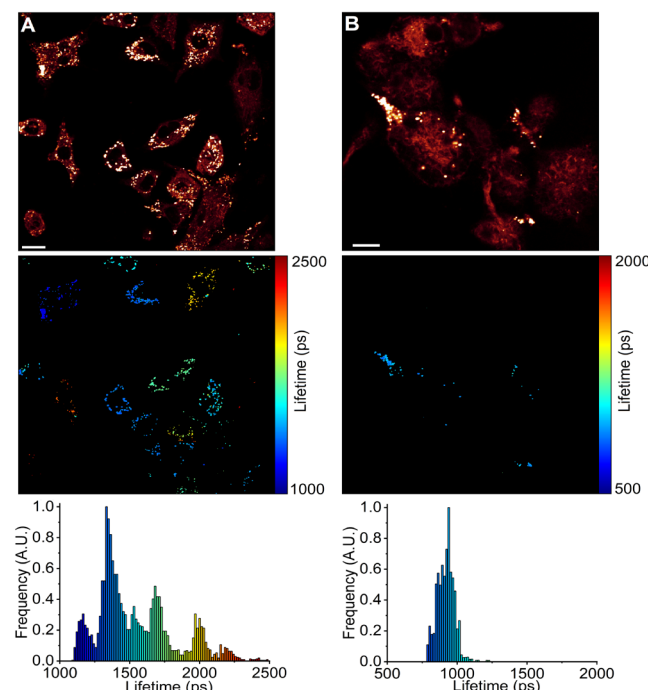
Aplinkai jautrūs organiniai fluoroforai suteikia vieną iš paprasčiausių būdų vaizdinti biofizikinių parametru pokyčius gyvose sistemose dėl efektyvaus šių fluoroforų prasiskverbimo per ląstelių membranas, mažo toksiškumo bei lengvai modifikuojamų junginių savybių [2]. Pastaraisiais metais ypač didelio pasisekimo susilaukė BODIPY (boro dipirometeno) grupės fluoroforai, kurių veikimas paremtas spindulinės bei nespindulinės relaksacijos konkurencija, kintančią nuo aplinkos savybių bei leidžiančią vaizdinti fluoroforų gyvavimo trukmę pasitelkiant fluorescencijos gyvavimo trukmės vaizdinimo mikroskopiją (angl. *fluorescence lifetime imaging microscopy*, FLIM) [3,4].



1 pav. Tyime naudojami BODIPY fluoroforai. Mikroklampai jautrūs molekuliniai rotoriai BODIPY-LD bei BODIPY-Lys, poliškumui bei balytmų koncentracijai jautrūs jutikliai - BODIPY-Ph-LD bei BODIPY-MF-(Ph)₂.

Šiame darbe, pasitelkiant FLIM'ą, nagrinėjamas mikroklampai, poliškumui bei balytmų koncentracijai jautrių BODIPY fluoroforų kūrimas bei panaudojimas vėžio diagnostikai (pav. 1). Tyime pristatomi ląstelinėms organelėms specifiški mikroklampos jutikliai - BODIPY-Lys bei BODIPY-LD, atskleidžiantys reikšmingus klampos skirtumus tarp sveikų ir vėžinių žmogaus ląstelių lizosomose bei lipidiniuose lašeliuose (pav. 2). Darbe demonstruojama, kaip pasitelkiant mikroklampai jautrius fluoroforus galima atpažinti skirtingomis ląstelinėmis būsenomis pasižymintias vėžines ląsteles bei įvertinti vėžinio audinio atsparumą chemoterapijai. Antroje tyrimo dalyje

aptariama elektronus donoruojančių grupių įtaka BODIPY mikroklampos sensorinėms savybėms bei pristatomui poliškumui bei balytmų koncentracijai jautrūs jutikliai - BODIPY-Ph-LD bei BODIPY-MF-(Ph)₂. Parodoma, elektronus donoruojančių pakaitų prijungimas keičia BODIPY molekulių sensorinės savybes ir leidžia išgauti mikroklampai nejautrius, bet poliškumui jautrius fluoroforus.



2 pav. BODIPY-LD FLIM'as lipidiniuose lašeliuose žmogaus plaučių vėžio A549 (A) ir sveikų inkstų HEK 293T (B) ląstelėse. Viršutinėje panelėje parodytos fluorescencijos intensyvumo nuotraukos, viduryje - BODIPY-LD gyvavimo trukmės, apačioje - gyvavimo trukmės histogramos. Skalės - 10 µm.

Darbas sudarytas iš nuostoviosios bei nuo laiko priklausančio fluorescencijos spektrų, gyvų ląstelių vaizdinimo FLIM'u bei sugerties matavimų.

Literatūra

1. S.Vasseur, and F.Guillaumond, Oncogenesis, 11, 46 (2022).
2. Y.Fu, and N.S.Finney, RSC Adv. 8, 29051-29061 (2018).
3. M.A.Haidekker, and E.A.Theodorakis, Org. Biomol. Chem. 5, 1669-1678 (2007).
4. J.A.Levitt, P.Chung, M.K.Kuimova, G.Yahiroglu, Y.Wang, J.Qu, and K.Suhling, ChemPhysChem 12, 662-672 (2011).

FLUORESCENCE CONCENTRATION QUENCHING IN SOLUTIONS OF ZINC- AND FREE BASE PHTHALOCYANINES

Ivan Halimski¹, Simona Streckaitė¹, Jevgenij Chmeliov^{1,2}, Andrius Gelzinis^{1,2}, Leonas Valkunas¹

¹Fizinių ir technologijos mokslų centras, Molekulinių darinių fizikos skyrius
Saulėtekio al. 3, LT-10257 Vilnius, el. p.: ivan.halimski@ftmc.lt

¹Center for Physical Sciences and Technology, Department of Molecular Compound Physics
Saulėtekio av. 3, LT-10257 Vilnius, email: ivan.halimski@ftmc.lt

²Vilnius University, Faculty of Physics, Institute of Chemical Physics
Saulėtekio av. 9-III, LT-10222 Vilnius

The phenomenon of fluorescence (FL) quantum yield decrease upon concentration increase is called concentration quenching (CQ). Despite the fact that this phenomenon has been observed for various materials [1,2], its nature is not completely understood. Most likely, the origin of CQ varies for different compounds: a statistical pair of molecules could act as an excitation trap, or some molecules may form H-dimers, which quench FL. Most studies focus on characteristics such as the average FL lifetimes or FL quantum yield. However, FL decay kinetics with increasing concentration could provide useful information [3]. For example, Förster Resonance Energy Transfer (FRET) [4] could be detected through changes in the kinetics [3].

In this study we investigate the picture of FL concentration quenching in 2,9,16,23-TETRA-TERT-BUTYL-29H,31H-PHTHALOCYANINE (TTBpc; Fig. 1a) and ZINC 2,9,16,23-TETRA-TERT-BUTYL-29 H,31 H-PHTHALOCYANINE (ZnTTBpc; Fig 1c). We studied CQ by varying concentration of phthalocyanine by two orders of magnitude, from 0.1 mM up to 10 mM, and

recording FL spectrum with FL decay kinetics (Figs 1b and 1d). The spectra do not change, while time-resolved kinetics exhibit severe changes with concentration increase. Firstly, all the kinetics are fitted with the stretched-exponential function $\exp\left[-\left(\frac{t}{\tau}\right)^b\right]$ to observe the deviations from mono-exponential decay of unquenched species.

To explain the experimental data, we apply donor-trap model, where a single donor molecule is surrounded by an infinite number of acceptors. For this reason, all the kinetics are fitted with $\exp\left[-t/\tau_D - (t/\tau_2)^{1/2}\right]$ function (called 'DAC'), where τ_D is the decay rate of excited donor molecule in the absence of acceptors and τ_2 represents quenching due to acceptors. We state that FRET from monomer species to H-dimers of the corresponding material occurs.

References

1. G.S. Beddard, Nature, 78 – 80 (1976).
2. J. Tamošiūnaitė, S. Streckaitė, J. Chmeliov, L. Valkunas and A. Gelzinis, Chem. Phys., **572**, 111949 (2023).
3. S. Barysaitė, J. Chmeliov, L. Valkunas and A. Gelzinis, J. Phys. Chem. B, **128**, 4887–4897 (2024).
4. T. Förster, Ann. Phys., **437**, 55–75 (1948).

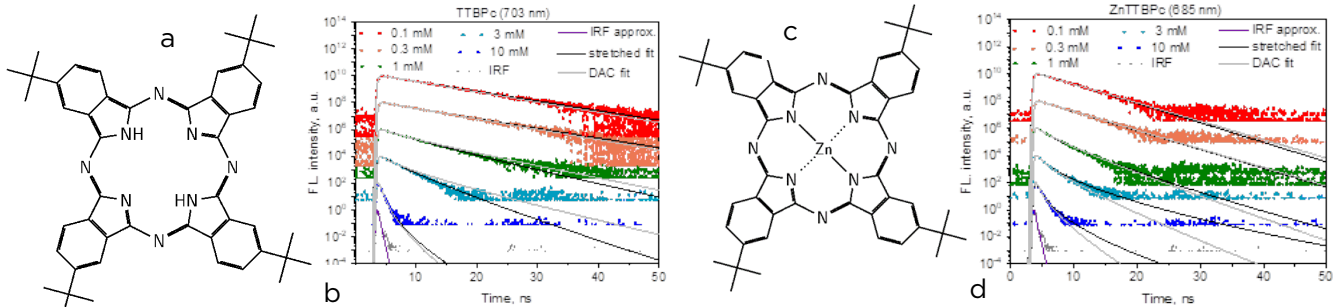


Fig 1. Molecular structure of TTBpc (a) and its decay kinetics (b);
Structure of ZnTTBpc (c) and kinetics (d).

OPTOELECTRONIC SIMULATION OF CONVENTIONAL AND PLASMONIC PHOTOCONDUCTIVE ANTENNAS BASED ON FINITE ELEMENT METHOD (FEM)

Mohammad Esmaeil Daraei^{1*}, Mehdi Abedi-Varaki², and Ignas Nevinskas¹

¹Department of Optoelectronics, Center for Physical Sciences and Technology,
Saulėtekio av. 3, LT-10257 Vilnius, Lithuania.

²Department of Laser Technologies, Center for Physical Sciences and Technology,
Savanošiu av. 231, LT-02300 Vilnius, Lithuania.

*email: esmaeil.daraei@ftmc.lt

The Terahertz (THz) band, located between the microwave (MW) and infrared (IR) regions of the electromagnetic (EM) spectrum, has garnered significant interest in research [1]. THz radiation has potential applications in various fields, including wireless communication, explosive detection, pharmaceuticals, spectroscopy, and imaging [2].

Photoconductive antennas (PCAs) are currently utilized as THz emitters and detectors [3]. A PCA consists of a photo-absorbing substrate (low temperature grown Gallium Arsenide (LT-GaAs) in this study) and a metallic dipole antenna biased with a direct current (DC) voltage that efficiently radiates THz waves. When a short pulse laser is illuminated on the PCA, photons are absorbed in the semiconducting substrates, resulting in electron-hole pairs generation. The electric field, established by an external DC bias between the electrodes, separates the photo-generated electrons and holes. The resulting photocurrent pulse is fed into the antenna, and the electromagnetic pulse radiates into free space.

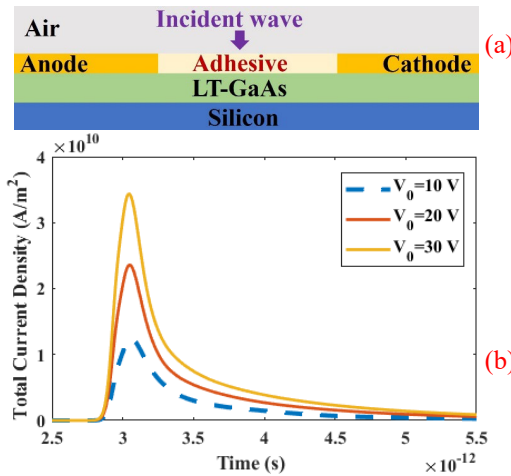


Fig.1. (a) Conventional PCA, (b) Total current density vs time for a Conventional PCA applying different voltages.

Recent research has employed plasmonic nanostructures to improve the efficiency of THz PCAs. These nanostructures interact with the incoming laser light, boosting optical absorption in the active photoconductive region, which leads to an increased concentration of free carriers and enhanced carrier gradients.

This study employs the finite element method (FEM) to simulate the THz PCA through solving the

Maxwell's equations alongside the coupled drift-diffusion and Poisson's equations. The computational modeling is divided into two steps: (1) calculating the optical response by determining the spatial distribution of the optical field and (2) determining the electronic response by solving the time-domain forms of the coupled drift-diffusion and Poisson's equations, using carrier generation derived from the first step.

We studied the conventional bottom-embedded thin-film (CBETF) and plasmonic bottom-embedded thin-film (PBETF) PCAs which are illustrated in Fig. 2.

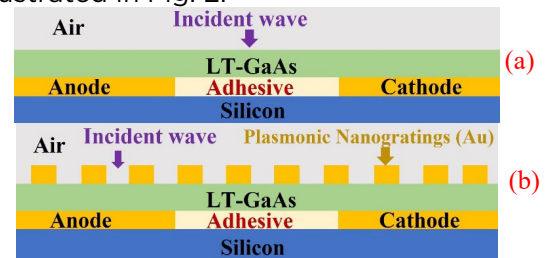


Fig.2: Illustrations of the (a) CBETF and (b) PBETF THz PCA.

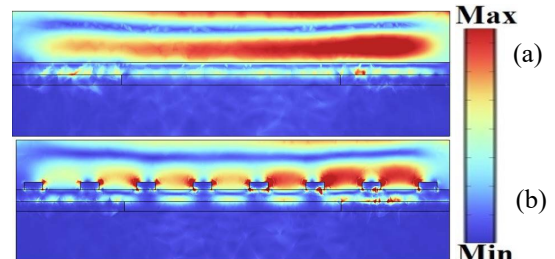


Fig. 3. Electric field for (a) CBETF, and (b) PBETF THz PCAs.

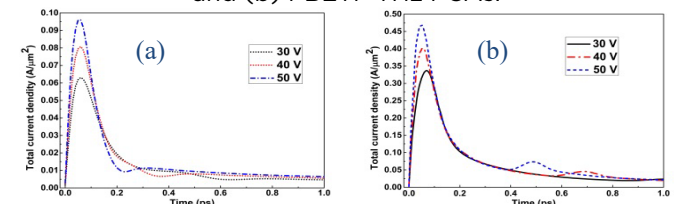


Fig. 4. Total current density vs time for (a) CBETF, and (b) PBETF THz PCAs applying different voltages.

References

- Christopher W Berry and Mona Jarrahi 2012 New J. Phys. 14 105029.
- Tonouchi, M. Cutting-edge terahertz technology. Nat. Photonics 1, 97-105 (2007).
- Ghorbani, S. et al. Thin film tandem nanoplasmionic photoconductive antenna for high performance terahertz detection. Superlattices Microstruct. 120, 598-604 (2018).

APPLICATION OF TERAHERTZ TIME-DOMAIN SPECTROSCOPY FOR OBSERVATION OF POLYMER CURING CHEMICAL REACTIONS

Ihor Krapivin¹, Mykolas Šikas¹, Ramūnas Adomavičius¹

¹Center for Physical Sciences and Technology, Department of Optoelectronics
Saulėtekio av. 3, LT-10257 Vilnius, email: ihor.krapivin@ftmc.lt

In this study, the terahertz time-domain spectroscopy (THz-TDS) technique was employed to monitor the photochemical and polymerization reactions of epoxy resin. The curing process of six types of epoxy adhesives and five types of UV-curing adhesives was investigated.

The terahertz absorption spectra of liquid epoxy resins are characterized by several absorption lines. During curing, the center frequencies of some lines shift, and some lines disappear. Additionally, it was found that the transparency of epoxy resins to terahertz radiation depends on their state: liquid, colloidal, or solid. The colloidal state of epoxy resin is the least transparent, while the fully cured epoxy resin is the most transparent.

When studying UV-curing adhesives, it became evident that the rate of the photochemical reaction depends on the intensity of UV radiation (Fig.1). It was also established that the refractive index of the hardened material varies with the intensity of optical radiation.

Our work demonstrates that the terahertz time-domain spectroscopy (THz-TDS) technique is an excellent tool for monitoring polymerization reactions, as the curing process significantly alters the optical properties of polymers in the terahertz wavelength range.

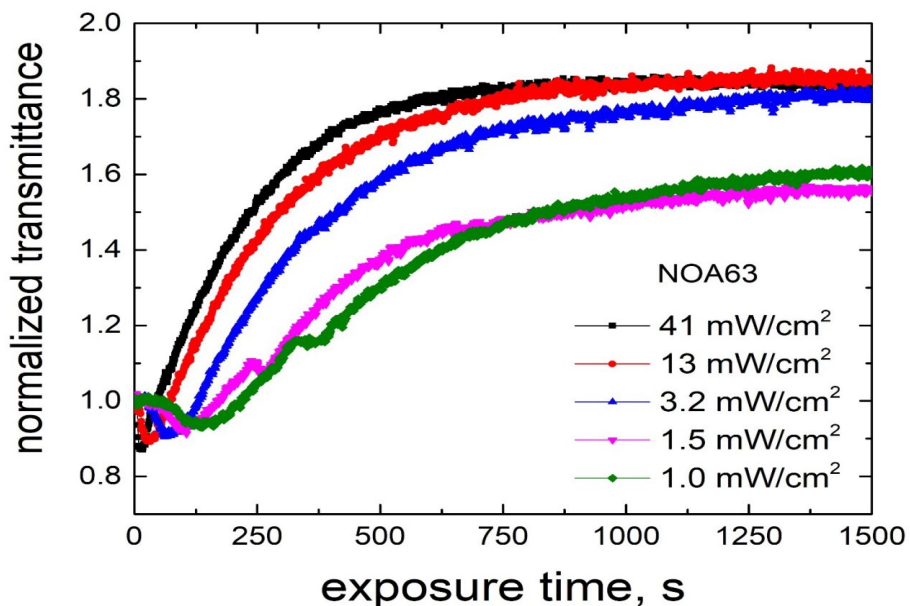


Figure 1. Normalized transmittance of UV-curable adhesive at different excitation intensities of UV light. Probing radiation frequency - 0.2 THz. The start of the time countdown coincides with the switching-on of the light source. The stabilization of transmittance at a constant level coincides with the hardening of the polymer "NOA63".

MODIFIED EdgeFET DESIGN FOR SENSITIVE ROOM-TEMPERATURE TERAHERTZ DETECTION

Maxim Moscotin, Miroslav Saniuk, Justinas Jorudas and Irmantas Kašalynas

Center for Physical Sciences and Technology, Department of Optoelectronics
Saulėtekio av. 3, LT-10257 Vilnius, email: maxim.moscotin@ftmc.lt

Sensitive room-temperature terahertz detection remains an important problem. TeraFETs have been recently demonstrated to be both sensitive and fast THz detectors [1]. However, the largest sensitivity achievable in the plasmonic-resonant regime occurs at a specific frequency depending on the geometrical parameters of the conductive part of the detector [2]. To enable plasmon-frequency tunability, an EdgeFET design has been proposed [3], in which two gate electrodes surround the channel of the HEMT detector. Applying voltage to the edge gates depletes the edge parts of the channel, making it possible to control the channel width electrically, which is crucial for the plasmon frequency. However, the devices demonstrated had rather high threshold voltage, which meant noise problems and poor convenience in application.

In this work, we propose the original EdgeFET design modification, combining it with the classical FinFET configuration. The proposed modified EdgeFET design is intended to increase the gating efficiency, reducing the threshold voltage of the detector and, thus, the noise and required DC bias.

We implemented the detectors on a SiC substrate with a stacked structure of a 62-nm AlN nucleation layer, 2.4-nm GaN cap, a 20.5-nm $\text{Al}_{0.25}\text{Ga}_{0.75}\text{N}$ barrier, and a 255-nm GaN channel. The channel formation was performed by reactive ion etching, while the Ti/Al/Ni/Au contact metallization and the Ni/Au gate metallization were done by e-beam evaporation. Both ohmic source-drain and capacitive gate electrodes were designed to be attached to individual bow-tie antennas, enabling THz coupling. Electrical characterization of the fabricated TeraFETs revealed a low threshold gate voltage of -2.5 to -3 V for the classical FinFET and the modified EdgeFET designs. The previously proposed EdgeFETs demonstrated a threshold gate voltage of -40 to -120 V. The steepness of the threshold slope in the case of the modified EdgeFETs was up to several orders larger compared to unmodified EdgeFETs, which can be explained by lower gate leakage current at lower gate voltages. This is an important feature for THz detection, as the Seebeck coefficient is proportional to the first derivative of the transfer-to-gate function. THz radiation absorption generates localized heating, and the temperature gradient created within the channel drives electron movement due to the thermoelectric effect. If the material has a non-zero Seebeck coefficient, this results in a voltage difference, which can be

measured and used to detect the incident THz radiation. Thus, the sensitivity of a TeraFET detector directly depends on the steepness of the gate threshold slope.

For the THz detection characterization, the samples were bundled with a Si-lens. The assembly was exposed to 150 and 300 GHz radiation focused by an OAP mirror. The position of the sample was always optimized by signal amplitude. Responsivity was measured for multiple channel lengths at each gate configuration: fully covered channel in case of a FinFET, side gate in case of an EdgeFET, and side gates with an interconnection over the channel in case of an m-EdgeFET.

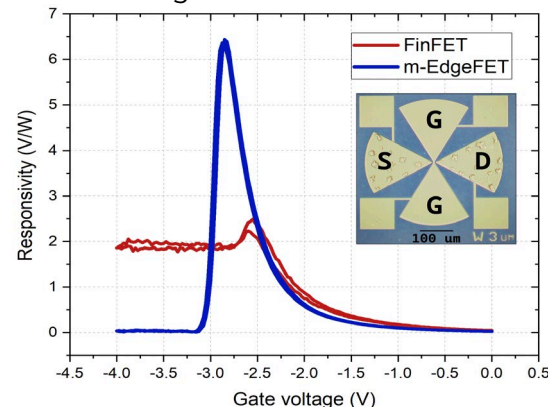


Fig.1. Room temperature responsivity to 300 GHz of a FinFET (red) detector and a modified EdgeFET detector (blue), depending on the gate voltage. The inset shows an overview of the detector.

The room temperature responsivity to linearly polarized 300 GHz radiation, coupled with the source-drain antenna, for samples of two gate configurations, FinFET and m-EdgeFET, having identical dimensional parameters of the channel, is shown in Fig.1. Due to the decreased area of the channel-gate overlapping the modified EdgeFET configuration has lower gate leakage, which results in over three times higher responsivity values than in case of a regular FinFET detector. M-EdgeFET HEMTs were experimentally proven to operate as sensitive room-temperature THz detectors, combining effective gating and low gate leakage current.

References:

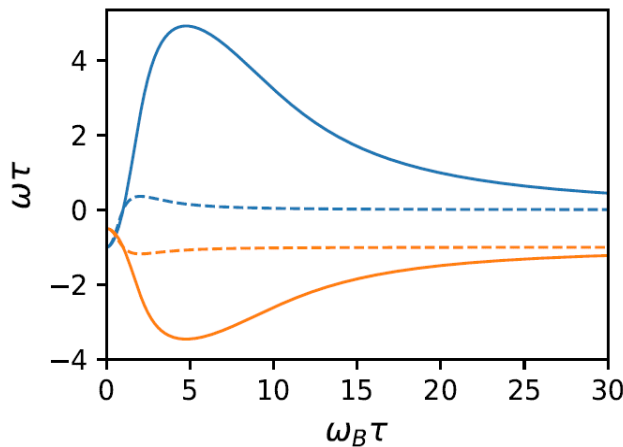
1. M. Bauer et al., "A High-Sensitivity AlGaN/GaN HEMT Terahertz Detector With Integrated Broadband Bow-Tie Antenna," in IEEE Transactions on Terahertz Science and Technology, vol. 9, no. 4, pp. 430-444, (2019).
2. Pashnev D. et al. "Terahertz time-domain spectros-copy of two-dimensional plasmons in AlGaN/GaN heterostructures." Applied Physics Letters, 117 – №. 5 (2020).
3. Sai, P., et al. "AlGaN/GaN field effect transistor with two lateral Schottky barrier gates towards resonant detection in sub-mm range." Semiconductor Science and Technology 34.2: 024002 (2019).

SUPERGARDELĖS PLAZMONINIŲ TIKRINIŲ MODŲ YPATYBĖS BLOCHO STIPRINIMO REŽIME

Lukas Stakėla, Kirill N. Alekseev

Fizinių ir technologijos mokslų centras, Optoelektronikos skyrius
Saulėtekio al. 3, LT-10257 Vilnius, el. p.: lukas.stakela@ftmc.lt

Nuolatinės srovės puslaidininkinės supergardelės gali veikti neigiamo diferencialinio laidumo režimu dėl sužadintų elektronų Blocho virpesių [1]. Šis veikimo režimas potencialiai gali lemti aukšto dažnio Blocho stiprinimą, dėl kurio gali būti stiprinami GHz-THz signalai [2]. Prietaisai paremti supergardelėmis gali veikti kambario temperatūroje, kuo iš esmės skiriasi nuo šiuo metu egzistuojančių ir plačiai naudojamų terahercinių kvantinių kaskadinių lazerių, kuriems vis dar reikalinga itin žema temperatūra. Supergardelėje stiprinamas kintamosios srovės signalas gali būti skersinė elektromagnetinė banga (optinis stiprinimas) arba išilginė erdvinio krūvio banga (plazmoninis stiprinimas). Fiziniai plazmoninio stiprinimo mechanizmai šiose kvantinėse struktūrose vis dar yra mažai ištýrinėti, todėl tai apima pagrindinę mūsų mokslinio domėjimosi sritį.



1 pav. Nestabilios relaksacijos modos (mėlyna) padidėjimas ($\omega_l > 0$) ir stabilios hibridinės modos (oranžinė) sumažėjimas dviem plazmos parametru reikšmėmis: $\omega_p\tau = 2$ (brükšninė linija) ir $\omega_p\tau = 20$ (vientisa linija).

Šiame tyrime remdamiesi istoriniu darbu [3], apskaičiuojame ir analizuojame supergardelės, su nuolatine srove, kompleksinius skersinių plazmos modų ($\sim \exp(-i\omega t)$) tikrinius dažnus ($\omega = \omega_R + i\omega_I$). Modų elgseną daugiausia lemia du parametrai: $\omega_B\tau$ ir $\omega_p\tau$ (Blocho ir plazmos dažniai bei sklaidos laikas – τ). Kai $\omega_B\tau > 1$ ir $\omega_p\tau > 1$, Blocho ir plazmos virpesiai yra sužadinami ir hibridizuojami į aukštadažnę „hibridinę Blocho ir plazmos modą“. Tuo pačiu metu žemo dažnio „relaksacijos moda“ tampa nestabili. Mūsų skaičiavimai rodo gerą atitinkamą apytiksliams analitiniams sprendiniams, rastiems [2], kai $\omega_p\tau \leq 1$. Taip pat šiame tyrime nagrinėjame įdomų ribinį atvejį, atitinkantį stipriai legiruotas supergardeles [4], ko pasekoje randame labai didelį nestabiliosios modos prieaugį, kurio atsiradimas sutampa su žymiu hibridinės modos nykimo spartos padidėjimu [žr. 1 pav.] Mūsų atradimai suteikia naudingų įžvalgų, padedančių suprasti ir vystyti naujus plazmoninius įrenginius.

Literatūra

1. Esaki, L. and Tsu, R., IBM J. Res. Dev. 14, 61-65 (1970).
2. Ktitorov, S. A., Simin, G. S. and Sindalovskii, V. Y., Fiz. Tverd. Tela 13, 2230-2233 (1971).
3. Ignatov, A. A. and Shashkin, V. I., Sov. Phys. JETP 66, 526 (1987).
4. Renk, K. F. et al., Phys. Rev. Lett. 95, 126801 (2005).

TERAHERTZ SPECTROSCOPY OF RECTANGULAR METASURFACES FORMED ON n-GaAs/GaAs STRUCTURES

Barbora Škėlaitė^{1,2}, Vytautas Jakštas³, Marius Treideris³, Andrius Bičiūnas¹,
Kęstutis Ikamas⁴, Renata Butkutė¹ and Ignas Grigelionis¹

¹Center for Physical Sciences and Technology, Department of Optoelectronics

²Vilnius University, Institute of Photonics and Nanotechnology

³Center for Physical Sciences and Technology, Department of Physical Technologies

⁴Vilnius University, Institute of Applied Electrodynamics and Telecommunications
Saulėtekio av. 3, LT-10257 Vilnius, email: barbora.skelaita@ff.stud.vu.lt

Ever-growing field of terahertz (THz) technology, specifically imaging applications, require polarization sensitive, efficient, compact and easy to operate solid state thermal emitters [1]. Currently, widely known devices, such as quantum cascade lasers or 2DEG plasmonic emitters require elaborate processing and additional cryogenic cooling [2], which limits the application of such devices in imaging systems. Thermal emitters coupled with metasurfaces can act as an attractive alternative, as they provide narrow resonant emission with peak quality similar to those of 2DEG plasmonic devices and can operate at higher temperatures [3]. Such emitter has a structure of a conductive bottom layer, insulating layer and metallic metasurface layer on top, all of which allows the excitation of resonant magnetic polaritons.

In this work, a dual frequency thermal emitter composed of GaAs based semiconductor structure equipped with metallic metasurface arranged from periodic rectangular-shaped metacells is proposed and demonstrated experimentally. The structure of the thermal emitter consisted of 500 μm -thick n-type GaAs substrate layer with 4.3 μm GaAs spacer layer grown on top using molecular beam epitaxy. The metasurface was formed on top of the spacer layer using UV laser lithography and metal lift-off

process to produce 200 μm -thick periodic layer of rectangular metacells. The optical properties of the samples were measured to determine samples reflectivity and emissivity.

Acquired reflection spectra (fig. 1) demonstrates the resonant 1st and 3rd harmonic frequency peaks resulting from the excitation of magnetic polaritons. Due to the rectangular-shaped metasurface structure the dual frequency peak can be seen depending on the polarization. Spectra shows the 1st harmonic s-polarized dip at 1.93 THz and p-polarized at 1.6 THz. Furthermore, the 3rd harmonic is seen at 4.04 THz and 3.74 THz for s-polarization and p-polarization respectively.

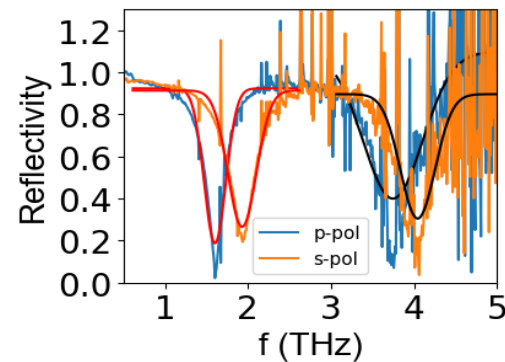


Fig. 1. Experimental reflectivity spectrum of THz thermal emitter equipped with metasurface at two perpendicular polarizations. The lines represent Lorentzian function fits of 1st harmonic (red) and 3rd harmonic (black) resonant frequencies.

References

1. Leitenstorfer A. et al. The 2023 terahertz science and technology roadmap. *J. Phys. D: Appl. Phys.* **56**, 223001 (2023).
2. Bosco L. et al. Thermoelectrically cooled THz quantum cascade laser operating up to 210 K. *Applied Physics Letters* **115**, 010601 (2019).
3. Alves F., Kearney B., Grbovic D. and Karunasiri G. Narrowband terahertz emitters using metamaterial films. *Opt. Express, OE* **20**, 21025-21032 (2012).

APERTURE PHOTOMETRY LIMITS IN STAR CLUSTER STUDIES

Karolis Daugevičius, Eimantas Kriščiūnas, Erikas Cicénas, Rima Stonkutė, Vladas Vansevičius

Center for Physical Sciences and Technology, Department of Fundamental Research
Saulėtekio av. 3, LT-10257 Vilnius, email: karolis.daugevicius@ftmc.lt

Studies of star clusters and their physical/structural parameters allow us to understand how galaxies form and evolve. Aperture photometry is a powerful method that enables studies of star cluster systems covering a wide range of cluster parameters. However, accuracy of the method strongly depends on numerous effects, including stochasticity, environmental effects, intrinsic limits of such methodology, and others. Thus, in our study we aim to determine accuracy and applicability limits of the aperture photometry approach for star cluster studies.

We simulated a large grid of realistic stochastic star cluster models covering parameter space of the real M31 clusters. Images were modelled in six photometric passbands to match Panchromatic Hubble Andromeda Treasury (PHAT) survey [1] performed with *Hubble Space Telescope* (HST). We placed our simulated clusters in 5 locations of M31 disc at different radial distances, representing environments of various stellar density, and measured them using aperture photometry method (see Fig. 1).

In our study [2] of the background-less case (B0 as shown in Fig. 1.) we found that due to stochastic effects young low-intermediate mass star clusters without and with post-main-sequence stars exhibit large photometric differences – this makes cluster physical parameter determination based on aperture photometry problematic at ages $\lesssim 30$ Myr.

In Fig. 2, we show how photometry errors in different environments depend on aperture radius, R_{ap} . Generally, errors decrease with increasing aperture size and cluster mass, meanwhile they increase with age and higher background level. However, we found that accuracy gain is small for apertures beyond the cluster half-light radius and measurements using small apertures can be relatively more accurate.

In Fig. 3, differences of colour index $F475W - F814W$ when measured in background fields and the background-less case, are shown. We found, that in (semi-)resolved dense fields, bright background stars that are mostly red can introduce reddening effect, when clusters are measured with large apertures. We suggest that this can be minimized using smaller apertures to measure colour indices, as proposed in the adaptive aperture photometry method, that we introduced in the previous studies of real M31 star clusters [3, 4].

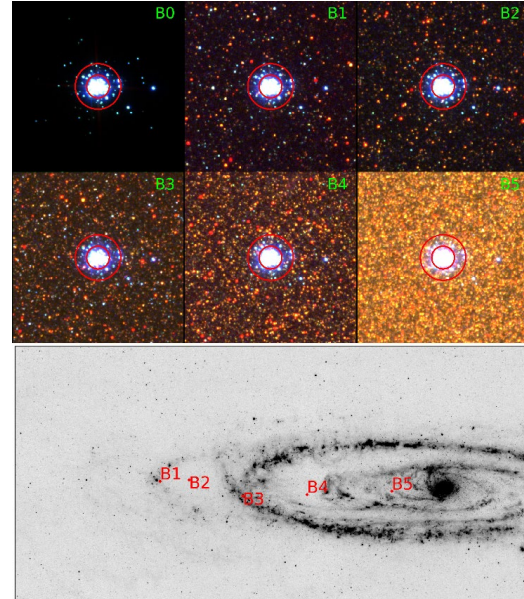


Fig. 1. $F336W/F475W/F814W$ colour images of one model cluster (mass of $3000 M_\odot$ and age of 10 Myr) placed in different M31 environments. B0 – no background. Red circles – apertures with radii (R_{ap}) of 1 and 2 arcsec. Bottom panel – locations of B1-B5 fields marked on the map of M31 (*Spitzer* MIPS $24\mu m$ image).

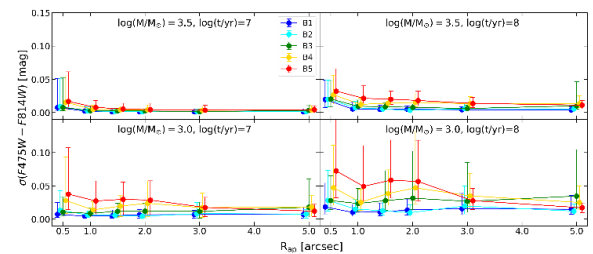


Fig. 2. Photometry errors arising due to aperture positioning and size biases. Error bars – 16–84 percentile ranges. Results for clusters with half-light radii in the range of 0.2–1.0 arcsec are shown. Mass and age of models are indicated in panels.

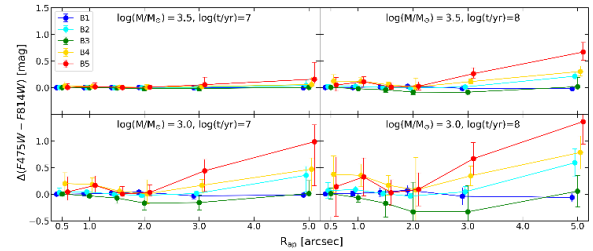


Fig. 3. Differences of $F475W - F814W$ when measured in background fields (B1-B5) and the B0 case. Error bars – 16–84 percentile ranges. Results for clusters with half-light radii in the range of 0.2–1.0 arcsec are shown here. Mass and age of models are indicated in each panel.

References

1. J. J. Dalcanton, B. F. Williams, D. Lang, et al., *Astrophys. J. Supplement Series*, **200**, 18 (2012).
2. K. Daugevičius, E. Kriščiūnas, E. Cicénas, et al., *Astron. Astrophys.*, **688**, A131 (2024).
3. R. Naujalis, R. Stonkutė, and V. Vansevičius, *Astron. Astrophys.*, **654**, A6 (2021).
4. E. Kriščiūnas, K. Daugevičius, R. Stonkutė, V. Vansevičius, *Astron. Astrophys.*, **677**, A100 (2023).

STAR CLUSTERS IN THE DISK OF ANDROMEDA GALAXY

Eimantas Kriščiūnas, Karolis Daugevičius, Eriks Cicēnas,
Rima Stonkutė, Vladas Vansevičius

Center for Physical Sciences and Technology, Department of Fundamental Research
Saulėtekio av. 3, LT-10257 Vilnius, email: eimantas.krisciunas@ftmc.lt

Star clusters are essential for understanding the formation and evolution processes of their host galaxies. Most stars form in embedded star clusters (Lada & Lada 2023), therefore knowledge of the physical parameters of a cluster population (e.g., age, mass, chemical composition, and interstellar extinction) is crucial for constraining the star formation history of the galaxy and understanding the processes that drive star formation.

The Andromeda galaxy (M31) is one of the best sites for studying star formation within galaxy disks due to its complex history and structure (Lewis et al. 2015; Williams et al. 2017). The M31 disk star cluster studies have been made possible by the extensive Panchromatic Hubble Andromeda Treasury (PHAT) survey (Dalcanton et al. 2012) performed with the *Hubble Space Telescope* (HST). PHAT has covered a significant portion of the M31 disk, resulting in the largest star cluster catalogue (Johnson et al. 2015) of 2753 clusters.

In this presentation, we aim to explore the connections between star clusters and the star formation history of the M31 disk using PHAT data. By analysing the parameters of individual clusters – age, mass, extinction, and metallicity – we explored the radial and azimuthal distributions of clusters, revealing insights into the recent evolution of the M31 disk.

We measured the radial profiles of cluster surface density for two age groups, focusing on the azimuthal segment from -25° to $+35^\circ$ around the major axis (Fig. 1). Star-forming rings at ~ 6 , ~ 10 , and ~ 15 kpc from the centre were identified, with the 15 kpc ring primarily consisting of clusters younger than 100 Myr. The small radial dispersion of cluster groups over ~ 300 Myr implies a radial velocity dispersion below ~ 2 km/s, showing that star clusters serve as stable, long-term tracers of star-forming regions in disk galaxies.

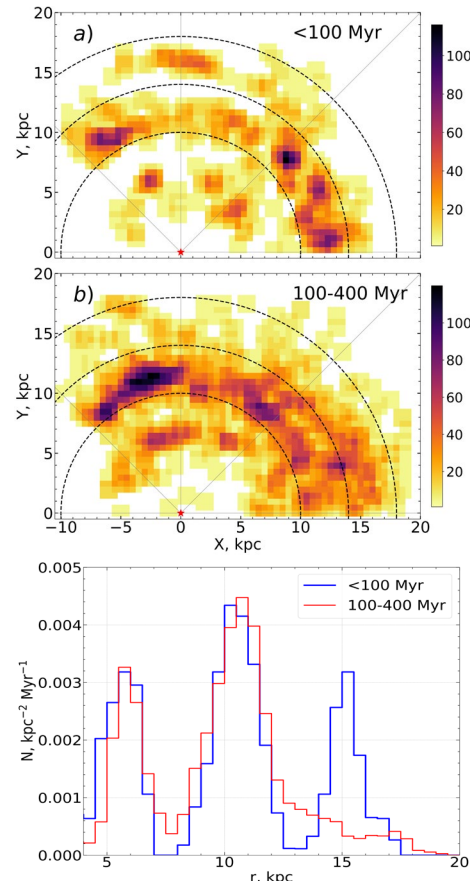


Fig. 1. Top: The maps of massive ($>800 M_\odot$) star cluster surface number densities in the M31 disk. The cluster number densities, kpc^{-2} , are colour-coded according to the bars. The circles indicate 10, 14, 18 kpc distances from the galaxy centre. Bottom: The radial profiles of star cluster surface number density calculated per Myr in two age ranges within the azimuthal segment of 60° (from -25° to $+35^\circ$). The blue line represents younger (≤ 100 Myr) and the red line – older ($100 < t \leq 400$ Myr) clusters.

References

1. C. J. Lada & E. A. Lada, *ARA&A*, **41**, 57 (2003).
2. A. R. Lewis, A. E. Dolphin, J. J. Dalcanton, et al., *ApJ*, **805**, 183 (2015).
3. B. F. Williams, A. E. Dolphin, J. J. Dalcanton, et al., *ApJ*, **846**, 145 (2017).
4. J. J. Dalcanton, B. F. Williams, D. Lang, et al., *ApJS*, **200**, 18 (2012).
5. L. C. Johnson, A. C. Seth, J. J. Dalcanton, et al., *ApJ*, **802**, 127 (2015).

MAGNETIC FIELD DYNAMICS DURING MAGNETIC PULSE FORMING AND CRIMPING

Pavel Piatrou, Voitech Stankevič, Skirmantas Keršulis, Vilius Vertelis, Nerija Žurauskienė

Center for Physical Sciences and Technology, Department of Functional Materials and Electronics
Saulėtekio av. 3, LT-10257 Vilnius, email: pavel.piatrou@ftmc.lt

Forming and crimping metals with pulsed magnetic fields is a modern, environmentally friendly method that eliminates the need for mechanical pressure. This process uses short high-amplitude pulsed magnetic fields and the analysis of these dynamics provides important insights for evaluating quality and optimizing the process. This paper presents a computerized fast magnetic field measurement system that enables precise measurements of pulsed magnetic fields up to 20 T with 40 µs duration. To study the magnetic field dynamics in magnetic pulse forming and crimping, we developed a setup consisting of capacitors, a Bitter coil, a spark gap. The setup allows for short pulsed magnetic fields, which we recorded with a fast B-scalar meter. We conducted a series of experiments that consist of three stages. At each stage, we modified the experiment so that its results could be compared with a result obtained at the previous stage.

On first stage, we investigated how the presence of an aluminum rod affects the magnetic field in the field shaper of Bitter coil. For this purpose, in the first case we measured the magnetic field near the inner surface when only the field shaper was present, and in the second case with an inserted aluminum rod of 6.8 mm diameter. In both cases, the capacitors were charged up to 11.5 kV. The results are shown in Fig 1.

On a second stage, we investigated an aluminum tube forming. We inserted the aluminum tube with a diameter of 6.8 mm into the field shaper and recharged the capacitors up to 11.5 kV. The energy stored in the capacitors was sufficient to initiate the plastic deformation of the tube after discharge. Fig. 2 presents the results for both the non-deformable rod and the tube that deforms plastically in the magnetic field shaper.

On a third stage, the same 6.8 mm aluminum tube was used to crimp two steel rods with diameters of 4.5 mm and 5 mm, respectively, under identical capacitor charging voltage of 11.5 kV. The results of the crimping processes were compared to the tube deformation observed on previous stage. Since it was found that the plastic deformation occurs during the first half-wave, Fig. 3 shows only a detailed view of the first peak.

When a non-deformable aluminum rod (6.8 mm diameter) was inserted into the field shaper, the magnetic field amplitude in the 700 µm gap increased by about 19%, due to induced currents on the rod's surface, which generate a magnetic field aligned with the external field and lead to a higher measured magnetic flux density. In this case the signal period slightly decreased due to increased

reactive impedance. Comparisons between non-deformable rods and deforming tubes of the same diameter revealed plastic deformation of aluminum starting 5 µs after discharge. When crimping aluminum tubes and steel rod, the fast B-scalar meter allows registering a time of impact. For the 5 mm steel rod, the flyer tube moves 500 µm, and impact occurs 2 µs after the start of plastic deformation. With the 4.5 mm rod, the flyer tube moves 750 µm and impact occurs 3.5 µs later. Crimping occurred within the first half-period of the signal.

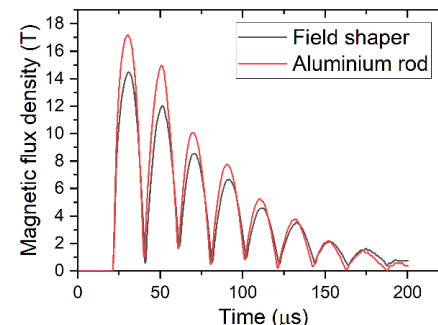


Fig. 1. Time dependence of magnetic flux density in the field shaper (black) and with inserted rod (red).

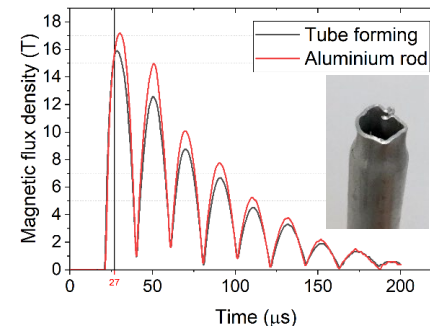


Fig. 2. Time dependence of magnetic flux density in the field shaper with inserted rod (red) and with the Al tube (red). The inset shows the image of the formation.

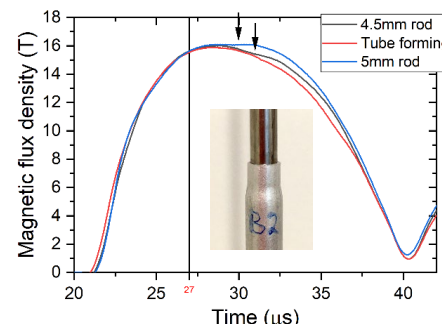


Fig. 3. Time dependence of magnetic flux density during crimping flyer tube around a 4.5 mm steel rod (black), a 5 mm steel rod (blue), and the tube formed without impact (red). The arrows show the impact moments.

References

1. Sensors 2020, 20(20), 5925; DOI: 10.3390/s20205925
2. Sensors 2023, 23(3), 1435; DOI: 10.3390/s23031435

PAVIRŠINIO PLAZMONO IR R6G EKSITONO EMISIJA STIPRIOSIOS SĄVEIKOS REŽIME

Povilas Jurkšaitis¹, Justina Anulytė¹, Dovydas Banevičius²,
Ernesta Bužavaitė-Vertelienė¹, Zigmantas Balevičius¹

Fizinių ir technologijos mokslų centras, Lazerinių technologijų skyrius, Plazmonikos ir nanofotonikos laboratorija
Saulėtekio al. 3, LT-10257 Vilnius, Lietuva el. p.: povilas.jurksaitis@ftmc.lt

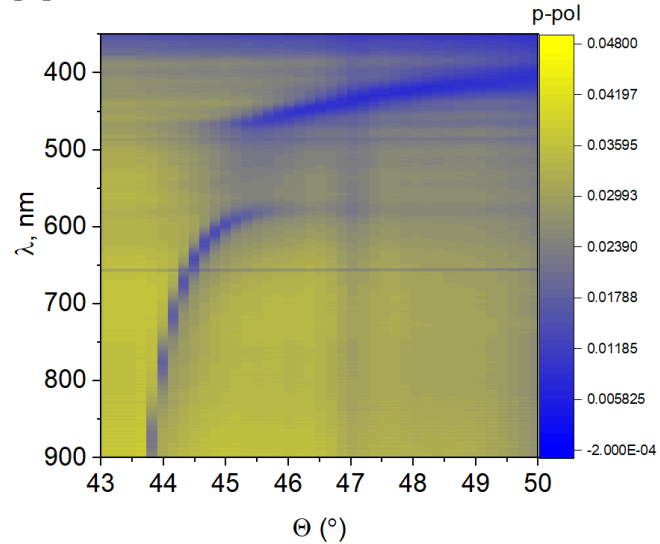
Fotonikos ir nanotechnologijų institutas, Fizikos Fakultetas, Vilniaus universitetas,
Saulėtekio al. 3, LT-10257 Vilnius, Lietuva

Paviršinio plazmono emisija (SPCE) iškilo kaip fluorescencijos aptikimo technologija biologijoje, biotechnologijos moksluose ir medicinos diagnostikoje. Naujas SPCE technologijos priėjimas leidžia smarkiai padidinti fluorescencijos signalo surinkimo efektyvumą transformuojant įprastai izotropinę, nuo kampo nepriklausomą, daugiadalelių fluorescencinių dažų emisiją į kryptingą[1] emisiją kuri vyksta plazmonų emisijos rezonanso kampu. Tai pasiekiamą kai fluorescencijos signalas iš molekulinių dažų sužadina plazmoninę bangą rezonanso sąlygomis ir paprastai atliekama įdedant emiterius į artimą lauką plazmonėse nanostruktūrose[2]. Paviršinio plazmono emisijos metu, dažo gesimo trukmė yra modifikuojama dėl atsiradusio Purcell efekto, tačiau dažo emisijos spektras išlieka nepakitęs. [3].

Spektroskopinė elipsometrija buvo naudojama siekant išsiaiškinti bandinių sugerties spektrus prie skirtinigų kritimo kampų ir įvertinti sugerties dispersiją. Fluorescencijai tolimajame lauke įvertinti buvo naudojama Furjė mikroskopija parodanti emisijos kampų pasiskirtymą. Atskira optinė schema buvo surinka siekant įvertinti fluorescencijos spektrus prie skirtinį kampą.

Šiame darbe buvo tyrinėjama emisiją iš mėginių, pasižyminčiu stipriosios sąveikos dinamika. Eksperimentiniai metodai, apimantys spektroskopinę elipsometriją ir Furjė mikroskopiją, buvo atlikti naudojant Rodamino 6G fluorescencinių dažų sluoksnius, suformuotų ant plonų sidabro 45 nm sluoksnių. Pav. 1 pavaizduota bandinio spektroskopinės elipsometrijos matavimas parodo modifikuotas dispersijos kreives – ties 470 nm esanti R6G dažo sugerties linija tampa priklausoma nuo šviesos kritimo kampo. Tai patvirtinta, kad sistema yra stipriojoje saveikoje. Mėginiams stipriosios sąveikos režime buvo stebima kryptinė emisija, taip pat modifikuotas emisijos spektras atsiradęs

dėl Rabi osciliacijų. Eksperimentai, apimantys Rodamino gesimo trukmės matavimus stipriosios sąveikos režime, gali rodyti reikšmingą gesimo trukmės sumažėjimą. Fluorescencijos gesimo trukmės matavimai pikosekundžių skalėje galėtų turėti didžiulės naudos dėl sumažėjusio gesimo laiko, tai padidintų kvantinės Hong-Ou-Mandelio interferencijos matomumą [4].



Pav. 1. Modifikuota rodamino 6G molekulių sugerties dispersijos kreivė stipriosios sąveikos režime.

Literatūra

1. M. Chen, S.-H. Cao, and Y.-Q. Li, *Anal. Bioanal. Chem.* **412**, 6085 (2020).
2. L. Novotny, B. Hecht, *Principles of Nano-Optics*, 2nd ed. Cambridge University Press (2012)
3. P. Berini and I. De Leon, *Nat. Photonics* **6**, 16 (2012).
4. A. Lyons, V. Zickus, R. Álvarez-Mendoza, D. Triggiani, V. Tammaro, N. Westerberg, M. Tassieri, and D. Faccio, *Nat. Commun.* **14**, 8005 (2023).

TAMM' O PLAZMONŲ – POLARITONŲ REZONANSINIO BANGOS ILGIO DERINIMAS NAUDOJANT ATOMINIO STORIO SLUOKSNIO NUSODINIMĄ

Mantas Drazdys¹, Ernesta Bužavaitė-Vertelienė¹, Darija Astrauskytė¹, Zigmantas Balevičius^{1,2}

¹Fizinių ir technologijos mokslų centras, Lazerinių technologijų skyrius,
Saulėtekio al. 3, LT-10257 Vilnius

²Vilniaus Gedimino technikos universitetas, Elektronikos fakultetas,
Naugarduko g. 41, LT-03227 Vilnius
el. p. mantas.drazdys@ftmc.lt

Pastaraisiais metais buvo skiriama daug dėmesio struktūroms sudarytomis iš fotoninio kristalo (PC – angl. k. *photonic crystal*) ir plono metalinio sluoksnio [1]. Tokiose struktūrose, PC ir metalo sluoksnio sąlyčio riboje gali būti generuojama paviršinė moda vadinama Tamm'o plazmonais – poliaritonais (TPP) [2]. TPP yra optinės būsenos panašios į I. Tamm'o aprašytas [3] elektronų būsenas ir susidaro draustinėje energijos juosteje kristalo paviršiuje. Šiuo atveju draustinę energijos juostą atitinka PC stop juosta susidaranti dėl Bragg'o atspindžių periodinėje struktūroje. TPP yra stovinčios bangos, kurias galima sužadinti tiek p-, tiek s-poliarizacijoje [4]. Priešingai nei paviršiaus plazmonų – poliaritonų sužadinimams, kuriems reikalingi papildomi optiniai elementai, tokie kaip prizmės ar gardelės, TPP galima generuoti paprastose optinėse konfigūracijose, o tai atveria galimybes jų taikymui įvairiose srityse: optiniai biosensoriai, juostos pralaidumo filtrai, nanolazeriai ir kitos. Tačiau sėkminges tokį struktūrų taikymas šiose srityse remiasi į tikslų TPP optinių savybių suderinimą bei tikslią TPP rezonanso padėti spektre.

Vienas iš metodų, leidžiančiu įgyvendinti aukštus tikslumo reikalavimus yra atominio storio sluoksnio nusodinimas (ALD – angl. k. *atomic layer deposition*). ALD yra cheminio garų nusodinimo (CVD – angl. k. *chemical vapour deposition*) atšaka, paremta ciklišku pirmtakų dozavimu į reaktorių, per vieną ciklą suformuojant atomo storio sluoksnį, užtikrinant itin didelį nusodintų sluoksnų storio tikslumą bei procesų atkartojamumą. Be to, proceso metu reaktoriuje padengiami visi optinių komponentų

paviršiai, o dangų tankis bei struktūra nenusileidžia jonapluoščiu dulkinimu suformuotoms dangoms, todėl ALD dangos gali pagerinti optinių komponentų parametru stabiliumą bei užtikrina komponento apsaugą nuo aplinkos poveikio [5].

Šio darbo tikslas yra pademonstruoti potencialų ALD metodo taikymą tiksliam TPP rezonansinio bangos ilgio derinimui. Jona-pluoščio dulkinimo metodu (IBS – angl. k. *ion beam sputtering*), periodiškai nusodinant tantalolo oksidą ir silicio oksidą, buvo suformuotas PC. Ant PC ALD metodu buvo nusodinami skirtinių storai Al_2O_3 ir galiausiai magnetroninio dulkinimo metodu (MS – angl. k. *magnetron sputtering*) nusodintas vienodo storio aukso sluoksniai. Spektroskopinės elipsometrijos ir atspindžio matavimų metu fotoninėje draustinėje juosteje buvo stebėtas TPP rezonansas. Buvo nustatyta, kad keičiant Al_2O_3 sluoksnio storj 3 nm, TPP rezonanso bangos ilgis taip pat pasilenka per \approx nm [6].

Literatūra

1. B.L.Afinogenov, V.O.Bessonov, A.A.Nikulin, A.A.Fedyanin, Appl. Phys. Lett. **103**, 061112 (2013).
2. M. Kaliteevski, I.Iorsh, S.Brand, R.A.Abram, J.M.Chamberlain, A.V.Kavokin, I.A.Shelykh, Phys. Rev. B, **76**, 165415 (2007).
3. I. Tamm, Z. Phys., **76**, 849-850 (1932).
4. A.P.Vinogradov, A.V.Dorozeenko, S.G.Erokhin, M.Inoue, A.A.Lisyansky, A.M.Merzlikin, A.B.Granovsky, Phys. Rev. B, **74**, 045128 (2006).
5. S.M.George, Chem. Rev. **110**, 1 (2010).
6. M.Drazdys, E.Bužavaitė-Vertelienė, D.Astrauskytė, Z.Balevičius, Coatings, **14**, 33 (2024).

FABRICATION OF THE FIRST GaAsBi BASED VERTICAL-EXTERNAL-CAVITY SURFACE-EMITTING LASER FOR NIR

A. Zelioli¹, A. Špokas¹, D. Gailevičius², E. Dudutienė¹,
B. Čechavičius¹, A. Vaitkevičius^{1,3} and R. Butkutė¹

1 Center for Physical Sciences and Technology, Saulėtekio al. 3, Vilnius, Lithuania
email: andrea.zelioli@ftmc.lt

2 Laser research center, Vilnius University, Saulėtekio av. 10, Vilnius, Lithuania

3 Institute of Photonics and Nanotechnology, Vilnius University, Saulėtekio av. 3, Vilnius, Lithuania,

This study presents the fabrication of two Vertical-External-Cavity Surface-Emitting Laser (VECSEL) chips. The first chip features InGaAs multiple quantum wells (MQWs) in the gain region, serving as a reference for testing the structure, while the second chip utilizes GaAsBi MQWs. The incorporation of bismuth into the GaAs lattice highly reduces the band gap, 60-90 meV per Bi% [1], enabling longer wavelength emission with minimal Bi content and enhancing bandgap temperature stability. Additionally, this incorporation increases the spin-orbit split-off energy of GaAsBi, reducing non-radiative Auger recombination and making GaAsBi quantum structures promising for optoelectronic applications.

Since their invention, lasers have become indispensable across a wide range of fields, including research, medicine, consumer electronics, and communication. Each of these applications requires a specific set of laser properties, leading to the development of various laser types over time. VECSELs represent a newer class of structures derived from Vertical-Cavity Surface-Emitting Lasers (VCSELs).

Unlike conventional VCSELs, which use a gain region enclosed between two Distributed Bragg Reflectors (DBRs), VECSELs replace the top DBR with an external coupler. The primary advantage of VECSELs over VCSELs is their ability to generate high optical power output while maintaining excellent circular beam quality [2]. The output power of VECSELs is directly proportional to the emitting surface area, making it essential to grow large-area samples with the highest possible optical uniformity [3]. This design allows for optical pumping and provides cavity access, resulting in significantly higher output power, limited primarily by thermal management [4,5]. The bandgap stability of GaAsBi helps overcome this limitation, simplifying thermal management during operation.

The VECSEL structures were grown using a Molecular Beam Epitaxy (MBE) system. A gain region comprising 12 QWs with alternating barrier thicknesses was grown on top of a 30-

period AlAs/GaAs DBR. This configuration, illustrated in Fig. 1, reduces the overall chip thickness, thereby improving thermal management. Special attention was given to avoid the formation of misfit dislocations in the quantum wells to fabricate large chips.

The InGaAs/GaAs MQW gain VECSEL demonstrated lasing at 976 nm from a 500 μm diameter region. Using a similar double quantum well design, a VECSEL with a GaAsBi/GaAs MQW gain area was fabricated, achieving lasing at 1070 nm. This marks the first reported instance of lasing from a GaAsBi-based VECSEL.

This research was funded by the Research Council of Lithuania (LMTLT), agreement No. [S-MIP-22-86].

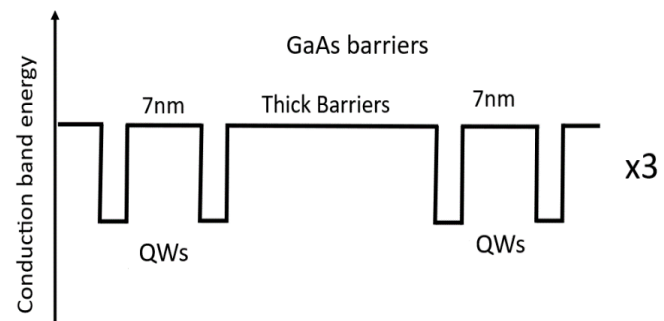


Fig. 1. Sketch of the gain area used in the VECSELs fabrication.

References

- [1] M. Yoshimoto et al., Metastable GaAsBi alloy grown by molecular beam epitaxy, *Jpn. J. Appl. Phys.*, 42 (2003)
- [2] M. Guina, A. Rantamäki, and A. Häkkinen, Optically pumped VECSELs: review of technology and progress, *Journal of Physics D: Applied Physics* **50** (38), 383001 (2017).
- [3] J.-F. Seurin, G. Xu, V. Khalfin, A. Miglo, J.D. Wynn, P. Pradhan, Ch.L.Ghosh, L.A. D'Asaro, Progress in high-power high-efficiency VCSEL arrays, *Vertical-Cavity Surface-Emitting Lasers XIII. Proceedings of SPIE*, **7229**, 722903 (2009).
- [4] Muszalski Jan, et al. "VECSELs emitting at 976nm designed for second harmonic generation in the blue wavelength region." *Laser Technology 2012: Progress in Lasers*. Vol. 8702. SPIE, (2013).
- [5] Jacquemet Mathieu, et al. "Single-frequency cw vertical external cavity surface emitting semiconductor laser at 1003 nm and 501 nm by intracavity frequency doubling." *Applied Physics B* 86 (2007): 503-510.

EVALUATION OF LIMITING FACTORS THAT INFLUENCE THE QUANTUM CUTTING EFFICIENCY OF YTTERBIUM-DOPED HALIDE PEROVSKITE

Lamiaa Abdelrazik,^a Simona Streckaitė,^a Karolina Maleckaitė,
^a Marius Franckevičius^a and Vidmantas Gulbinas^a

^a Center for Physical Sciences and Technology, Department of Molecular Compound Physics
Saulėtekio av. 3, LT-10257 Vilnius, email: lamiaa.abdelrazik@ftmc.lt

Cesium lead halide perovskites (CLHPs) exhibit remarkable properties, including a broad absorption range in the visible light band, tunable bandgap, structure stability, and defect tolerance. Their facile fabrication processes and low production cost make them highly suitable for various optoelectronic applications, such as photovoltaics and photodetection.[1] Recently, CLHPs garnered significant attention as efficient hosts for down-conversion materials, particularly when doped with lanthanide ions such as Yb³⁺. CLHPs can absorb high-energy photons within the UV-blue spectral range and emit two lower-energy photons in the near-infrared region, known as the quantum cutting phenomenon (QC). As a result of this phenomenon, the photoluminescence quantum yield (PLQY) can exceed unity [2,3]. Numerous studies have reported PLQY values under various conditions, reaching 170% [3], 173% [4], and 190% [5]. In our previous work, we achieved a maximum PLQY of 160% for Yb³⁺:CsPbCl₃ powder. However, this value represents a record achievement rather than a consistently reproducible result, as obtaining reproducible films remains challenging [6].

Several factors may limit the achievement of these high PLQY values, including the efficiency of the energy transfer from the perovskite host (Visible spectrum) to the dopant (near-infrared spectrum) or the intrinsic luminescence properties of the dopant. In the present work, we employed electron paramagnetic resonance (EPR) measurements, visible and infrared photoluminescence, ultrafast time-resolved fluorescence, and microscopic techniques to assess ytterbium incorporation into the perovskite lattice and to identify the factors limiting QC efficiency.

Our findings revealed the presence of two distinct species of Yb³⁺ ions—monomeric and dimeric ytterbium—each exhibiting different luminescence lifetimes depending on Yb³⁺ concentration (Fig. 1, Table 1). The fast decay component was found to reduce the luminescence quantum yield less than unity. As the Yb³⁺ concentration increased, this fast decay component diminished, giving way to a dominant slow decay component, which led to an enhancement in PLQY (monoexponential decay). However, with further increases in Yb³⁺ concentration, the slow decay component re-

emerged (non-exponential decay), likely due to migration-limited excitation quenching. This quenching is attributed to several factors, including the presence of impurities, defects, or monomeric Yb³⁺ ions, which leads to non-radiative relaxation.

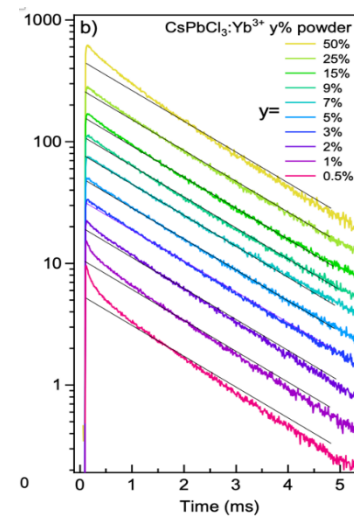


Fig. 1. NIR kinetics of the CsPbCl₃ powders with different Yb³⁺ concentrations.

Table 1. NIR emission decay times of Yb³⁺-doped CsPbCl₃ powders and thin films ($\lambda_{\text{exc}} = 375$ nm).

| | τ_1 [ms] | A ₁ [%] | τ_2 [ms] | A ₂ [%] | τ_{av} [ms] | QY [%] |
|--|---------------|--------------------|---------------|--------------------|-------------------------|--------|
| Powders | | | | | | |
| CsPbCl ₃ :Yb ³⁺ y%, y= | | | | | | |
| 0.5% | 0.15 | 0.52 | 1.46 | 0.48 | 0.79 | 27 |
| 1% | 0.15 | 0.35 | 1.51 | 0.65 | 1.03 | 65 |
| 2% | 0.18 | 0.16 | 1.57 | 0.84 | 1.35 | 81 |
| 3% | 0.64 | 0.11 | 1.71 | 0.89 | 1.59 | 89 |
| 5% | 0.69 | 0.11 | 1.74 | 0.89 | 1.62 | 114 |
| 7% | - | - | 1.67 | 1 | 1.67 | 102 |
| 9% | 0.98 | 0.32 | 1.88 | 0.68 | 1.59 | 101 |
| 15% | 0.73 | 0.24 | 1.80 | 0.76 | 1.55 | 109 |
| 25% | 0.68 | 0.20 | 1.76 | 0.80 | 1.54 | 75 |
| 50% | 0.53 | 0.30 | 1.61 | 0.70 | 1.28 | 71 |

References

1. L. Protesescu, S. Yakunin, *Nano Lett.* 15, 6, 3692–3696 (2015).
2. A. Ishii and T. Miyasaka, *Journal of Chemical Physics*, 153, 194704 (2020).
3. P. Vergeer, T. J. H. Vlugt, M. H. F. Kox, M. I. Den Hertog, J. P. J. M. Van Der Herden and A. Meijerink, *Phys. Rev. B Condens. Ma9er Mater. Phys.*, 71, 014119 (2005).
4. T. J. Milstein, D. M. Kroupa and D. R. Gamelin, *Nano Lett.*, 18, 3792–3799 (2018).
5. D. Zhou, R. Sun, W. Xu, N. Ding, D. Li, X. Chen, G. Pan, X. Bai and H. Song, *Nano Lett.*, 19, 6904–6913 (2019).
6. S. Streckaitė, L. Miklušis, K. Maleckaitė, L. Abdelrazik, M. Franckevičius and V. Gulbinas, *J. Mater. Chem. C*, 11, 15463 (2023).

EVIDENCE OF HOT CARRIER EFFECT IN A SILICON SOLAR CELL

Ihor Zharchenko, Jonas Gradauskas, Oleksandr Masalskyi, Steponas Ašmontas,
Algirdas Sužiedėlis, Aldis Šilėnas, Aurimas Čerškus, Vladyslav Kyshchun

Center for Physical Sciences and Technology, Laboratory of Electronic Processes
Saulėtekio av. 3, LT-10257 Vilnius, email: ihor.zharchenko@ftmc.lt

The sole effective optical mechanism that produces electron-hole pairs essential for solar cell functionality is the absorption of solar photons possessing energy equivalent to a semiconductor's forbidden energy gap. According to the Shockley-Queisser limit, photons with energy below the bandgap are not absorbed [1], leading to what is known as "below-bandgap loss" [2]. Photons with energies exceeding the bandgap create electron-hole pairs with excess energy. Typically, this extra energy is not utilized for carrier generation and instead heats the crystal lattice, diminishing the solar cell's efficiency [3]. This process, termed "thermalization loss," occurs as the carriers lose their excess energy through interactions with other free carriers and phonons.

This study examines the peculiarities of hot carrier (HC) phenomena in solar cells. In an industrial silicon solar cell, the HC photocurrent is generated by radiation which is close to but below the bandgap. The wavelength is chosen to minimize the single-photon generation of electron-hole pairs which could suppress the heating of carriers. Furthermore, the presence of carrier heating under the above-bandgap laser radiation was confirmed. The characteristics of the HC photocurrent are examined by a comparative analysis of the hot carrier and generation photocurrents in their current-voltage (I-V) and current-power dependencies [4]. Additionally, the carrier temperature is determined using an innovative method based on the temperature coefficient of the I-V characteristic [5].

As the investigation reveals, pulsed 1,342 μm laser radiation generates a photocurrent consisting of two components with opposing polarities. The I-V characteristics of the sample, both in the dark and under illumination, are depicted using the individual peak values of each photocurrent component, considering their respective directions, and are illustrated as solid lines in Fig. 1. At the applied laser light intensity of 0.36 MW/cm² both short-circuit photocurrent components have nearly equal values, but increasing the forward bias voltage significantly alters their ratio, reducing the generation component [3].

The formation of the HC photocurrent can be explained as follows: a free electron absorbs energy from the below-bandgap photon, becomes heated, and then diffuses across the junction. This diffusion is driven by the carrier density gradient, with the electron's elevated energy allowing it to overcome the junction's potential barrier. Notably, the direction of this photocurrent aligns with the forward current across the junction [2].

Notably, unlike the generation current (Fig. 1, blue dotted line), no HC short-circuit photocurrent is observed under illumination by a 1.064 μm laser (with photon energy above the bandgap). However, the HC photocurrent becomes noticeable at forward bias voltages above approximately 0.8 V (Fig. 1, red dotted line in the top right corner).

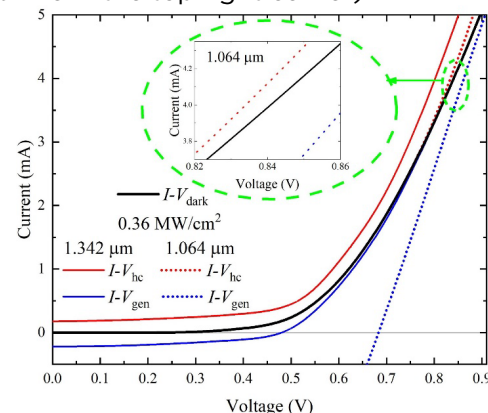


Fig. 1. Current-voltage characteristics of Si solar cell. In the inset: enlarged high-bias region of I-V curves under 1.064 μm illumination.

The I-V curves were measured at temperatures of 300 K and 80 K. The observed shift in the I-V characteristics with temperature can be characterized by the temperature coefficient, a material-specific parameter that indicates the voltage drop per degree of temperature change. The model developed for assessing carrier temperature, based on the temperature coefficient of the I-V characteristics, provides a measure of the hot carrier temperature.

In summary, these findings improve the comprehension of the hot carrier phenomenon in photovoltaic devices and may require a reassessment of intrinsic loss mechanisms in solar cells. Furthermore, the results indicate the need to revise the Shockley-Queisser limit of a single-junction solar cells by incorporating the unavoidable effects of hot carriers.

References

1. W. Shockley, H. J. Queisser, Detailed Balance Limit of Efficiency of p-n Junction Solar Cells, *J. of Appl. Phys.* 32, 510-519 (1961).
2. L. C. Hirst and N. J. Ekins-Daukes, Fundamental losses in solar cells, *Prog. Photovolt. Res. Appl.* 19, 286-293 (2011).
3. J. Gradauskas, S. Ašmontas, A. Sužiedėlis and et al., Influence of Hot Carrier and Thermal Components on Photovoltage Formation across the p-n Junction, *Appl. Sci.* 10, 1-8 (2020).
4. I. Zharchenko, J. Gradauskas, O. Masalskyi, A. Rodin, Hot carrier photocurrent induced by 0.92 eV photon energy radiation in a Si solar cell, *Opto-Electronics Rev.* 32, 1-6 (2024).
5. S. Ašmontas, O. Masalskyi, I. Zharchenko, and et al., Some aspects of hot carrier photocurrent across GaAs p-n Junction, *Inorganics* 12, 1-9 (2024).

SbSel PLONŲ DANGŲ FORMAVIMAS TERMINIU UŽGARINIMU

Deividas Vainauskas, Vidas Pakštas, Rokas Kondrotas

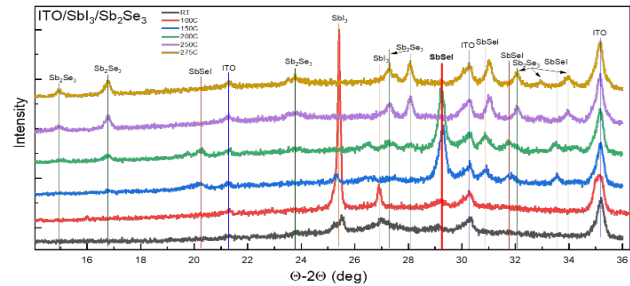
Fizinių ir technologijos mokslų centras, Medžiagų struktūrinės analizės skyrius
Saulėtekio al. 3, LT-10257 Vilnius, el. p.: deividas.vainauskas@ftmc.lt

Stibio seleno jodidas (SbSel) susilaukia vis didėjančio mokslininkų dėmesio fotovoltaikos srityje [1], [2]. SbSel pasižymi dideliu šviesos sugerties koeficientu ir plačiu draustinės juostos tarpu (1.7 eV), todėl šią medžiagą norima pritaikyti kuriant naujos kartos saulės elementus skirtus generuoti energiją iš vidaus patalpų apšvietimo. SbSel taip pat sudarytas iš nebrangių ir mažai toksiškų cheminių elementų bei yra termodinamiškai stabilus kambario salygomis. Tačiau SbSel kristalinę struktūrą sudaro gijos kurios viena kryptimi yra sudariusius stiprius kovalentinius ryšius, o kitomis kryptimis – van der Valsinius. Dėl šios priežasties, kristalizacijos metu SbSel grūdeliai kovalentinių ryšių kryptimi auga labai greitai, o kitomis – lėtai ir tai lemia iš mikro-vamzdelių sudarytą SbSel paviršiaus morfologiją [2]. Tokia sluoksninių morfologija yra netinkama gaminti įprastinės struktūros saulės elementus nes ženkliai padidina paviršinę rekombinaciją, mažina kontaktą plotą ir neužtkrina dangos vientisumo [2]. Taigi pagrindinis šio darbo tikslas buvo išbandyti terminio užgarinimo metodas norint suformuoti kompaktišką ir vientisą SbSel dangą.

Suformuoti plonas SbSel dangas buvo pasirinkti du būdai: (i) atskirtų sluoksninių terminis užgarinimas ir atkaitinimas; (ii) vieno sluoksnio greitas užgarinimas ir atkaitinimas. Pirmuoju atveju, Sb_2Se_3 ir SbI_3 dangos buvo užgarintos viena ant kitos. Buvo nustatyta optimalus garavimo režimas ir laikas kiekvienai medžiagai norint gauti reikiama storio dangas, kurios atitiktų molinį $\text{Sb}: \text{Se}: \text{I}$ santykį 1:1:1 visame tūryje. Tuomet suformuotas dvigubas sluoksnis buvo tiriamas Rentgeno spindulių difrakcijos metodu, kaitinant He atmosferoje in situ režimu. Antruoju būdu ploni sluoksniai buvo auginami garinant SbSel milteliaus specialiaiame lovelioje. Buvo nustatyta ir keičiamas garinimo režimas kuris leistų gauti vientisą, homogenišką Sb-Se-I dangą su stechiometrine sudėtimi.

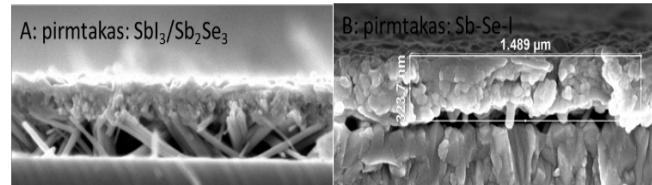
Nustatyta, jog kristalizuojant dangas iš dvigubų pirmtako sluoksninių grynos SbSel fazės formavimosi temperatūrinis intervalas buvo 150 – 200 °C (pav. 1). Fazinė analizė atskleidė, kad bandiniuose atkaitintuose virš 200 °C buvo aptikta Sb_2Se_3 fazė ir jos koncentracija didėjo didinant atkaitinimo temperatūrą. Manoma, jog prie aukštesnių nei 200 °C temperatūrų SbSel skyla į Sb_2Se_3 (kieta) ir SbI_3 (dujos). Šios prielaidos buvo patvirtintos ir termogravimetrijos matavimais. Taigi kaitinant pirmtakus sudarytus iš Sb_2Se_3 ir SbI_3 dangų buvo pasirinktos temperatūros neaukštesnės nei 230 °C. Atlikus paviršiaus morfologijos tyrimus, buvo nustatyta jog visos SbSel dangos suformuotos iš

$\text{SbI}_3/\text{Sb}_2\text{Se}_3$ pirmtako pasižymėjо dviguba dangos struktūra (pav. 2A).



Pav. 1. Dvigubo $\text{SbI}_3/\text{Sb}_2\text{Se}_3$ pirmtako sluoksnio rentgenogramos išmatuotos in situ režimu, kaitinant bandinį iki 275 °C, 50 laipsnių žingsniu, He atmosferoje.

Manoma, kad dėl didelio kristalizacijos temperatūrų skirtumo tarp SbI_3 ir Sb_2Se_3 dangų, SbSel pirmiausia pradeda formuotis apatinėje sluoksnio dalyje, o perteklinis jodas pasišalina duju pavidale. Šios priežastys lėmė tuščumų susiformavimą prie padéklo ir suteikė erdvės mikro-vamzdelių augimui (pav. 2A). Deja, dėl mažo sukibimo ploto dangos dažnai atšokdavo nuo padéklo.



Pav. 2. Atkaitintų SbSel dangų skerpjūvio SEM nuotraukos, kai (a) pirmtakas buvo dvigubas sluoksnis (b) viengubas.

Norint išvengti dvigubo sluoksnio formavimosi, buvo nuspresta pakeisti pirmtako nusodinimo būdą ir pabandyti užauginti Sb-Se-I sluoksnį tiesiogiai. Šiam tikslui pasiekti buvo pasitelktas greito garinimo metodas, nes kaip nustatyta anksčiau, įprastiniu greičiu kaitinant SbSel milteliai skyla į Sb_2Se_3 ir SbI_3 . Garinimo procesas buvo optimizuojamas keičiant garinimo greitį, atstumą tarp padéklo ir šaltinio, miltelių kiekį bei lovelio formą. Po kristalizacijos, dangos buvo kompaktios, grynos SbSel fazės ir nepasižymėjо dvigubo sluoksnio struktūra (pav. 2B). Taigi šiame darbe pavyko rasti terminio garinimo sąlygas norint gauti vientisas, kompaktiškas ir pakankamai lygias SbSel dangas.

Literatūra:

1. Sadurni, Marc Dolcet, et al. "Preparation and characterization of SbSel thin films." *Journal of Science: Advanced Materials and Devices* 9.1 (2024): 100664.
2. Nowak, M., et al. "Optical properties of nanocomposite fibrous polymer mats containing SbSel nanowires." *Optical Materials* 84 (2018): 383-388.

INVESTIGATION OF PHOTOVOLTAGE FORMATION IN PEROVSKITE SOLAR CELLS

Mujahid Muhammad

Center for Physical Sciences and Technology, Laboratory of Electronic Processes
Saulėtekio av. 3, LT-10257 Vilnius, email: muhammad.muhammad@ftmc.lt

Due to their outstanding characteristics that have the potential to be used in optoelectronic devices including solar cells, photodetectors, and light-emitting diodes, metal halide perovskites have caught a lot of attention. Because of its high absorption coefficient over the whole visible spectrum, which enables the use of thin films, high defect tolerance, high carrier mobility, and long carrier diffusion length, metal halide perovskites are appealing for use in solar cells[1].

In this project I will present experimental as well as theoretical study of the formation of photovoltaic voltage in perovskite solar cells fabricated with and without Sn on base cesium-containing triple cation perovskite film $Cs_x(FA_{0.83}MA_{0.17})_{(1-x)}Pb(I_{0.83}Br_{0.17})_3$ and $Cs_x(FA_{0.83}MA_{0.17})_{(1-x)}Pb_{0.8}Sn_{0.2}(I_{0.83}Br_{0.17})_3$.

Two components constitute up the photoresponse, according to measurements of transient photovoltaic voltage created in perovskite solar cells by short laser pulse illumination. The photovoltaic voltage was determined to consist of two components: $U = Uph + Uf$ [2]. The first one, Uph , is the typical photovoltaic result of laser radiation producing electron-hole pairs. The second one, Uf , is the rapid component of photovoltaic voltage that has the opposite polarity from Uph and follows the laser pulse. Compared to Pb perovskite solar cells, mixed Pb-Sn perovskite solar cells typically have a lower photovoltaic.

Conference abstracts submitted by October 1 2024.

References

1. Ašmontas, S.; Mujahid, M. Nanomaterials. **13**, 1886 (2023).
2. S.Ašmontas, J.Gradauskas, A.Sužiedelis et al., Appl.Phys.Lett. **113** p 071103 (2018).

PROPERTIES OF PLANAR AND MESOPOROUS PEROVSKITE SOLAR CELLS

Kazimieras Petrauskas, Steponas Ašmontas, Aurimas Čerškus,
 Jonas Gradauskas, Asta Grigucevičienė, Remigijus Juškėnas, Konstantinas Leinartas,
 Andžej Lučun, Algirdas Selskis, Laurynas Staišiūnas, Algirdas Sužiedėlis,
 Aldis Šilėnas, Edmundas Širmulis

Center for Physical Sciences and Technology, Laboratory of Electronic Processes
 Saulėtekio av. 3, LT-10257 Vilnius, email: kazimieras.petrauskas@ftmc.lt

Perovskite solar cells (PSCs) have garnered considerable attention in recent years due to their notable efficiency and potential for cost-effectiveness. Featuring a hybrid organic-inorganic composition, these materials have demonstrated significant advancements in power conversion efficiency (PCE), positioning them as promising candidates for renewable energy applications. Understanding the various factors influencing PSC performance is essential for enhancing their commercial viability.

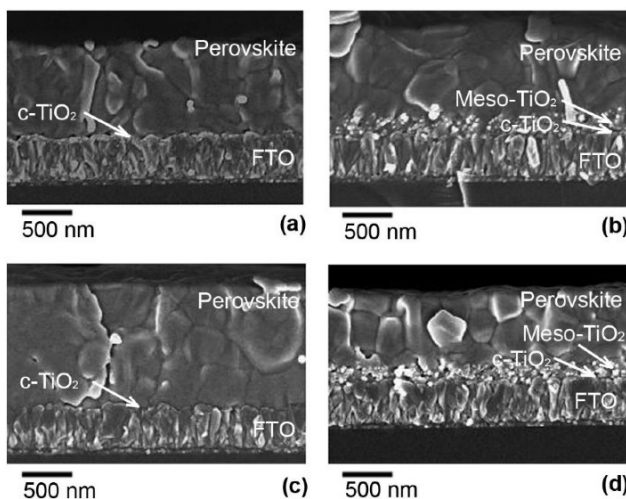


Fig. 1. Cross-sectional SEM images of perovskite films on different TiO_2 layers [1].

The analysis included four distinct types of perovskite films: Film A (on compact TiO_2), Film B (on mesoporous TiO_2), Film C (on compact ALD- TiO_2), and Film D (on mesoporous ALD- TiO_2). Various characterization techniques, such as X-ray diffraction (XRD), scanning electron microscopy (SEM), and photoluminescence (PL) measurements, were employed. XRD analysis revealed that films grown on mesoporous TiO_2 exhibited superior crystallinity compared to

those on compact TiO_2 , with sharper peaks indicating larger crystallite sizes and reduced dislocation densities. SEM imaging provided insights into the morphology, showing that films on mesoporous layers penetrated more effectively between nanocrystals, resulting in smoother surfaces and uniform grain distribution. Photoluminescence studies indicated a significantly longer lifetime of charge carriers in mesoporous structured films, correlating with enhanced device performance.

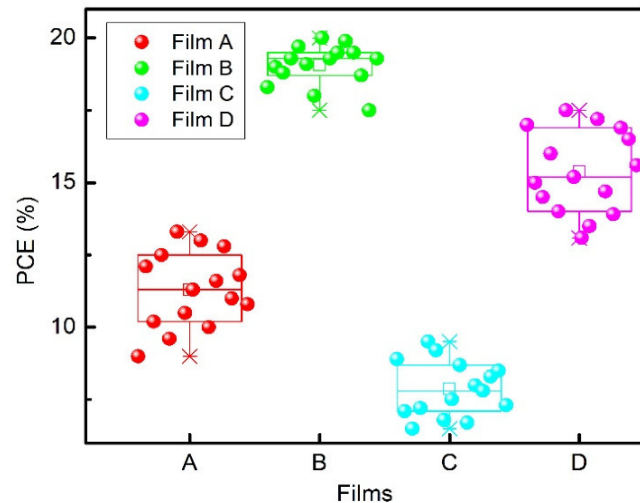


Fig. 2. Statistical distribution of the power-conversion efficiency of perovskite solar cells based on different perovskite films.

Overall, these findings demonstrate that mesoporous structures facilitate improved charge transport and longer carrier lifetimes, contributing to higher power conversion efficiencies in solar cells.

References

1. Ašmontas, S.; Čerškus, A.; Gradauskas, J.; Grigucevičienė, A.; Juškėnas, R.; Leinartas, K.; Lučun, A.; Petrauskas, K.; Selskis, A.; Staišiūnas, L.; et al. *Materials* **2022**, *15*, 4300.

INNOVATIVE BIMETALLIC 3D NICKEL-IRON/TITANIUM BIFUNCTIONAL ELECTROCATALYSTS FOR EFFICIENT HYDROGEN EVOLUTION REACTION IN ACIDIC MEDIA

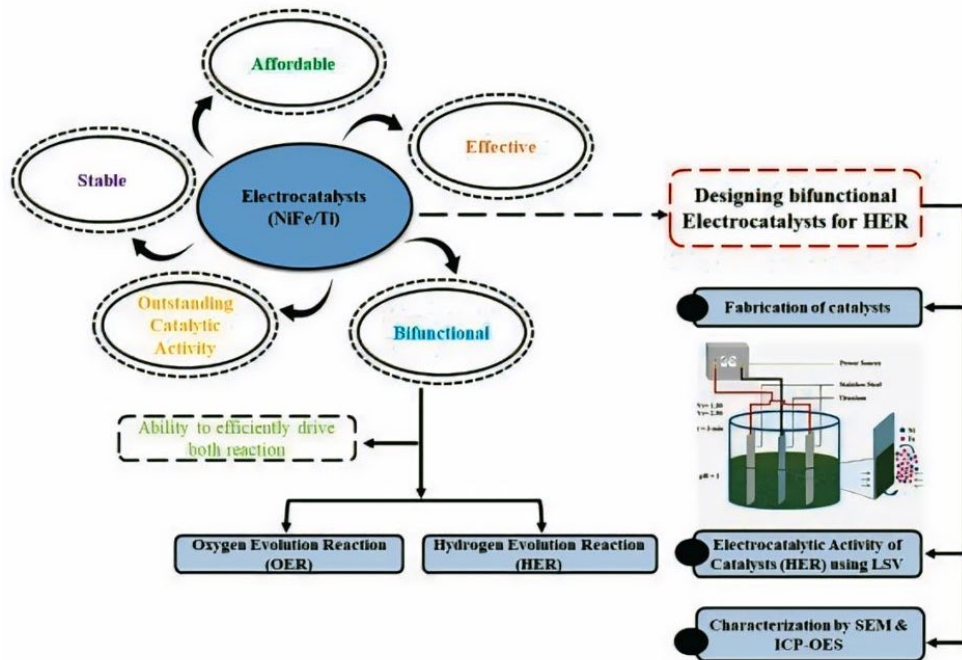
Shahid Nawaz, Aldona Balčiūnaitė

Department of Catalysis, Center for Physical Sciences and Technology, Saulėtekio av. 3, LT-10257 Vilnius,
email: shahid.nawaz@ftmc.lt

Due to their significance in science and technology, the development of affordable, efficient, and robust hydrogen evolution reaction (HER) electrocatalysts has been a long-standing pursuit. The demand for bifunctional electrocatalysts, capable of efficiently driving both the oxygen evolution reaction (OER) and hydrogen evolution reaction (HER), is gaining considerable attention, as they are essential for overall water-splitting processes. However, designing OER/HER bifunctional electrocatalysts that are both cost-effective and exhibit outstanding catalytic activity remains a significant challenge. In this study, iron-nickel (Fe/Ni) bimetallic coatings were investigated as electrocatalysts for the HER in acidic (0.5 M H₂SO₄) media. The catalysts were deposited on a titanium substrate (1 × 1 cm²) using an economical and straightforward electrochemical deposition process via a dynamic hydrogen bubble template method. The electrocatalytic

efficiency of the synthesized catalysts was evaluated for HER at 25°C using linear sweep voltammetry (LSV). The surface morphology and composition were further analyzed through scanning electron microscopy (SEM) and inductively coupled plasma optical emission spectroscopy (ICP-OES). It was observed that the synthesized FeNi/Ti-1 and FeNi-2 electrocatalysts, with Fe³⁺/Ni²⁺ molar ratios of 1:1 and 1:2, respectively, exhibited excellent HER activity in acidic conditions, requiring an overpotential of 106 mV to achieve a current density of 10 mA cm⁻². Both catalysts demonstrated outstanding long-term stability for two and ten hours at constant potentials and a constant current density of 10 mA cm⁻², indicating their resilience and enhanced stability.

Graphical Abstract:



ELECTROSTATIC INTERACTIONS IN PHOTOSYNTHETIC COMPLEXES

Gabrielė Rankelytė^{1,2}, Jevgenij Chmeliov^{1,2}, Andrius Gelzinis^{1,2}, Leonas Valkunas^{1,2}

¹Center for Physical Sciences and Technology, Department of Molecular Compound Physics
Saulėtekio av. 3, LT-10257 Vilnius, email: gabriele.rankelyte@ftmc.lt

²Institute of Chemical Physics, Faculty of Physics, Vilnius University
Saulėtekio av. 9, III bld., LT-10257 Vilnius

Photosynthesis is one of the most important processes on Earth. The most efficient organisms that carry out photosynthesis are land plants or higher plants. In the thylakoid membrane of chloroplasts there are two systems that carry out photosynthesis - Photosystem I (PSI) and Photosystem II (PSII), both with their own light harvesting complexes - LHCI and LHCII.

PSI is the most efficient light-to-energy conversion apparatus with quantum yield almost equal to 1 [1]. One of the conditions needed for high efficiency is very fast energy transfer between the molecules in light harvesting complex (LHCI). Light-harvesting complex of PSI absorbs and emits light at the longest wavelengths compared to other pigment-protein complexes. In plants, light harvesting antenna of PSI is composed of four species of LHCI complexes. They all have very similar structure; however, their spectral properties are different.

The excitation dynamics in LHCI is highly affected by the charge-transfer (CT) states that occur between two or more pigments [2]. Some sites in which CT states occur in LHCI are known; however, they do not completely explain the spectral properties of this antenna, such as the red-shifted peak in fluorescence spectrum. The energy of the excited states of pigments (including the CT states) are highly affected by the surrounding environment, consisting of other pigments (chlorophylls and carotenoids) and the protein chain. Therefore, it is necessary to account for the environment to model light-harvesting complexes properly.

LHCI structure was obtained as the 1st-4th chains of PSI complex structure [3] (see Fig. 1), freely available at Protein Data Bank (PDB ID: 5L8R). We calculated the distances between the chlorophyll molecules (Mg-Mg distance) in Lhca1-4 complexes and selected chlorophyll pairs that are no further than 12.5 Å. The possible charge-transfer states in all four Lhca complexes were found by evaluating the distribution of Mulliken partial charges between the pigments of the dimers as well as the values of static and transfer dipole moments of the dimers. We then performed quantum chemical calculations to obtain energies of these chlorophyll dimer CT states *in vacuo* using "VU HPC Saulėtekis" supercomputer.

The dimers of interest were then surrounded by the environment once again. For all four protein chains, we estimated the most probable

protonation pattern in neutral solution using Henderson-Hasselbalch equation. We then included the environment (chlorophylls, carotenoids and the protein chain) in our calculations by obtaining atomic partial charges of both environmental blocks and the dimers of interest and evaluating the electrostatic interaction between these charges using CDC (charge-density coupling) method [4]:

$$\Delta E_m = \frac{1}{\epsilon_{\text{eff}}} \sum_I \sum_{\eta, J} \frac{(q_I^{(m)}(s,s) - q_I^{(m)}(0,0)) q_J^{(\eta)}(0,0)}{|R_I^{(m)} - R_J^{(\eta)}|}. \quad (1)$$

Here ϵ_{eff} denotes the effective dielectric constant of the environment, m is the index for the dimer of interest and $q_I^{(m)}(s,s)$ ir $q_I^{(m)}(0,0)$ are the partial charges of this dimer in the excited and the ground state, respectively. $q_J^{(\eta)}(0,0)$ denotes the partial charges of the remaining pigments and the amino acids surrounding this dimer. $R_I^{(m)}$ and $R_J^{(\eta)}$ denote the coordinates of the charges of the dimer of interest and the environmental blocks, respectively.

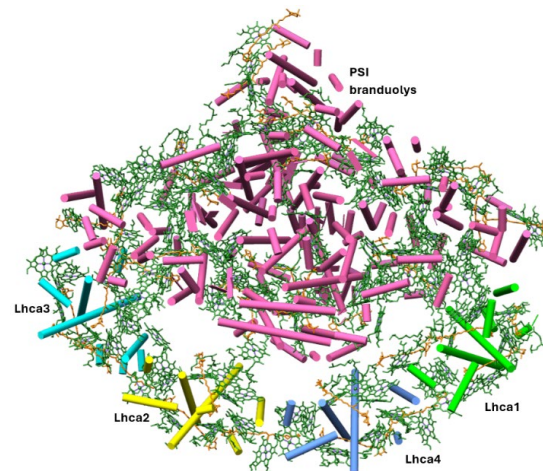


Fig. 1. The structure of Photosystem I (PDB ID: 5L8R). The protein chain is depicted in various colors, representing PSI core and four light harvesting complexes Lhca1-4. Chlorophyll molecules are depicted in green and carotenoids - in orange.

References

1. R. Croce, H. van Amerongen, *Photosynth. Res.* **116**, 153-166 (2013).
2. M. Tros, V. I. Novoderezhkin, R. Croce, R. van Grondelle, and E. Romero, *Phys. Chem. Chem. Phys.* **22**, 25720-25729 (2020).
3. Y. Mazor, A. Borovikova, I. Caspy, N. Nelson, *Nat. Plants*, **3**, 17014-17014 (2017).
4. T. Renger, F. Mühl, *Phys. Chem. Chem. Phys.* **15**, 3348-3371 (2013).

HIBRIDINIŲ MIKROGUMBELIŲ GARDELIŲ DYDŽIO ĮTAKA PLAZMONŲ REZONANSO SUŽADINIMO KOKYBEI

Rodrigas Liudvinavičius, Evaldas Stankevičius

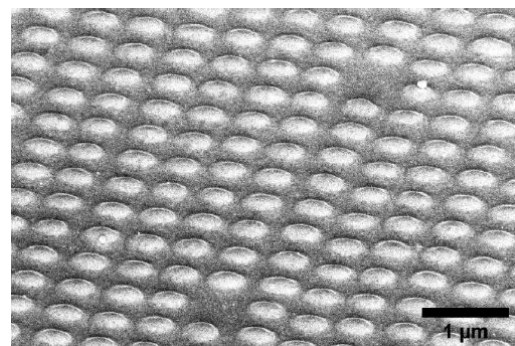
Fizinių ir technologijos mokslų centras, Lazerinių technologijų skyrius
Savanorių per. 231, LT-02300 Vilnius, el. p.: rodrigas.liudvinavicius@ftmc.lt

Pastaraisiais metais nanotechnologijų sritis sulaukia vis daugiau dėmesio dėl sėkmingo nanostruktūrų taikymo jutiklių gamyboje ir naujų optinių prietaisų kūrime [1]. Tarp sėkmingų nanoprietaisų svarbų vaidmenį atlieka metalo nanostruktūros, ypač pagamintos iš tauriųjų metalų, pavyzdžiui, aukso ar sidabro. Šios medžiagos išsiskiria bei pasižymi unikaliomis ir stipriomis plazmoninėmis savybėmis, apibūdinančiomis šviesos ir nanostruktūrų sąveiką.

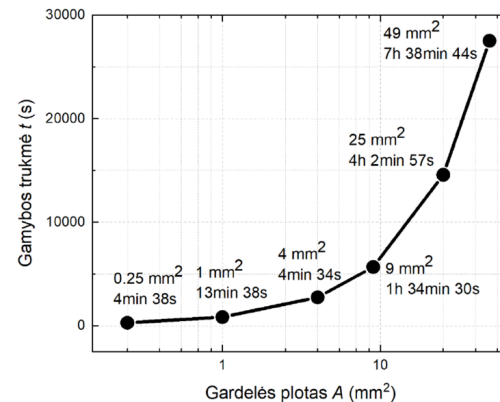
Plazmoninės nanostruktūros dažnai gaminamos naudojant elektronų pluošto (e-beam) ir fokusuoto jonų pluošto (FIB) litografijos metodais. Tačiau šie būdai turi trūkumų, susijusių su periodiškumo skiriamaja geba ir gamybos sąnaudomis. Naujausi pasiekimai lazerinio apdirbimo srityje, pavyzdžiui tiesioginiame lazeriniame rašyme (TLR) yra nauja alternatyva litografiniams metodams. Naudojant TLR, galima tiesiai ant plonų metalinių paviršių formuoti skirtinges struktūras. Šis metodas pasižymi ir tuo, jog yra ekonomiškas ir suteikia galimybę tiesiogiai valdyti struktūros parametrus. Šiame tyrime mikrogumbelių formavimo procesas buvo atliktas naudojant TLR, tuo pat metu remiantis pačios medžiagos, aukso tamprumo ir takumo savybėmis.

Nepaisant tiesioginio lazerinio rašymo privalumų, visgi kyla sunkumų paseikiant stiprų optinį atsaką, nulemta rezonanso sugerties dėl plazmonų modų hibridizacijos efekto. Tyrime yra aptariami optinio plazmonų atsako gerinimo būdai, pavyzdžiui periodo tarp mikrostruktūrų mažinimas bei periodinės gardelės masyvo didinimas. Taip pat, matavimo pluoštą ribojančių apertūrų pasitelkimas, norint efektyviau išmatuoti struktūruoto aukso paviršiaus plotą. Atsirandant keliems gamybos proceso ir matavimo kintamiesiems, atsiranda ir poreikis optimizuoti visą formavimo procesą. Tokiu būdu išlaikant geriausią santykį tarp darinių masyvo formavimo laiko ir optinio rezonanso sugerties signalo.

Šiame darbe yra aptariami mikrogumbelių masyvo dydžio įtaka plazmoninio sužadinimo kokybės parametrams (Q ir MQ kokybės parametrai). Tyrimas taip pat apima ir suformuotų gardelių įvertinimo proceso patobulinimus, pateikiami būdai kaip efektyviau yra įvertinama plazmoninių gardelių optinis atsakas – rezonanso sugertis. Tai yra atliekama, panaudojant papildomas apertūras, skirtingo dydžio ir formos, ribojančias matavimo pluošto dydį.



1 pav. Aukso mikrogumbelių plonoje 50 nm dangajo SEM nuotrauka. Periodas tarp darinių 550 nm. Mikrostruktūros buvo suformuotos naudojant 0,6 nJ energijos lazerio impulsą.



2 pav. Aukso mikrogumbelių gardelės gamybos trukmės priklausomybė nuo gardelės ploto.

Literatūra

1. K. Yang, et al., Metallic Plasmonic Array Structures: Principles, Fabrications, Properties, and Applications. Adv. Mater. 33(50), pp. 2007988 (2021).

Padėka

Finansavimą skyrė Lietuvos mokslo taryba (LMTLT), sutarties Nr. S-MIP-23-32.

POLYMER-BASED METALENSES FOR THz BEAM ENGINEERING

Simonas Driukas¹, Rusne Ivaškevičiūtė-Povilauskienė¹, Vladislovas Čižas¹, Karolis Redeckas¹, Linas Labanauskas², Vytautas Jakštė¹, Linas Minkevičius¹ and Gintaras Valušis¹

¹Departament of Optoelectronics, Center for Physical Sciences and Technology,

²Departament of Organic Chemistry, Center for Physical Sciences and Technology,
Saulėtekio Ave. 3, Vilnius, Lithuania.

Email: simonas.driukas@ftmc.lt

The rapid development of terahertz (THz) technology and its promising implementations in communications, security and other industries stimulates high demand for compact photonic components. Since conventional passive optics are bulky and severely limit the packaging options for photonic circuits, THz metamaterials-based photonics has attracted considerable attention. One of attractive options are metlenses, which are flat and flexible compared to conventional lenses and allow compact photonic integration into various optical devices and circuits. Generally, such metlenses are fabricated from highly conductive metallic materials to couple the THz field to the meta-surface cells.

In this work, we explore an alternative approach by using conductive polymers as the base material for the fabrication of metlenses. This brings several key advantages as polymers can be processed using solution-based methods and require lower laser patterning energies, which is particularly beneficial when depositing metlenses on sensitive substrates.

Three different polymers - Clevios™ SV3, Clevios™ PH1000 and FET3 - were selected for metlens fabrication and designed for frequency of 300 GHz. For comparison, samples made from

metal and graphite are studied. Beam shaping and spectral properties were investigated. Measurements show a good focusing and rather strong conductivity-dependent performance of the photonic components.

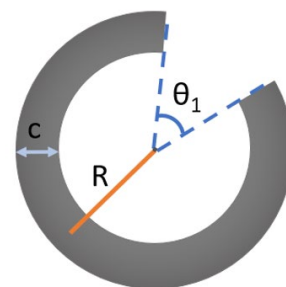
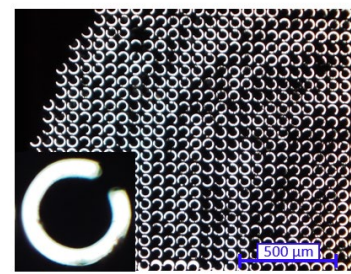


Fig. 1. Microscopic image of polymer metlens and its schematic design parameters.

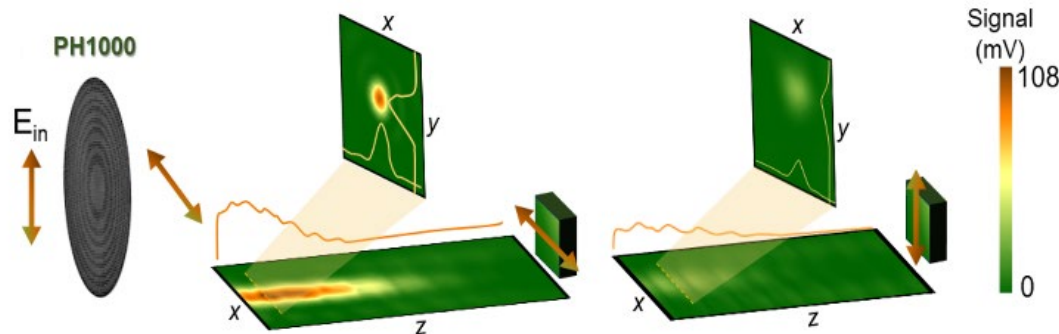


Fig. 2. Spatial beam distribution of the focused THz radiation using metlens based on PH1000.

UNRAVELING THE IMPACT OF BIOMASS BURNING THROUGH ISOTOPIC COMPOSITION

D. N. Habib, A. Garbaras and A. Mašalaitė

Center for Physical Sciences and Technology, Department of Nuclear Research
Saulėtekio av. 3, LT-10257 Vilnius, email: durre.nayab@ftmc.lt

Biomass burning aerosols are significant source of atmospheric aerosols, releasing a diverse mixture of particles and gases into the atmosphere [1]. The impacts of biomass burning aerosols extend beyond local and regional scales, as they can be transported over long distances by atmospheric circulation, affecting air quality and climate in remote regions [2]. This work provides the analysis of aerosols produced from a range of biomass fuels (17 types of wood) and coal, focusing on their isotopic signatures of total carbon, elemental carbon, and organic carbon at various temperature stages. The design of experiment was crafted to closely replicate normal conditions, aligning with the typical heating practices observed during winter in domestic settings in Lithuania. The results demonstrate a broad distribution of isotopic signatures of the carbon isotopes ($\delta^{13}\text{C}$) across different plant species used for biomass burning (BB) experiment. The isotopic variability at lower temperatures is exhibiting greater diversity compared to those at higher temperatures (350 °C and 650 °C). The analysis highlights distinct isotopic signatures between C₃ and C₄ plants, with C₄ corn displaying less negative $\delta^{13}\text{C}$ values (~-12‰), while C₃ species like willow and oak showing more negative values (-29‰ to -31‰). The elemental carbon (EC) consistently shows more negative $\delta^{13}\text{C}$ values comparing to TC across most species, indicating isotopic fractionation during its formation. Furthermore, the fractionation factor (ε) analysis highlights that while most species

show ε values clustering around zero, indicating minimal fractionation between biomass burning materials and aerosol particles, coal exhibits unique isotopic behavior with higher positive ε values. The overall isotopic composition revealed the differences between BB material indicating that different plants and coal possess distinct isotopic signatures. During this study, we aim to enhance our understanding of biomass burning aerosols and their broader environmental implications.

References

1. Souri, A., et al. (2023). The impact of biomass burning emissions on aerosol concentrations and depositions in the northern South China Sea region. *Frontiers in Environmental Science*, 11, 1124579.
2. Zhang, Y., et al. (2023). Impacts of biomass burning in Southeast Asia on aerosols over downwind regions: A case study during the spring season. *Frontiers in Environmental Science*, 11, 1101745.

MAŠININIS MOKYMASIS – POTENCIALUS ĮRANKIS ANTENŲ MODELIAVIME

Justina Žemgulytė, Paulius Ragulis, Žilvinas Kancleris

Fizinių ir technologijos mokslų centras, Fizikinių technologijų skyrius
Saulėtekio al. 3, LT-10257 Vilnius, el. p.: justina.zemgulyte@ftmc.lt

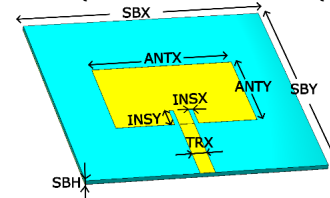
Mašininis mokymasis šiandien yra viena iš populiausių ir sparčiai besivystančių technologijų, turinčių didelį poveikį įvairioms pramonės šakoms ir kasdieniam gyvenimui. Mokslineje literatūroje daugėja darbų, kurie parodo, kad mašininis mokymas gali būti panaudotas įvairių procesų optimizavimui, kaip sudėtingų kompozitų liejimas [1], jutiklių duomenų apdorojimas [2] ir pan.

Populiariausia antenų elektromagnetinio modeliavimo metodika yra pagrįsta baigtinių skirtumų laiko skalėje (angl. *Finite-Difference Time-Domain*) metodu. Pagrindinė šios metodikos idėja yra spręsti diskretizuotas Maksvelo lygtis erdvėje ir laike. Antena ir erdvė aplink ją yra padalinama į celes ir jose skaičiuojamas elektromagnetinio lauko dedamosios. Diferencijuoto Gauso formos žadinimo signalas sklinda tiriamoje erdvėje ir sąveikauja su antena. Žinodami elektromagnetinio lauko kitimą antenoje ir aplink ją galime suskaičiuoti kokia dalis energijos buvo sugerta, išspinduliota, kokia dalis atsispindėjo ir sugrįžo atgal į žadinimo šaltinį. Šis procesas naudoja didelius skaičiavimo resursus, o kad išsamiai išnagrinėti anteną reikia ne tik žinoti jos elektromagnetinių parametrų dažnines charakteristikas bet ir jų priklausomybes nuo antenos geometrinių parametru. Atliekant daug modeliavimų net ir nepriekaištingai apdorojant duomenis yra sunku atskirti ir apibrėžti kokią įtaką konkretus parametras turi antenos veikimui. Taip pat nėra lengva optimizuoti anteną, kai pasikeičia poreikiai, pavyzdžiui, reikia panaudoti kitą medžiagą su kita dielektrine skvarba, arba, reikia, kad antena veiktu kitame dažnyje. Šias problemas gali padėti išspręsti mašininis mokymas.

Šiame darbe parodėme, kad turint pakankamą kiekį modeliavimo duomenų, galime taikyti dirbtinio intelekto (DI) metodus, konkrečiai mašininį mokymąsi, kad įvertintume antenos geometrinių parametrų įtaką jos veikimui. Tam tikslui duomenis sugrupuojame į ypatybes ir tikslines vertes (angl. *features and target values*). Ypatybės gali būti antenos geometriniai parametrai (1 pav.), o tikslinės vertės – elektromagnetinės charakteristikos: antenos rezonansinis dažnis, atspindžio koeficientas ir stiprinimas. Darbe parodysime, kad apmokę modelį galėsime padaryti išvadas apie geometrinių parametrų įtaką apsibrėžtoms tikslinėms vertėms.

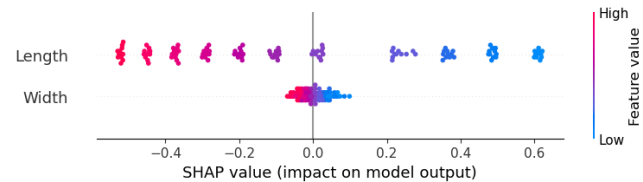
Šiam tikslui buvo surinkti 121 mikrojuostelinės antenos atspindžio koeficiente priklausomybės nuo dažnio, kur buvo keičiamas tik antenos ilgis ir plotis nuo 20 mm iki 30 mm. Panaudojant šiuos duomenis buvo apmokytas DI algoritmas Random Forest Regressor. Naudojant įrankį SHAP (angl.

SHapley Additive exPlanations) atvaizdavome kokią įtaką antenos ilgis ir plotis daro antenos rezonansiniams dažniui, rezonanso gyliui bei stiprinimui (2 pav.). Spalva žymi geometrinio parametru dydį, o padėtis rodo, ar pasirinkta tikslinė vertė didėja, ar mažėja. Sukurtas modelis gali ne tik pateikti šias įžvalgas, bet ir suprojektuoti anteną, kuri veiktu norimame dažniu ruože.

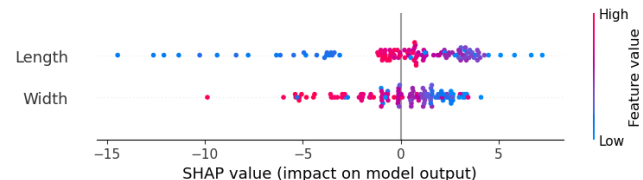


1 pav. Galimos mikrojuostelinės antenos ypatybės arba geometriniai parametrai.

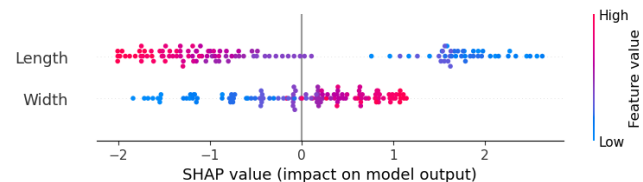
a)



b)



c)



2 pav. Antenos ilgio ir pločio įtaka mašininio mokymo algoritmui (SHAP įrankis), a – rezonansiniams dažniui, b – atspindžio koeficientui, c – stiprinimui.

Mašininis mokymas turi potencialą palengvinti antenų modeliavimą, bei suteikti įrankių patogiam modeliavimo rezultatų apibendrinimui. Šio darbo metu buvo siekiama palyginti kelis algoritmus, patikrinti sukurto modelio patikimumą, bei įtraukti kitus antenos geometrinius parametrus.

Literatūra

- [1] H. Tercan, A. Guajardo, J. Heinisch, T. Thiele, C. Hopmann, and T. Meisen, ‘Transfer-Learning: Bridging the Gap between Real and Simulation Data for Machine Learning in Injection Molding’, *Procedia CIRP*, vol. 72, pp. 185–190, 2018, doi: 10.1016/j.procir.2018.03.087.
- [2] A. Fischer, M. Liang, V. Orschlet, H. Bi, S. Kessler, and J. Fottner, ‘Detecting Equipment Activities by Using Machine Learning Algorithms’, *IFAC-Pap.*, vol. 54, no. 1, pp. 799–804, 2021, doi: 10.1016/j.ifacol.2021.08.094.

SELF-ASSEMBLED MONOLAYERS FOR ELECTRODE SURFACE COATING: FORMATION AND EVALUATION

Simona Raišytė¹, Viktorija Liustrovaitė², Arūnas Ramanavičius^{1,2}

¹Center for Physical Sciences and Technology, Department of Nanotechnology,
Saulėtekio av. 3, LT-10257 Vilnius, email: simona.raisyte@ftmc.lt

²Vilnius University, Faculty of Chemistry and Geosciences, Institute of Chemistry,
Department of Physical Chemistry, Naugarduko Str. 24, LT-03225 Vilnius

Biosensors are analytical devices designed to convert biological reactions occurring within living organisms into measurable electrical signals such as resistance, current, and electrical conductivity [1]. Their wide application comes from their capability to perform rapid measurements and detect analyte concentrations as low as nanomolar levels. [2]. This sensitivity makes them indispensable tools in fields such as medical diagnostics, environmental monitoring, and food safety. The initial step in developing biosensors involves modifying the surface of the working electrode, which significantly impacts sensor performance. Among various techniques, the formation of a self-assembled monolayer (SAM) on the electrode surface is employed due to its performance and structure, affecting the application and use of the biosensor.

In this study, the screen-printed electrode (SPE) was modified in two stages to optimise its electrochemical properties for biosensing applications. Initially, a thin layer of gold nanostructures (AuNS) was deposited on the SPE surface. Subsequently, SAMs of different compositions were formed on the AuNS-modified SPE electrode surface.

The impact of the SAM formation and its constituent molecules on the electrochemical properties of the AuNS-coated SPE electrode was evaluated using square wave voltammetry (SWV) and electrochemical impedance spectroscopy (EIS).

The successful formation of the SAM was verified by an increase in charge transfer resistance and a decrease in current density, compared to the results observed when the working electrode surface was coated only with AuNS.

These changes suggest the potential of this modified electrochemical system as a robust platform for biosensor development, offering increased sensitivity, adaptability, and potential for integration into real-world diagnostic tools. Future work could focus on optimising the SAM composition for specific biomolecular targets, enabling the development of highly specific and versatile biosensors for various clinical and environmental applications.

References

1. Liustrovaite, V. et al. (2023). Towards Electrochemical Sensor Based on Molecularly Imprinted Polypyrrole for the Detection of Bacteria—Listeria monocytogenes. *Polymers*, 15(7).
2. Liustrovaite, V et al. (2024). Electrochemical biosensor for the evaluation of monoclonal antibodies targeting the N protein of SARS-CoV-2 virus. *Science of the Total Environment*, 924.
3. Drobyshev, M. et al. (2024). Electrochemical biosensing based comparative study of monoclonal antibodies against SARS-CoV-2 nucleocapsid protein. *Science of the Total Environment*, 908.

REMOVAL OF LEAD (II) FROM AQUEOUS SOLUTION BY BUCKWHEAT (*FAGOPYRUM ESCULENTUM*) HULL AS A LOW-COST BIOSORBENT: KINETIC, EQUILIBRIUM AND THERMODYNAMIC STUDIES

Tayyab Tahir¹, Rūta Druteikienė¹, Zita Žukauskaitė¹, Jūratė Vaičiūnienė²

¹Center for Physical Sciences and Technology, Department of Nuclear Research
Savanorių ave. 231, LT-02300 Vilnius, email: tayyab.tahir@ftmc.lt

²Center for Physical Sciences and Technology, Department of Catalysis
Saulėtekio av. 3, LT-10257 Vilnius

Water is the main constituent of the hydrosphere as well as a basic component in all life forms (e.g.: plants, microorganisms, animals, fishes, and humans) for food and nutrient transportation and thermoregulation across their bodies. In industries, water is also used for processing, diluting products, temperature regulation, cleaning, and various other purposes. Wastewater from petroleum, metal refinery, paint, chemical plants, textiles, and steel industries contains heavy metals such as Cu²⁺, Ni²⁺, Zn²⁺, Pb²⁺, Hg²⁺ and Cr³⁺. The exposure of this contaminated wastewater to the environment is a major cause of water pollution as these heavy metals have hazardous effects on all life forms making it a big concern for environmentalists [1].

Consumption of lead (II) even in small amounts leads to severe diseases such as anaemia, hepatitis, and encephalopathy. It also can cause central nervous system disorder and irreversible brain damage. Furthermore, long-term exposure to Pb(II) affects human hearing, learning ability, growth, and central nervous system of children [2].

Filtration, precipitation, carbon adsorption, ion exchange, evaporation, electrochemical processes redox, electrowinning, reverse osmosis pre-concentration, chelation, membrane technology, and wastewater coagulation are few examples of wastewater cleaning methods [3]. Nowadays a promising technique called as biosorption, a process involving treatment of effluents for removal of heavy metals, is a highly sensitive technique. Being more efficient this technique provides various benefits than conventional techniques as it requires minimal technical expertise, cost-effective, and also produces less biological /chemical sludge [4].

This research aims to evaluate the effectiveness of buckwheat (*Fagopyrum esculentum*) hull as a cost- effective biosorbent for the removal of lead (II) from aqueous solutions. The objectives include studying the adsorption kinetics, equilibrium isotherms along with thermodynamic parameters to understand the mechanism and feasibility of the process.

Buckwheat hull was characterized by determining their physicochemical properties using analytical methods such as FTIR, SEM, EDX, and pH of zero-point charge.

The pH_{pzc} value for buckwheat hull is around 5.4, which indicates that surface of buckwheat hull has positive charge at below pH value of 5.4 and have negative charge above pH value of 5.4. Due to repulsive electrostatic interactions between lead (II) and the positively charged surface of buckwheat hull below pH value of 5.4, biosorption of lead (II) is unfavorable. The maximum lead (II) adsorption by buckwheat hulls was 96.7% at pH 6, contact time for 180 min, the initial lead concentration of 50 mg/L, the temperature of 25 °C, and biosorbent dose of 0.1 g.

The equilibrium study shows a high value of the regression correlation coefficient ($R^2 = 0.95$) for the Langmuir model, which is the best fit for the biosorption of Pb (II) in buckwheat hull with a sorption capacity of 96.15 mg g⁻¹. The adsorption of lead (II) presented a pseudo-second-order kinetics and the study of thermodynamic parameters discovered that the lead (II) adsorption on buckwheat hull is a non-spontaneous and exothermic process.

References

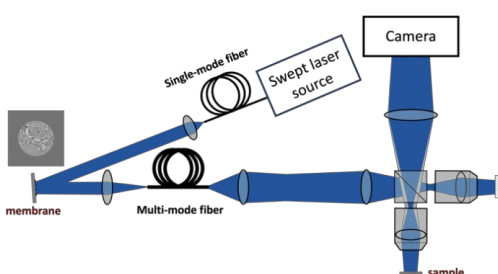
1. Sarkar, B., et al., Application of artificial neural network and particle swarm optimization for modelling and optimization of biosorption of lead (II) and nickel (II) from wastewater using dead cyanobacterial biomass. Journal of the Indian chemical society, 2021. **98**(3): p. 100039.
2. Tee, W.T., et al., Effective remediation of lead (II) wastewater by Parkia speciosa pod biosorption: Box-Behnken design optimisation and adsorption performance evaluation. Biochemical Engineering Journal, 2022. **187**: p. 108629.
3. Karnwal, A., Unveiling the Promise of Biosorption for Heavy Metal Removal from Water Sources. Desalination and Water Treatment, 2024: p. 100523.
4. Sundararaman, T., et al., Biosorption of toxic reactive blue textile dye from effluent water using immobilized biomass based adsorbent. Environment and Natural Resources Journal (EnNRJ), 2024. **22**(1): p. 1-12.

PILNO LAUKO OPTINĖ KOHERENCINĖ TOMOGRAFIJA SU MAŽAIS KOHERENTINIAIS TRIUKŠMAIS

Karolis Adomavičius, Austėja Trečiokaitė, Eriks Tarvydas, Egidijus Auksorius

Fizinių ir technologijos mokslų centras Optoelektronikos skyrius
Saulėtekio al. 3, LT-10257 Vilnius, el. p.: karolis.adomavicius@ftmc.lt

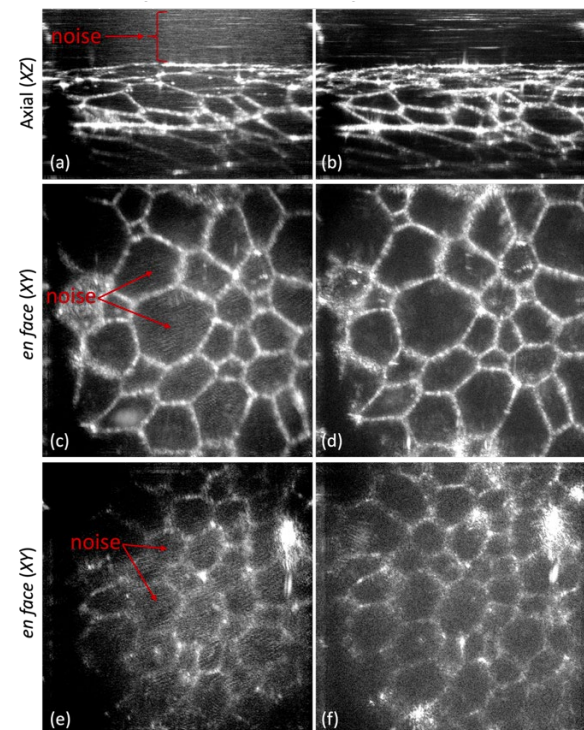
Optinė koherentinė tomografija (OKT) yra neinvazinės metodas, plačiai taikomas trimačiam tinklainės vaizdinimui, kuris padeda aptikti, diagnozuoti ir stebėti jvairias tinklainės ligas. Vis dėlto, OKT technologija vis dar susiduria su iššūkiais, susijusiais su optine skyra, greičiu ir vaizdinimo gyliu. Siekiant padidinti OKT vaizdinimo greitį, nesenai buvo sukurta Furjė erdvės pilnojo lauko OKT (PL-OKT) technologija, kuri naudoja itin greitą kamerą ir derinamo bangos ilgio lazerinį šaltinį trimačiams objekto vaizdams gauti. PL-OKT gali užfiksuoti interferometrinius vaizdus iš gilių biologinio audinio sluoksnių. Tačiau PL-OKT efektyvumą gali riboti tarppikselinė sąveika, atsirandanti dėl lazerio erdvinių koherentiškumo. Šiam triukšmui sumažinti buvo panaudota greitai deformuojama membrana, kuri per kelias mikrosekundes sumažina lazerio erdvinių koherentiškumą [1]. Vėliau buvo parodyta, kad tam pačiam tikslui galima panaudoti ir multimodinį šviesolaidį [2]. Deja, multimodiniai šviesolaidžiai pasižymi modaliniu triukšmu, nes pats šviesolaidis sukuria koherentinius artefaktus, kurie pasireiškia kaip šviesos dėmių (angl. speckle) susidarymas šviesolaidžio gale. Siekdami išvengti šių fluktuacijų, šiame darbe sukombinavome multimodinį šviesolaidį (50 µm šerdies skersmens ir 200 metrų ilgio) su greitai deformuojama membrana (Dyoptika, „Anti-Speckle Technology Evaluation System“), kaip parodyta Pav. 1. Besikeičianti membrana sukuria jvairius fazės pasiskirstymus, kurie keičia lazerio bangos frontą. Tokia šviesa, nukreipta į šviesolaidį, sužadina skirtinges šviesolaidžio modų rinkinius. Dėl šios šviesos randomizacijos, išeinanti šviesa iš šviesolaidžio nebesudaro ryškių dėmių, nes jvairios membranos formos realizacijos suvidurkina dėmes į homogeniškesnį pasiskirstymą. Tokia šviesa yra nukreipiama į PL-OKT sistemą kuri aprašyta ankščiau [2,3].



1 pav. OKT sistema naudojanti multimodinį šviesolaidžio ir membranos kombinaciją koherentinio triukšmo sumažinimui.

2 paveiksle pavaizduoti ląstelių vaizdai, gauti naudojant multimodinio šviesolaidžio ir membra-

nos sistemą, skirtą šviesos koherentiškumui ir koherentiniams triukšmui sumažinti. Čia lyginami vaizdai, užfiksuoti ijjungus ir išjungus membraną skirtinguose pjūviuose. Kaip matyti iš XZ ir XY pjūvių, šviesolaidžio ir membranos derinys sumažina triukšmą ir leidžia gauti didesnio kontrasto vaizdus.



2 pav. Ląstelių vaizdai užregistruoti naudojant multimodinį šviesolaidį (a, c, d) ir jo kombinaciją su membrana (b, d, f) koherentinio triukšmo sumažinimui. Kombinacija padeda geriau atskiratyti koherentinio triukšmo kaip iliustruota raudonomis rodyklėmis.

Šis patobulintas metodas turėtų leisti aptikti mažiau contrastingus tinklainės sluoksnius ir ląsteles, tokias kaip neuronus, kuriuos sunku užfiksuoti naudojant iprastas OKT technologijas.

Literatūra

1. P. Stremplewski, E. Auksorius, P. Wnuk, Ł. Kozoń, P. Garstecki, and M. Wojtkowski, "In vivo volumetric imaging by crosstalk-free full-field OCT," *Optica* 6, 608-617 (2019).
2. E. Auksorius, D. Borycki, P. Wegrzyn, I. Žičkienė, K. Adomavičius, BL. Sikorski, and M. Wojtkowski "Multimode fiber as a tool to reduce crosstalk in Fourier-domain full-field optical coherence tomography," *Opt. Lett.*, vol. 47, no. 4, p. 838, Feb. 2022, doi: 10.1364/OL.449498.
3. E. Auksorius et al., "Spatio-temporal optical coherence tomography provides full thickness imaging of the chorioretinal complex," *iScience*, vol. 25, no. 12, p. 105513, Dec. 2022, doi: 10.1016/j.isci.2022.105513.

FEMTOSEKUNDINIO LAZERIO IMPULSŲ SĄVEIKOS SU AGLIES PLUOŠTU SUSTIPRINTU PLASTIKU (CFRP) TYRIMAI

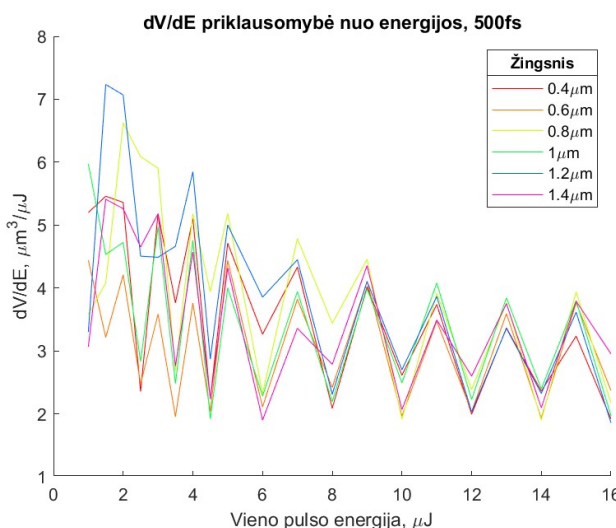
¹Justinas Minkevičius, ^{1,2}Paulius Šlevas, ²Orestas Ulčinas,
¹Egidijus Vanagas, ¹Sergejus Orlovas

¹Fizinių ir technologijos mokslų centras, Fundamentinių tyrimų skyrius
Saulėtekio al. 3, LT-10257 Vilnius

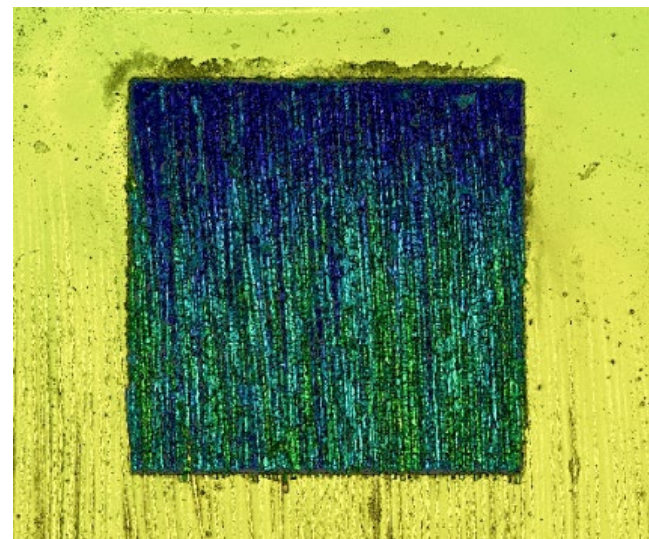
²Workshop of Photonics, Mokslininkų g. 6A, Vilnius, LT-08412 Vilnius, Lietuva
el. p.: justinas.minkevicius@ftmc.lt

Tyrimo objektas yra anglies pluoštu sustiprintas plastikas (CFRP - angl. Carbon Fiber Reinforced Plastic), plačiai naudojama įvairiose srityse kompozitinė medžiaga. Dėl savo išskirtinių savybių - lengvumo, tvirtumo, formavimo paprastumo, atsparumo korozijai ir agresyvios aplinkos poveikiui ir kt. turi platū pritaikymą. Tačiau visos tos puikiosios šio kompozito savybės sukelia ir papildomas problemas kaip sudėtingas kompozito apdorojimas, konkrečiai pjovimas, t.y. kompozito detalių formavimas. Mes siūlome taikyti lazerinį apdorojimą aukšto intensyvumo femtosekundiniai impulsai. Šviesos ir medžiagos (CFRP) sąveikos (pjūvio) vietoje dėl medžiagų savybių skirtumų vyksta skirtingi pakitimai CFRP kompozito sudedamose medžiagose: anglies pluošto skaidulose ir plastike. Dėl šių skirtumų bus įtakojama pjovimo eiga bei kokybė.

Šiame darbe mes orientavomės į lazerinio apdirbimo aukšto intensyvumo femtosekundiniai impulsai tyrimus. Buvo išabliuota po du šimtus $0,25 \text{ mm}^2$ ploto kvadratėlių naudojant 1ps ir 500 fs trukmės impulsus, taip pat variuojamas atstumas tarp impulsų nuo $0,2 \mu\text{m}$ iki $2 \mu\text{m}$ ir impulso energija nuo $1 \mu\text{J}$ iki $16 \mu\text{J}$. Darbe buvo naudojamas vizualinis pjūvio įvertinimas optinio mikroskopio pagalba, atliktas pjūvio sąlygų optimizavimas gauti geriausios kokybės ir spartos pjūvius. Gautų rezultatų charakterizavimao ir tyrimų etape buvo naudojama vizualizavimo mikroskopio pagalba, scanning electron microscopy (SEM) sistema su EDS galimybėmis identifikuoti medžiagų sastato cheminius pokyčius.



2 pav.: $\Delta V / \Delta E$ priklausomybės nuo impulso energijos grafikas 0,4-1,6 μm atstumu tarp impulsų intervalo.



2 pav.: Išabliuoto kvadratėlio profilis. $13 \mu\text{J}$ impulsų energija, bei daromi $0,8 \mu\text{m}$ žingsniai tarp impulse.

OPTICAL AND ELECTRICAL PROPERTIES OF GaAs/AlGaAs LASER DIODES WITH WEAK AND STRONG OPTICAL MODE CONFINEMENT

Karina Pokaliuk, Algimantas Lukša, Renata Butkutė, Viktorija Nargelienė

Center for Physical Sciences and Technology,
Department of Physical Technologies, Department of Optoelectronics
Saulėtekio av. 3, LT-10257 Vilnius, email: karina.pokaliuk@ff.stud.vu.lt

GaAs/AlGaAs multiple quantum well (MQW) laser diodes (LDs) are used in modern optoelectronic components as they can operate in the therapeutic wavelength range of 750-1200 nm [1]. In areas such as biosensors, medical devices and integrated photonic systems, they are attracting a lot of attention due to their compactness and efficiency [2][3]. Optimizing the fabrication technique of GaAs/AlGaAs LDs is essential for their performance. This study focuses on the fabrication and comparison of laser diodes with weak and strong optical mode confinement, examining how these different fabrication techniques affect their optical and electrical properties.

LDs with two different types of optical mode confinement (Fig. 1.) have been fabricated using different ridge etching techniques: shallow etching for weak optical mode confinement and deep etching for strong optical mode confinement.

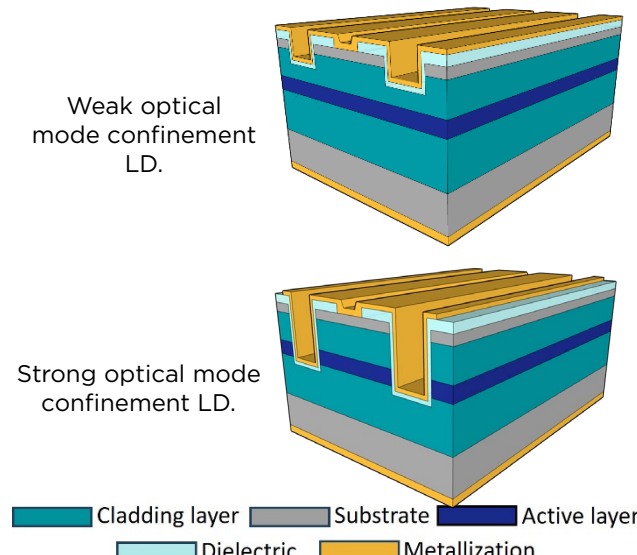


Fig. 1. Two different optical mode confinement LD structures.

Both types of diodes having various resonator lengths were tested to investigate how these structural changes affect their threshold current, optical power and quantum efficiency. From the characterization results, it was found that LDs with strong optical mode confinement exhibit lower threshold currents (Fig. 2.). However, they

also exhibit lower differential quantum efficiency compared to diodes with weak optical mode confinement, which can be explained by electrical and optical losses due to deep etching during fabrication.

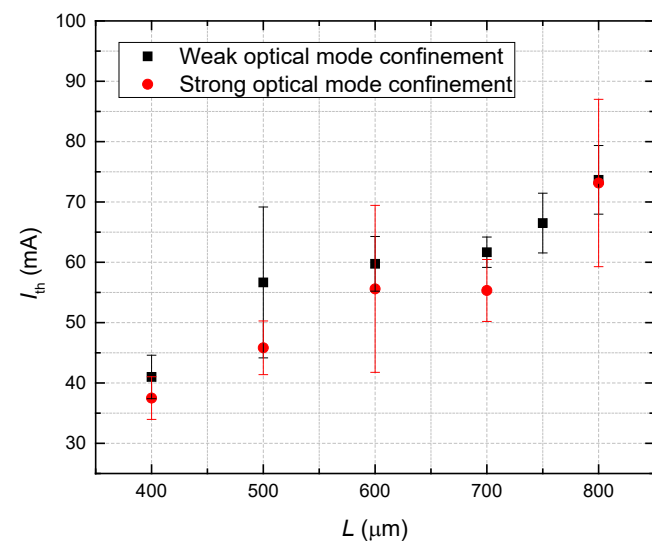


Fig. 2. Threshold current dependence on laser diode cavity length of LD with weak (black squares) and strong (red dots) optical mode confinement.

These findings highlight the trade-offs between fabrication complexity and device efficiency, and therefore provide valuable insights into how to optimize laser diode fabrication for different applications.

References:

- [1] A. Dhakal, P. Wuytens, F. Peyskens, A. Z. Subramanian, N. Le Thomas, and R. Baets, "Silicon-nitride waveguides for on-chip Raman spectroscopy," *Opt. Sens. Detect. III*, vol. 9141, p. 91411C, May 2014, doi: 10.1117/12.2057509.
- [2] V. P. Rachim and W. Y. Chung, "Wearable-band type visible-near infrared optical biosensor for non-invasive blood glucose monitoring," *Sensors Actuators B Chem.*, vol. 286, pp. 173-180, May 2019, doi: 10.1016/J.SNB.2019.01.121.
- [3] M. Sanna *et al.*, "SiN integrated photonic components in the visible to near-infrared spectral region," *Opt. Express*, Vol. 32, Issue 6, pp. 9081-9094, vol. 32, no. 6, pp. 9081-9094, Mar. 2024, doi: 10.1364/OE.514505.

INTERNAL QUANTUM EFFICIENCY OF GaAsBi/GaAs MQW STRUCTURES

Aistė Štaupienė, Aivaras Špokas, Andrea Zelioli, Augustas Vaitkevičius,
Bronislovas Čechavičius, Renata Butkutė, Evelina Dudutienė

Center for Physical Sciences and Technology, Department of Optoelectronics
Saulėtekio av. 3, LT-10257 Vilnius, email: aiste.staupiene@ftmc.lt

GaAsBi quantum well (QW) structures have a lot of favorable properties for optoelectronic devices operating in the near-infrared (NIR) region [1]. The first characteristic of GaAsBi is the significant redshift of the bandgap with an increase in Bi content [2]. Also, the incorporation of Bi induces strong spin-orbit splitting, surpassing the bandgap energy when Bi content exceeds 10.5 %, which can have beneficial effect of suppressing Auger recombination and intervalence band absorption processes [3]. Moreover, the bandgap of GaAsBi has low sensitivity to temperature variations. Thus, the use of the GaAsBi quantum structures as the active medium, allows to create a tunable laser on a well-developed GaAs platform that operates at room temperature without additional cooling.

However, the complicated growth of GaAsBi often leads to a high concentration of defects, resulting in low luminescence intensity. To reduce the defect density in such structures it is necessary to optimize the growth of GaAsBi QWs, which cannot be done without the investigation of its optical properties.

For this reason, a detailed optical study using photoluminescence (PL) technique was conducted to investigate optical characteristics, especially the internal quantum efficiency (IQE) of a GaAsBi/GaAs multiple QW (MQW) structures.

Studied structures were grown by the molecular beam epitaxy (MBE) method as an active area for Vertical-external-cavity surface-emitting lasers (VECSELs) [4]. These investigated structures represent new growing method for the active area for VECSELs, where the pairs of QWs are placed periodically to match the antinodes of the optical standing wave. This allows to have thinner structures with higher homogeneity and enhanced PL intensities.

This study compared two samples, which were grown at different temperatures (425 °C and 435 °C) and therefore contained different concentrations of Bi (7.6 % and 7.1 %). Observed PL bands in the room temperature PL measurements of 1.06 eV and 1.09 eV were assigned to optical transitions in QWs of GaAsBi. The results from temperature dependent PL measurements (4 - 300 K) revealed S-shaped temperature dependence of PL peak positions in both structures. This was explained by the high

localization effect (>30 meV), which is present even at room temperature.

Additionally, we calculated photoluminescence emission efficiency, analyzed different carrier recombination processes and demonstrated a new method to quantitatively evaluate the QW photoluminescence efficiency for bismide structures. The IQE values of ~10 m% were acquired by absolute method with an integrating sphere and compared with a newly developed ABB* method (see fig.1), which includes contribution from trap-assisted Auger-Meitner non-radiative recombination.

It should be noted that extremely low efficiencies were associated with the low growth temperature of the material, resulting in a high density of defects in the material.

All in all, this work presents a new modified method used for the IQE assessment of GaAsBi/GaAs MQW structures, which allows not only to compare structures grown and characterized in different laboratories, but also to evaluate both radiative and non-radiative mechanisms, which could enhance the optimization of GaAsBi structure growth.

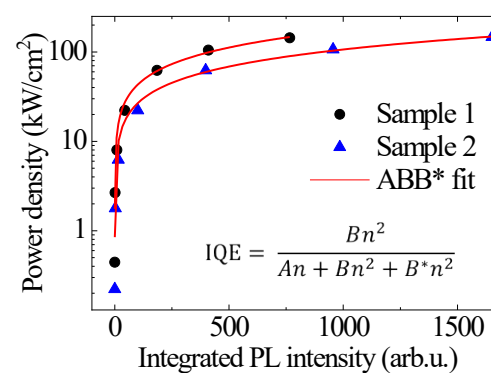


Fig. 1 IQE evaluation using ABB* method.

References

1. R. D. Richards et al. physica status solidi (b) **259(2)** (2022).
2. J. Yoshida et al. Japanese Journal of Applied Physics **42** (2003).
3. K. Alberi et al. Applied Physics Letters **91** (2007).
4. K. S. Kim et al. IEEE Photonics Technology Letters **19(20)** (2007).

This work is supported by Research Council of Lithuania under Contract No. S-LLT-23-3.

KVANTINIŲ IR KLASIKINIŲ SISTEMŲ ANALOGIJOS

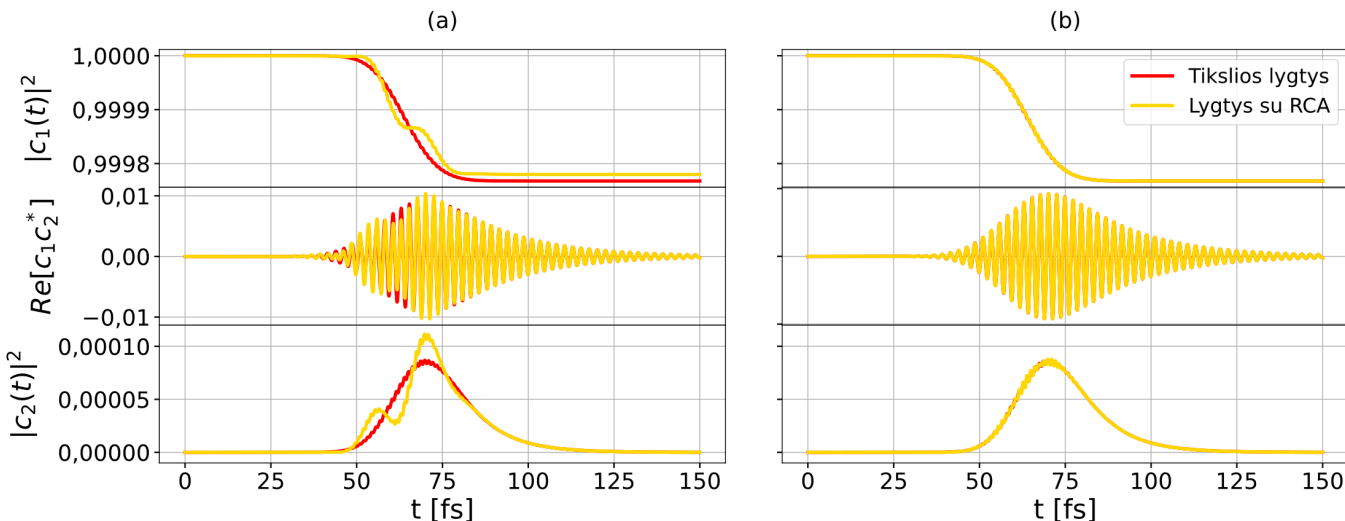
Justina Vaičaitytė^{1,2}, Andrius Gelžinis^{1,2}, Leonas Valkūnas^{1,2}

¹Fizinių ir technologijos mokslų centras, Molekulinių darinių fizikos skyrius,
Saulėtekio al. 3, LT-10257 Vilnius

²Vilniaus universitetas, Fizikos fakultetas, Saulėtekio al. 9, LT-10222 Vilnius
el. p.: justina.vaicaityte@ff.stud.vu.lt

Kvantinė mechanika leidžia aprašyti mikroskopinių sistemų savybes. Tačiau dalis taip aprašomų savybių gali turėti ir klasikinius atitikmenis, nors tai ne visada yra akivaizdu. Kai kuriuos kvantinės dinamikos aspektus galima analizuoti naudojant klasikines sistemas, jeigu šios aprašomas matematiškai ekvivalentiškomis lygtimis. Tokių sistemų pavyzdys yra klasikinių osciliatorių rinkiniai. Alexander Eisfeld ir John S. Briggs parodė, jog nenuostovioji Šredingerio lygtis N lygmenų sistemai gali būti visiškai tiksliai atvaizduota klasikinėmis Hamiltono lygtimis tokiam

ir Eisfeld metodiką kelių lygmenų sistemoms. Mūsų darbe buvo nagrinėtos kelių lygmenų disipatyvios sistemos su neermitiniu nuo laiko priklausančiu hamiltonianu, turinčiu kompleksines tikrines vertes. 1 pav. (a) pavaizduotas dimerio užpildų bei koherentiškumų laikinių evoliucijų palyginimas naudojant tikslias kvantines lygtis bei lygtis pritaikius RCA aproksimaciją dviejų lygmenų sistemai, su energijomis ε_1 ir ε_2 , kurios būsenos sąveikauja tik dėl išorinio lauko $A(t)$. Laikoma, kad sužadinta būsena relaksuoja su sparta γ į pagrindinę būseną. Žinoma,



1 pav. Tankio operatoriaus elementų laikinės evoliucijos tikslaus kvantinio sprendinio (raudona linija) ir sprendinio su RCA (geltona linija) palyginimas. Parametrų vertės: $\varepsilon_1 = 1000 \text{ cm}^{-1}$, $\varepsilon_2 = 15000 \text{ cm}^{-1}$, $\gamma = 0,5 \text{ fs}^{-1}$, $A(t) = A_0 \exp\left(-\frac{(t-t_0)^2}{2\sigma^2}\right) \cos \Omega(t-t_0)$, $A_0 = -8,23 \text{ cm}^{-1}$, $t_0 = 60 \text{ fs}$, $\sigma = 10 \text{ fs}$, $\Omega = \varepsilon_2 - \varepsilon_1$. Priedas prie sužadinimo energijų: (a) 0 cm^{-1} , (b) 15000 cm^{-1} .

pačiam skaičiui sukabintų osciliatorių, kai kvantinės sistemos hamiltonianas yra realus ir ermitinis [1]. Vėlesnė tų pačių autorų analizė apémė ir nuo laiko priklausančius kompleksinius hamiltonianus [2]. Vis dėlto, gaunamos sukabintos osciliatorių lygtys bendru atveju gali būti sudėtingos formos. Viena iš priežasčių yra tai, kad gautoje klasikinėje Hamiltono funkcijoje yra ir osciliatorių apibendrintujų judesio kiekiei sąveikos. Nepaisant to, jeigu kvantinės sistemos būsenų tarpusavio sąveikos V_{nm} yra daug mažesnės už sužadinimo energijas ε_n ir tenkinama sąlyga $\varepsilon_n + \varepsilon_m \approx 2\varepsilon_n$, galima pakankamai tiksliai aprašyti kvantinę sistemą naudojant ženkliai paprastesnes Hamiltono lygtis. Ši aproksimacija atitinka narių $p_n p_m$ ($n \neq m$) pašalinimą iš Hamiltono funkcijos ir yra vadinama RCA aproksimacija (angl. *realistic-coupling approximation*) [3].

Šiame darbe buvo nagrinėjamas kvantinių sistemų atvaizdavimas klasikiniais osciliatoriais taikant Briggs

kad kvantinių sistemų tankio operatoriaus elementų priklausomybė nuo laiko nekinta pridėjus konstantą prie diagonalinių hamiltoniano elementų. Šiame darbe parodyta, kad RCA galiojimo ribas galima ženkliai praplėsti dirbtinai pastūmus sužadinimo energijų vertes (žr. 1 pav. (b)).

Reikėtų paminėti, jog klasikinėmis lygtimis galima aprašyti daug kvantinių reiškinių, tokius kaip kvantinis tuneliaivimas arba interferencija. Mūsų tikslas ateityje yra pritaikyti Briggs ir Eisfeld metodiką molekulinių sistemų spektrų skaičiavimams.

Literatūra

1. J. S. Briggs ir A. Eisfeld, *Phys. Rev. A* **85**, 052111 (2012).
2. J. S. Briggs ir A. Eisfeld, *Phys. Rev. A* **88**, 062104 (2013).
3. J. S. Briggs ir A. Eisfeld, *Phys. Rev. E* **83**, 051911 (2011).

GaAsBi NIR EMITTERS FOR INTEGRATED BIOSENSORS IN WEARABLE TECHNOLOGY

Aivaras Špokas¹, Andrea Zelioli¹, Andrius Bičiūnas¹, Bronislovas Čechavičius¹,
Augustas Vaitkevičius^{1,3}, Virginijus Bukauskas², Mindaugas Kamarauskas²,
Evelina Dudutienė¹ and Renata Butkutė¹

¹Center for Physical Sciences and Technology, Department of Optoelectronics
Saulėtekio av. 3, LT-10257 Vilnius, Lithuania
email: aivaras.spokas@ftmc.lt

²Center for Physical Sciences and Technology, Department of Physical Technologies
Saulėtekio av. 3, LT-10257 Vilnius, Lithuania

³Institute of Photonics and Nanotechnology, Faculty of Physics, Vilnius University,
Saulėtekio av. 3, LT-10257, Vilnius, Lithuania

Recently small size semiconductor emitters have found commercial success in integrated biosensing applications. One of such examples is the optical measurements present in wearable smart devices, fitness trackers. One of the following vital signs that can be measured optically is the blood oxygen content. The technology of pulse oximetry has long been used by employing two wavelengths one in the visible range at 660 nm and near infrared (NIR) at 940nm [1]. Whilst this is sufficient and accurate in transmission mode devices like finger or ear clips, there are considerable issues with the accuracy in reflectance mode due to the difference in penetration depth into soft tissue. A proposed solution is utilizing two NIR wavelengths at 800 nm and 1100 nm, where the effective penetration depth is almost the same, but the absorption differences in oxy-/deoxy-hemoglobin remain sufficient for detection.

While emitters working at 800 nm are easily realized via classical approach, using AlGaAs/GaAs quantum structures, fabricating emitters working at 1100 nm is more challenging and requires unconventional material engineering strategies. The material system chosen for longer wavelength operation is GaAsBi/GaAs quantum wells (QWs). Using GaAsBi for the active region of emitters has been shown to present a variety of advantageous properties. First of all, substituting As atoms with Bi results in a large bandgap reduction of 88 meV/%Bi [2]. This helps in preventing relaxation, since a small fraction of host atoms has to be replaced to achieve wavelengths of 1100 nm and higher, which is not the case for other ternary GaAs based material systems. Secondly, GaAsBi has been shown to have an anomalously temperature insensitive bandgap, which is a crucial advantage, when considering devices intended room-temperature operation [3]. Finally, introduction of Bi not only influences the band gap but also rapidly increases the spin-orbit splitting energy, which becomes larger than the bandgap at a Bi fraction of 10.5%, consequently suppressing one of the major non-radiative Auger recombination channels [4].

Despite, the plethora of beneficial properties of the alloy its growth is complicated and requires specific technological solutions. First, a low group V (As) overpressure is required. Since Bi and As compete for the same sites in the GaAs lattice a stoichiometric As/Ga ratio promotes Bi introduction [5]. Additionally, growth of GaAsBi requires a low temperature growth, with 420 °C being the threshold of incorporation [6]. This work focuses on the molecular beam epitaxy (MBE) growth of GaAsBi/GaAs MQW structures and fabrication of emitters operating in the range of 1050

nm to 1150 nm. All of the presented structures were grown using a solid-state Veeco *GENxplor R&D* MBE system, equipped with standard metallic sources for Ga, Al, Bi, Be, Si and a unique As source that is both valved and cracked providing a purely dimeric As flux, with an ability to precisely control the flux, which is crucial, for sensitive control of the As/Ga ratios.

For the growth of the emissive layers a temperature limited GaAsBi growth regime was identified to be preferred for structures with high Bi fractions (>6%). It was realized by supplying a high Bi flux (well in excess of maximum incorporation threshold) and controlling the bismuth fraction by changing the temperature. GaAsBi/GaAs MQW structures with emission in the range from 1080 nm to 1320 nm were successfully reproduced in the temperature interval of 305 - 365 °C. Spatially resolved photoluminescence techniques were utilized to observe the absence of lattice mismatch dislocations in GaAsBi MQW structures emitting at central wavelengths longer than 1100nm. Furthermore, several diode structures were grown on thick (500 - 1000 nm) AlAs sacrificial layer, which is necessary for device transfer onto a silicon-based platform. Firstly, a GaAsBi/GaAs 5x rectangular quantum well (RQW) light emitting diode was grown with a peak emission registered at 1070 nm, temperature dependent electroluminescence measurements confirm the stability of the bandgap in a temperature range from 30 to 300 K, where an emission peak shift of only 27 nm is observed. Moreover, a GaAsBi/GaAs 3xRQW laser diode was produced, and lasing was registered at 1142 nm via pulsed electrical pumping at room temperature.

The work (“Apvalkalinio p-AlGaAs sluoksnio technologijos vystymas lazerinių diodų integracijai ant Si platformos”) was supported by the Research Council of Lithuania under agreement no. P-ST-24-170.

References

1. J.E.Sinex, Am. J. Emerg. Med. **17**, 59-67 (1999)
2. S.Francœur, M.J.Seong, A.Mascarenhas, S.Tixier, M.Adamcyk, T.Tiedje, Appl. Phys. Lett. **82** (22), 3874-3876 (2003)
3. Y.Tominaga, K.Oe, M.Yoshimoto, Appl. Phys. Exp. **3** (6) 1-4 (2010).
4. K.Alberi, O.D.Dubon, W.Walukiewicz, K.M.Yu, K.Bertulis, A.Krotkus. Appl. Phys. Lett., **91**, 10-13 (2007).
5. J. Puustinen J.Hilska, M.Guina, J. Cryst. Growth, **511**, 33-41 (2019).
6. R.D.Richards, F.Bastiman, C.J.Hunter, D.Mendes, A.R.Mohmad, J.S.Roberts, J.P.R.David, J. Cryst. Growth **390** 120-124 (2014).

RELATION BETWEEN PHOTOLUMINESCENCE INTENSITY OF InGaAs QUANTUM WELLS AND DESIGN OF AlGaAs BARRIERS

Monika Jokubauskaitė, Aistė Butkutė, Evelina Dudutienė, Aivaras Štokas,
Andrea Zelioli, Bronislovas Čechavičius, Renata Butkutė

Center for Physical Sciences and Technology, Department of Optoelectronics
Saulėtekio av. 3, LT-10257 Vilnius, email: monika.jokubauskaite@ftmc.lt

Optoelectronic devices operating in the near infrared range (NIR) are highly demanded in various fields, such as medicine, telecommunications, data transferring, military, security, environmental monitoring, etc. The fabrication of active media of NIR light sources that could be used for these applications is hindered by the lack of suitable materials with high optical performance. Although the idea to employ quantum well (QW) structures as an active media has been around for a while, the question of how to achieve optimal optical performance of these quantum structures still remains. Therefore, researchers are looking for the ways to improve luminescence properties of QWs by studying luminescence intensity dependence on growth parameters as well as details of structure design.

A concept of graded barriers was firstly mentioned back in 1987 by J. Feldmann *et al.* [1] where carrier trapping into QW efficiency was studied among GaAs/AlGaAs single quantum wells with different barrier designs. This investigation revealed trapping efficiencies reaching up to 100% in GaAs QWs with parabolically or linearly graded AlGaAs barriers. Moreover, GaAsBi quantum wells with parabolically graded AlGaAs barriers exhibited significantly higher photoluminescence (PL) intensity reported by S. Pūkienė *et al.* [2]. It is also important to mention that increased PL intensity was consistently reproducible under growth conditions.

In this work InGaAs QWs with different designs of AlGaAs barriers were grown by molecular beam epitaxy. PQW consists of one rectangular 5.7 nm width InGaAs QW inserted between 30 nm width AlGaAs parabolically graded barriers with the content of Al grading from 30% at the top to 0% (GaAs) at the bottom of the barriers. TrQW is one rectangular 5.7 nm width InGaAs QW inserted between 30 nm width AlGaAs linearly graded barriers. Reference sample RQWs consists of twelve rectangular 5.7 nm width InGaAs QWs separated by GaAs barriers of 7 nm width. PL measurements were carried out for RQWs, PQW and TrQW structures. Room temperature PL (Fig. 1 (a)) revealed higher intensity of PQW structure compared to TrQW and RQWs. Additionally, the emission peak of RQWs sample is observed at lower photon energies which could indicate wider QWs in this structure or smaller In

concentration in graded barrier structures (PQW and TrQW). Such deviation of PL peak should be taken into account when depositing quantum structures with specific wavelength. Photoluminescence measurements were also carried out in a wide temperature range of 0 – 300 K and PL peak positions as a function of temperature are graphed in Fig. 1 (b). Measurements data were fitted using Varshni function:

$$E(T) = E_0 - \frac{\alpha T^2}{\beta + T}$$

where E is the energy of material, E_0 is the band gap at 0 K, α describes band gap sensitivity to temperature and β is a parameter related to Debye temperature. Overall, it is clear that PL intensity is improved by employing graded barriers. Higher performance of PQW quantum structure could be associated with more mature growth technology of PQW structures rather than TrQW structures.

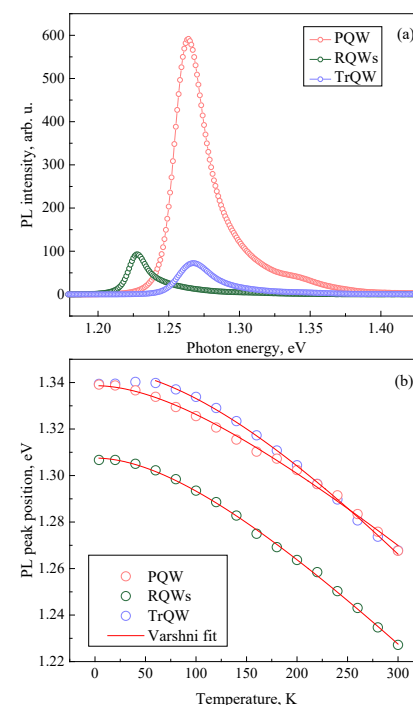


Fig. 1 (a) PL spectra of InGaAs/AlGaAs quantum structures measured at room temperature. (b) Temperature dependence of the PL peak energy.

References

1. J. Feldmann, G. Peter, E. O. Göbel, K. Leo, H.J. Polland, K. Ploog, K. Fujiwara, and T. Nakayama, *Appl. Phys. Lett.* **51**, 226 (1987).
2. S. Pūkienė, M. Karaliūnas, A. Jasinskas, E. Dudutienė, B. Čechavičius, J. Devenson, R. Butkutė, A. Udal, and G. Valušis, *Nanotechnology* **30**, (2019).

SYNTHESIS AND APPLICATION OF $Ti_3C_2T_x$ MXENES FOR DETERMINATION OF DRINKING WATER QUALITY AND POLLUTANT REMOVAL

Kristina Sobol^{1,2}, Almira Ramanaviciene¹, Simonas Ramanavicius²

¹NanoTechnas – Center of Nanotechnology and Materials Science, Institute of Chemistry, Faculty of Chemistry and Geosciences, Vilnius University, Naugarduko St. 24, LT-03225, Vilnius, Lithuania

²Center for Physical Sciences and Technology, Department of Electrochemical Material Science, Sauletekio av. 3, LT-10257, Vilnius, Lithuania

kristina.sobol@chgf.stud.vu.lt

The urgent and significant consequences of global industrialization are continuing to impact the ecosystem. Millions of tons of pollutants are being released into the water worldwide, posing a serious threat to the health of both humans and animals. This underscores the critical need for the development of cost-effective, sensitive, and environmentally safe technologies for removing water pollutants, particularly organic dyes and metal ions [1].

MXenes, a novel family of two-dimensional (2D) inorganic nanomaterials, first discovered in 2011, hold great promise for environmental applications. The MXene family, with the general structure of $M_{n+1}X_nT_x$, where M is a transition metal, X is C and/or N, and T_x is the surface functional group, consists of transitional metal carbides, nitrides, and carbonitrides. Their large surface area, simple surface functionalization, hydrophilicity, biocompatibility, and high adsorption capacity of both organic and inorganic contaminants make MXenes a promising solution for environmental challenges [2]. Our focus here is on MXene-based colorimetric technologies for the removal of organic dyes and the detection of Ag^+ ions in water samples.

In this study, we successfully synthesized and applied spherical and layered -SO₄ and -F functionalized $Ti_3C_2T_x$ MXenes for the adsorption of Rhodamine B and Methylene blue dyes, as model molecules. We evaluated their adsorption capacity and reproducibility using spectrophotometric methods. The layered MXenes demonstrated excellent dyes removal

efficiency, were successfully regenerated and reused. Subsequently, we investigated the adsorption of Ag^+ ions by spherical MXenes, revealing a linear correlation between Ag^+ concentration and the MXene absorption registered signal. Changes in Ag^+ concentration were observed spectrophotometrically and visually, with a noticeable color change of the solution as the concentration of ions increased. These successful results offer valuable insights into the potential application of -SO₄ and -F functionalized $Ti_3C_2T_x$ MXenes for practical application for wastewater treatment.

Acknowledgment: This project has received funding from the Research Council of Lithuania (LMTLT), agreement No S-MIP-24-14.

References

1. P.M.Boersenberger D. Bury, M. Jakubczak, R. Kumar, D. Sciezynska, B.Jan, P. Marcinowski, A. M. Jastrzebska, Cleaning the environment with MXenes, MRS Bulletin, 48, 10.1557/s43577-023-00507-6 (2023).
2. C. E. Shuck, K. Ventura-Martinez, A. Goad, S. Uzun, M.Shekhirev, Y. Gogotsi, Safe Synthesis of MAX and MXene: guidelines to reduce risk during synthesis, ACS Chem. Health Saf, 28, 326-338 (2021).

EXPLORING THE FEASIBILITY OF BISMUTH δ -DOPING OF GaAs/AlAs QUANTUM WELLS: AN OPTICAL STUDY

Justas Žuvelis, Evelina Dudutienė, Bronislovas Čechavičius, Renata Butkutė

Center for Physical Sciences and Technology, Department of Optoelectronics,
Saulėtekio av. 3, LT-10257 Vilnius, email: justas.zuvelis@ftmc.lt

The ever-growing demand for smaller semiconductor devices with improved physical properties, such as reduced power consumption and higher speeds, necessitates scaling down the distribution of impurities alongside the crystal structure itself. One method for achieving this is known as delta-doping, where dopants are confined to a single or a few monolayers (ML) of the lattice. While δ -doping with silicon (Si) and beryllium (Be) has been extensively studied and shown to improve carrier mobility and enable high tunability of the energy band structure [1, 2, 3], no research has been conducted on bismuth (Bi).

In this research, five different 5 nm-width GaAs/AlAs quantum well (QW) structures containing 0 (reference), 1, 4, 6, and 8 ML of Bi were studied using temperature-dependent photoluminescence (PL) and photoreflectance (PR) techniques to assess the feasibility of δ -doping by Bi atoms and the resulting optical properties.

The key issue when incorporating bismuth arises from its large atomic size, being 25% larger than As, and 5% than Ga. This not only causes deformations of the lattice but further requires the semiconductor to be grown at suboptimal temperatures to minimize dopant segregation. For this research, δ -doping with Bi was attempted at 425°C, noticeably lower than the standard temperature for GaAs of 600°C, which consequently increased the concentration of defects. As a result, these factors caused a significant reduction in PL emission— at 300 K, the signal obtained from the sample containing 1 ML of Bi was approximately 80 times weaker than that of the reference. Nonetheless, conducted TDPL measurements revealed that QW structures containing ≤ 4 ML of δ -Bi exhibit new energy states below the GaAs/AlAs QW bandgap (Fig. 1).

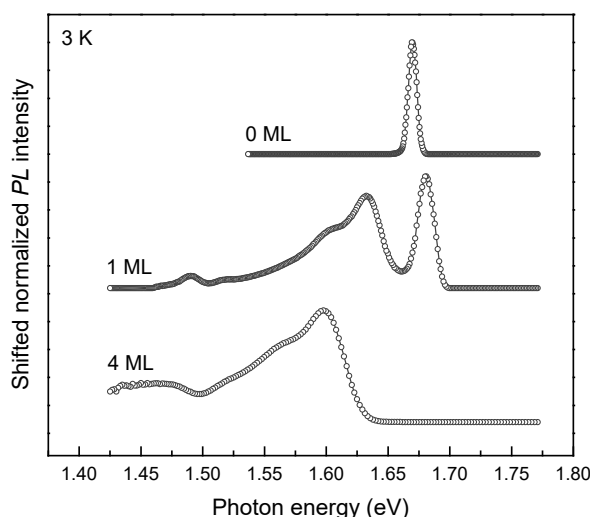


Figure 1. Photoluminescence measurements at 3 K of the reference, alongside the structures with 1 and 4 ML of δ -Bi.

In the case of photoreflectance, quantum-wells with up to 4 ML of Bi were successfully investigated across a wide temperature range between 3 K and 300 K. TDPR results, fitted to Aspnes' first-derivative function [4], alongside optical transition energies obtained from TDPL measurements were analyzed by Varshni temperature-dependent bandgap equation [5]. The obtained α parameters— 0.65 ± 0.03 meV/K⁻¹ for the reference and 0.58 ± 0.03 meV/K⁻¹ for the 4 ML sample—indicate that δ -doping with Bi has the potential to improve thermal stability.

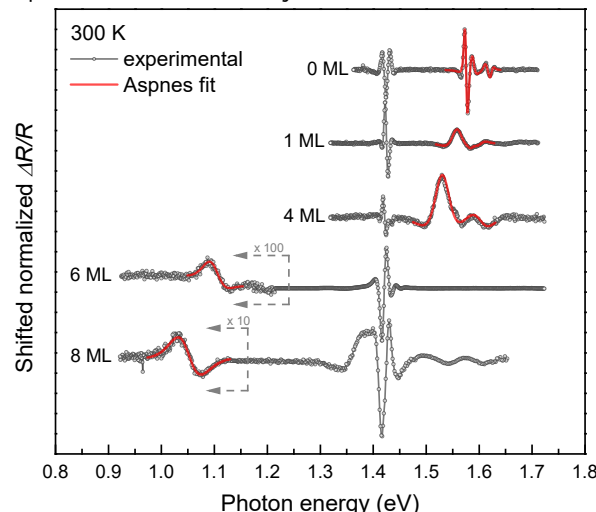


Figure 2. 300 K photoreflectance spectra of structures containing 0, 1, 4, 6, and 8 ML of bismuth, fit to Aspnes' function [4].

Furthermore, owing to the high-sensitivity of modulation spectroscopy, measurements below the bandgap of bulk GaAs (Fig. 2) revealed that δ -doping with ≥ 6 ML of bismuth leads to the formation of a narrow (< 5 nm) GaAsBi/GaAs QW within the preexisting GaAs/AlAs QW structure.

Acknowledgements: this research was funded by the Research Council of Lithuania, grant No. P-SV-24-401.

References

1. J.J. Harris, "Delta-doping of semiconductors". *J Mater Sci: Mater Electron* 4, 93–105 (1993).
2. J. Kundrotas, A. Čerškus, G. Valušis, M. Lachab, S. P. Khanna, P. Harrison, and E. H. Linfield. "Radiative recombination spectra of p-type δ -doped GaAs/AlAs multiple quantum wells near the mott transition". *Journal of Applied Physics*, 2008.
3. B. Čechavičius, J. Kavaliauskas, G. Krivaitė, G. Valušis, D. Seliuta, M. P. Halsall, and P. Harrison. "Photo- and electro-reflectance spectroscopy of δ -doped GaAs/AlAs multiple quantum-well structures". *Physica status solidi (a)*, 2007.
4. D. E. Aspnes, *Surf. Sci.* 37, 418–442 (1973).
5. Y. P. Varshni, *Physica*, 36 (1), 149–154 (1967).

FABRICATION OF A Cu₂O THIN FILM VIA OXIDATION FOR APPLICATION IN SbSel HETEROJUNCTIONS

Aistis Melnikas, Vidas Pakštas, Rokas Kondrotas

Center for Physical Sciences and Technology, Department of Characterisation of Materials Structure
Saulėtekio av. 3, LT-10257 Vilnius, email: aistis.melnikas@ktu.edu

Antimony selenium iodide (SbSel) is among the most promising inorganic semiconductors composed of inexpensive and abundant chemical elements, with E_g of 1.7 eV and a high absorption coefficient [1]. As this represents a relatively novel solar cell technology, no efficient SbSel heterojunction has yet been developed for optimal extraction of light-generated charge carriers. Based on the energy levels of SbSel and cuprous oxide (Cu₂O), heterojunction of SbSel/Cu₂O promises an efficient charge carrier separation, however this has not been proven experimentally. Therefore, the main objective of our research is to fabricate Cu₂O thin films via oxidation for application in SbSel heterojunctions. The synthesis of thin Cu₂O films via oxidation by varying pressure and temperature is also not thoroughly discussed. Although the phase transition diagram under equilibrium conditions is well established for Cu-O system [2], the kinetic part of oxidation plays a vital role when process duration and temperature are short and low. In this work, we systematically investigated the Cu thin film oxidation taking into account pressure, temperature, and time.

The experimental process begins with the sputtering of metal copper for 200 seconds under an argon atmosphere on FTO glass substrates via magnetron. The substrates are then inserted into a tube furnace for oxidation under the chosen static pressure ranging from 1 to 1000 mbar and static temperature ranging from 150 – 550 °C for 30 minutes. Thin films are then analyzed by X-ray diffraction analysis, characterized via ultraviolet-visible (UV-Vis) spectroscopy in the 300 – 1000 nm range, and surface morphology and thickness of thin films are analyzed using scanning electron microscopy (SEM).

A kinetic phase transition diagram (Fig. 2.) at different pressures and temperatures was determined, optimal conditions for pure phase Cu₂O thin film synthesis were ascertained, hence thin films of pure Cu₂O composition were used as substrates for antimony selenium iodide deposition. SbSel was deposited using a thermal evaporator, thin films were then annealed at temperatures ranging from 150 to 200 °C and a time frame of 10 – 30 minutes, hence the optimal annealing conditions for antimony selenium iodide thin films were determined. Aluminum was chosen as metal contacts for the devices, J-V characterization was carried out as a proof of concept. Optimal conditions for pure Cu₂O thin

film synthesis were determined at 1 mbar, 500 °C and 30 minutes. Annealing conditions of SbSel thin films were reflected in J-V characteristics, annealing at 150 °C for 30 minutes showed the best diode-like behaviour.

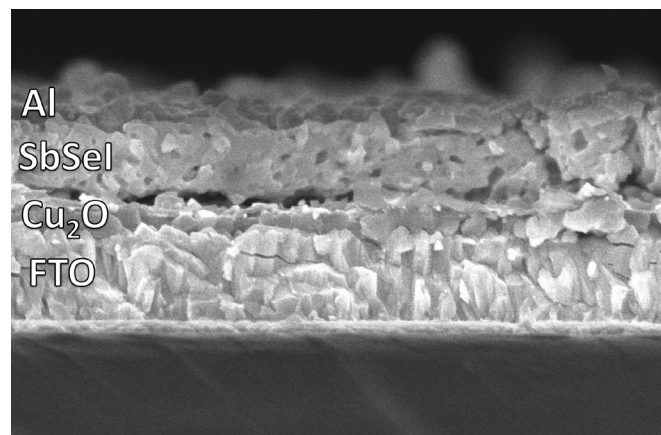


Fig. 1. Cross-section of obtained device.

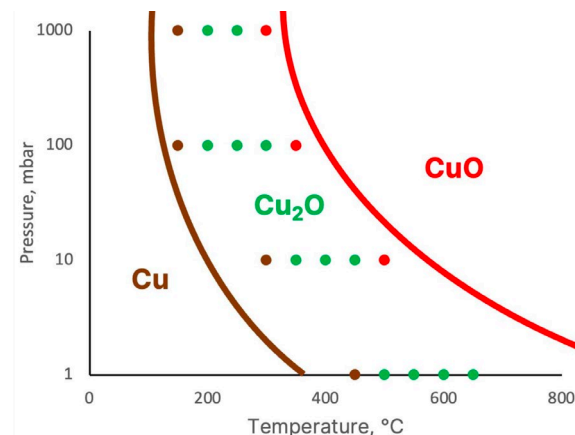


Fig. 2. Obtained phase transition diagram.

References

- I. Cano, ~ A. Navarro-Güell, E. Maggi, M. Barrio, J.L. Tamarit, S. Svatek, E. Antolín, S. Yan, E. Barrena, B. Galiana, M. Placidi, J. Puigdollers, E. Saucedo, SbSel and SbSeBr micro-columnar solar cells by a novel high pressure-based synthesis process, *J. Mater. Chem. A* (2023) 17616–17627, <https://doi.org/10.1039/d3ta03179a>.
- H. Amekura, O.A. Plaksin, K. Kono, Y. Takeda, N. Kishimoto, Production of Cu₂O nanoparticles in SiO₂ by ion implantation and two-step annealing at different oxygen pressures, *J. Phys. D: Appl. Phys.* 39 (2006) 3659–3664, <https://doi.org/10.1088/0022-3727/39/16/020>

FULL-FIELD OPTICAL COHERENCE TOMOGRAPHY WITH DIGITAL DEFOCUS CORRECTION IN HIGHLY SCATTERING SAMPLES

Austėja Trečiokaitė, Karolis Adomavičius, Egidijus Auksorius

Center for Physical Sciences and Technology, Department of Optoelectronics
Saulėtekio av. 3, LT-10257 Vilnius, email: austeja.treociokaite@ftmc.lt

Full-Field Optical Coherence Tomography (FF-OCT) is a fast, non-invasive interferometric technique for acquiring high-resolution *en face* images deep within the sample. To avoid crosstalk in images, a low-coherence light source is used, instead of a laser that is commonly used in holography/interferometry [1]. However, computational aberration/defocus correction, which is possible in Fourier-domain FF-OCT systems using lasers [2], is challenging when using incoherent light source, such as LED. Here we demonstrate a digital defocus correction over a large range of defocus values in FF-OCT employing LEDs.

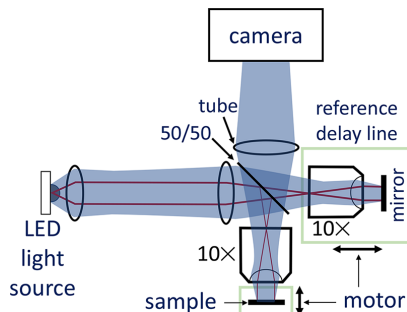


Figure 1. Principal scheme of FF-OCT system. Dark blue represents spatially incoherent LED illumination path, red, spatially coherent laser. Green boxes indicate translation stages equipped with stepping motors.

FF-OCT system, shown in Fig. 1, featured Linnik interferometer with two identical objective lenses and a spatially coherent or incoherent illumination source. Fig. 2 shows a procedure of digital defocus correction on a defocused resolution target.

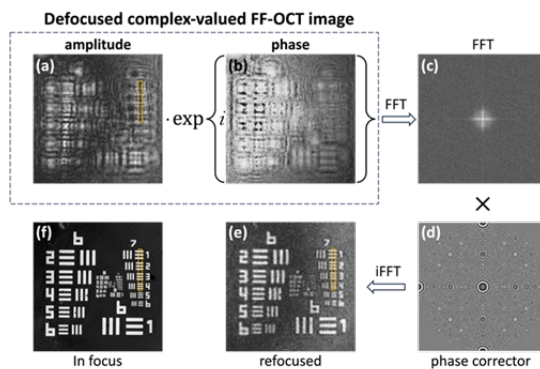


Figure 2. Digital defocus correction of complex-valued FF-OCT image of USAF target defocused by 1 mm. The complex-valued signal, consisting of amplitude (a) and phase (b), is Fourier-transformed (c), then multiplied by a quadratic phase function (d), and subsequently inverse Fourier-transformed, resulting in a refocused image (e). An in-focus image is provided in (f) for comparison.

Figure 3 demonstrates the digital refocusing in FF-OCT on a resolution target mounted behind a highly scattering sample. It also compares images

acquire with LED and laser, clearly showing that the latter fails to image the target because of the coherence noise dominating the image.

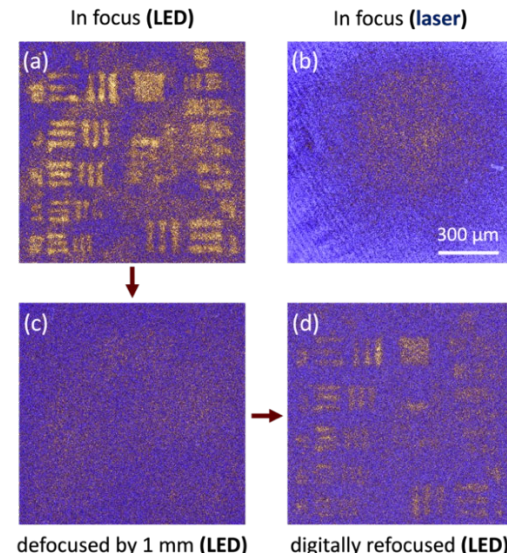


Figure 3. Digital defocus correction in FF-OCT imaging through highly scattering media: a demonstration using a USAF target beneath 400 μm of scattering material. (a) the in-focus image of USAF target. (b) the same image as in (a) but acquired with a laser. (c) the USAF target image defocused by 1 mm. (d) computationally refocused defocused USAF target.

Overall, digital defocus correction of images created with FF-OCT systems can be implemented over a much larger range than the Depth of Field (DOF). As DOF with used optics is 10 μm , defocus values up to 1 mm can be achieved although with certain spatial resolution and intensity losses [3]. Alongside the use of incoherent light sources, TD-FF-OCT holds an advantage over other holographic microscopy techniques due to reduction in the number of coherent artifacts granting an increase in imaging depth. This feature can be exploited in other important imaging scenarios, such as *in vivo* retinal imaging.

References

- [1] A. Dubois *et al.*, "Ultrahigh-resolution full-field optical coherencetomography," *Applied Optics*, vol. 43, no. 14, p. 2874, May 2004. doi:10.1364/ao.43.002874
- [2] A. Kumar, W. Drexler, and R. A. Leitgeb, "Subaperture correlation based digital adaptive optics for full field optical coherence tomography," *Optics Express*, vol. 21, no. 9, p. 10850, Apr. 2013. doi:10.1364/oe.21.010850
- [3] A. Trečiokaitė, K. Adomavičius, and E. Auksorius, "Time-domain full-field optical coherence tomography with digital defocus correction," *Optics Letters*, vol. 49, no. 10, p. 2605, Apr. 2024, doi: 10.1364/ol.520911.

STUDY OF ORGANIC BULK HETEROJUNCTION SOLAR CELLS BY KINETIC PHOTOCONDUCTIVITY METHOD

Dovilė Vasiliauskaitė, Ernestas Kasparavičius, Vidmantas Gulbinas

Fizinių ir technologijos mokslų centras, Molekulinių darinių fizikos skyrius
Saulėtekio al. 3, LT-10257 Vilnius, el. p.: dovile.vasiliauskaite@ff.stud.vu.lt

Center for Physical Sciences and Technology, Department of Molecular Compound Physics
Saulėtekio av. 3, LT-10257 Vilnius, email: dovile.vasiliauskaite@ff.stud.vu.lt

Renewable energy sources such as solar, wind and hydroelectric energy in recent years have become increasingly popular areas of research due to the global trend of moving away from fossil fuels. Solar photovoltaic systems being the most promising renewable energy source, theoretically capable of adequately satisfying energy demand worldwide [1]. Third generation organic solar cells have a great potential for a wide range of applications and cost effective production, as well as were shown to exhibit certified power conversion efficiencies up to 20.0% [4, 2]. The structure of a bulk - heterojunction organic solar cell consists of bottom and top electrodes, interfacial layers and an active layer. The active layer is a blend of two organic donor-like and acceptor-like molecules or polymers which create a *p-i-n* junction [3], while interface layers may consist of materials such as polymers or self-assembling monolayer materials (SAM) [5]. The investigation of different materials suitable for BHJ organic solar cells, most efficient device structures and their properties increasingly gain popularity as an area of academic interest.

In this work, inverted structure D18:Y6/PMMA bulk-heterojunction organic solar cells with different SAMs: 2PACz, MeO-2PACz and polymers: PEDOT:PSS, PTAA ware investigated. The goal was, using the photoconductivity

measurement method, to see how the charge carrier dynamics of the solar cell change depending on the used hole transport layer and the intensity of illumination of the cell.

References

- [1] E. Kabir, P. Kumar, S. Kumar, A. A. Adelodun, Ki-Hyun Kim, Solar energy: Potential and future prospects, Renewable and Sustainable Energy Reviews, Volume 82, Part 1, 2018.
- [2] Chen, C., Wang, L., Xia, W. et al. Molecular interaction induced dual fibrils towards organic solar cells with certified efficiency over 20%. *Nat Commun* **15**, 6865 (2024).
- [3] Takeo Oku, Chapter 17 - Fullerene-based solar cells, *Nanomaterials for Solar Cell Applications*, Elsevier, 2019.
- [4] S. Rafique, S. M. Abdullah, K. Sulaiman, M. Iwamoto, Fundamentals of bulk heterojunction organic solar cells: An overview of stability/degradation issues and strategies for improvement, *Renewable and Sustainable Energy Reviews*, Volume 84, 2018.
- [5] X. Sun, C. Zhang, Y. Yao, J. Lv, J. Yao, X. Ding, M. Lu, L. Zhu, G. Zhang, H. Lin, Y. Shi, K. Wang, C. Yang, X. Ouyang, H. Hu, I. McCulloch and Y. Lin, 19.35% Efficient Binary Bulk-Heterojunction Organic Photovoltaic Enabled by Optimizing Bromine-Substituted Self-Assembled Carbazole Based Molecules, *Advanced Functional Materials*, 2024

BIOMEDICAL IMAGING WITH NANO-FULL-FIELD OPTICAL COHERENCE TOMOGRAPHY

Austėja Trečiokaitė¹, Eriks Tarvydas¹, Karolis Adomavičius¹,
Urtė Neniškytė², Egidijus Auksorius¹

¹Center for Physical Sciences and Technology, Saulėtekio av. 3, LT-10257 Vilnius,

²Life Sciences Center, Saulėtekio av. 7, LT-10257 Vilnius

email: austeja.trecoiakite@ftmc.lt

Optical coherence tomography (OCT) is an interferometric imaging technique, widely used for imaging various biomedical samples. Most standard OCT systems typically achieve an imaging resolution of 1-10 μm axially and 3-10 μm laterally. The axial resolution of an OCT system is primarily determined by the spectral width (and thus the coherence length) of the light source. Lateral resolution, on the other hand, is determined by the numerical aperture of the objectives. Full-field (FF-) OCT can achieve higher resolution—better than 1 μm —due to a combination of factors [1,2]. Here, we demonstrate that FF-OCT can achieve a lateral resolution of 280 nm when two microscope objectives ($\times 100$) with a numerical aperture (NA) of 1.25 are employed. We call this technique nano-FF-OCT and showcase its potential for biomedical imaging of both highly reflective and scattering samples.

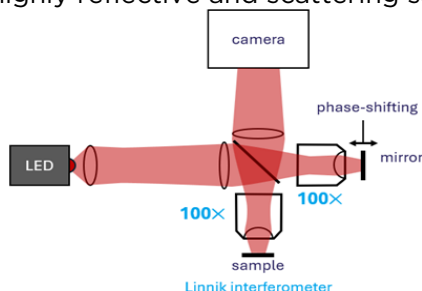


Figure 1. Principle schematics of extremely high-resolution FF-OCT system.

FF-OCT system is shown in Fig. 1, featuring Linnik interferometer with two identical objective lenses, a spatially incoherent white light source (LED) and a camera. Reference mirror is mounted on a piezo actuator to enable phase shifting.

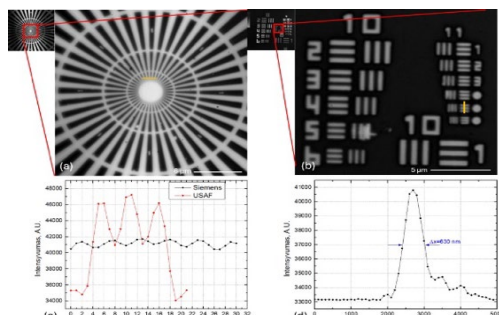


Figure 2. Nano-FF-OCT images of Siemens Star (a) and USAF (b) resolution targets showing that the system can achieve 280 nm lateral and 630 nm axial resolution. (c) illustrates intensity line profile for both targets in areas marked yellow, where the smallest imaged object measures 5 pixels (280 nm) in width. (d) – axial resolution measurement.

Fig. 2 shows resolution measurement results demonstrating that the system can achieve resolution better than 280 nm. To this end two resolution target were used to confirm the results. Figure 3 demonstrates nano-FF-OCT imaging of an ex vivo fixed mouse gut sample mounted behind a microscope coverslip. The entire thickness of the gut was imaged by axially stepping the sample in 100 nm increments.

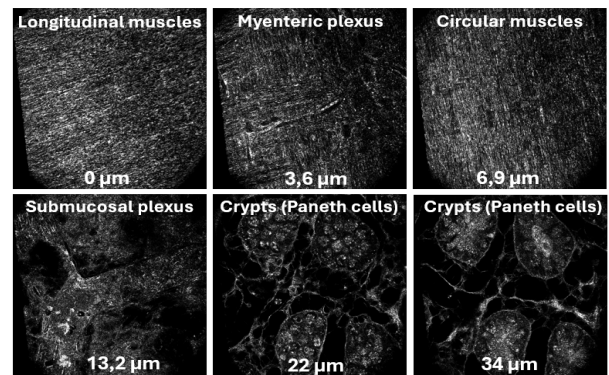


Figure 3. Nano FF-OCT images of mouse intestinal tissue at various depths beneath the sample surface. Images clearly showcase various layers in the gut.

The images reveal that various layers of the gut, including the myenteric plexus, can be successfully visualized. Overall, nano-resolution FF-OCT systems can be effectively employed for biomedical sample imaging, provided the sample is stabilized, the light source is sufficiently powerful, and the system can maintain mechanical optical path matching to prevent rapid signal degradation. Along with the use of incoherent light sources, FF-OCT offers the capability to achieve sub-micron resolution for imaging within the sample. This, when combined with digital defocus correction, can contribute to faster and more accurate diagnostics [3].

References

- [1] A. Dubois, K. Grieve, G. Moneron, R. Lequeux, L. Vabre, and C. Boccara, "Ultrahigh-resolution full-field optical coherence tomography," *Applied Optics*, vol. 43, no. 14, p. 2874, May 2004, doi: 10.1364/ao.43.002874.
- [2] T. Monfort et al., "Dynamic full-field optical coherence tomography module adapted to commercial microscopes allows longitudinal in vitro cell culture study," *Communications Biology*, vol. 6, no. 1, Sep. 2023, doi: 10.1038/s42003-023-05378-w.
- [3] A. Trečiokaitė, K. Adomavičius, and E. Auksorius, "Time-domain full-field optical coherence tomography with digital defocus correction," *Optics Letters*, vol. 49, no. 10, p. 2605, Apr. 2024, doi: 10.1364/ol.520911.

PALLADIUM-MODIFIED COBALT-PHOSPHORUS AND COBALT-IRON-PHOSPHORUS COATINGS FOR OXYGEN EVOLUTION REACTION

A. Degollado-Vasalauskas^{1,2}, H. Amber¹, A. Balčiūnaitė¹, L. Tamašauskaitė-Tamašiūnaitė¹, Z. Sukackienė¹, D. Šimkūnaitė¹, J. Vaičiūnienė¹, E. Norkus¹

¹Department of Catalysis, Center for Physical Sciences and Technology (FTMC), Sauletekio Ave. 3, LT-10257 Vilnius

²Faculty of Mechanical Engineering and Design, Kaunas University of Technology, Students st. 56, Kaunas

This study presents the fabrication of palladium-modified cobalt-phosphorus (Pd-CoP) and cobalt-iron-phosphorus (Pd-CoFeP) coatings deposited on the copper surface by the electroless metal plating, followed by their modification with Pd crystallites, and their application for oxygen evolution (OER). The morphology, structure, and composition of the resulting catalytic materials were characterized using scanning electron microscopy (SEM, Fig. 1), energy dispersive X-ray spectroscopy, X-ray diffraction, and inductively coupled plasma optical emission spectroscopy, while the electrocatalytic activity of the catalysts for the OER in an alkaline medium was studied using linear sweep voltammetry (LSV). The OER data for the CoP, CoFeP, Pd-CoP, and Pd-CoFeP catalysts are presented. It was found that the incorporation of Fe into the CoP coating significantly increased its activity for OER (Fig. 2). In addition, the Pd modified CoFeP also shows higher activity for OER compared to Pd-CoP (Fig. 2). The CoFeP catalyst demonstrated the most

promising properties for OER.

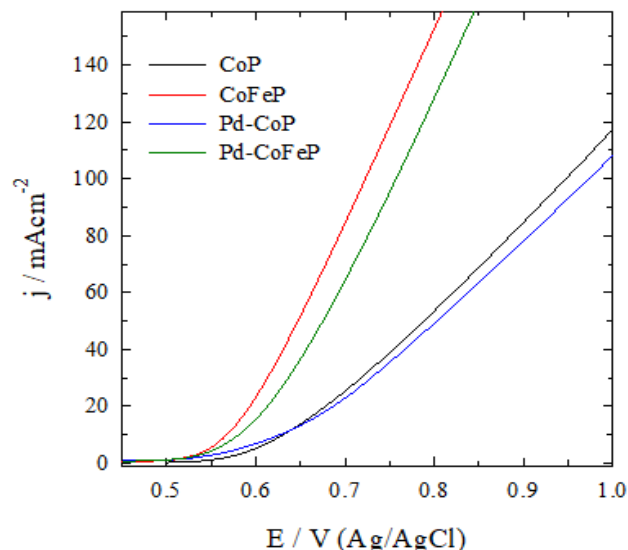


Fig. 2. The OER polarization curves recorded on CoP, Pd-CoP, CoFeP and Pd-CoFeP catalysts in 1 M KOH at 5 mV s⁻¹ and a temperature of 25°C.

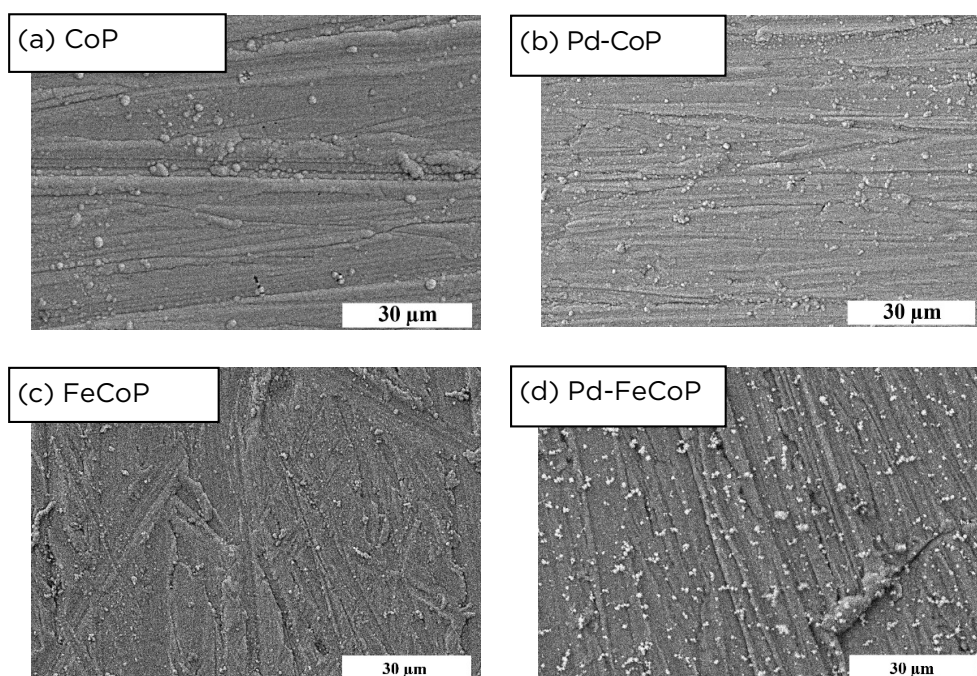


Fig. 1. The SEM views of CoP (a), Pd-CoP (b), CoFeP (c) and Pd-CoFeP (d) catalysts.

HYDROGEN AND OXYGEN EVOLUTION ON NICKEL-IRON COATINGS

Dmytro Shyshkin^{1,2}, Loreta Tamašauskaitė-Tamašiūnaitė¹

¹Center for Physical Sciences and Technology, Department of Catalysis
Saulėtekio av. 3, LT-10257 Vilnius, email: dmytro.shyshkin@ftmc.lt

²Vilnius University, Faculty of Chemistry and Geosciences
Naugarduko st. 24, LT-01513 Vilnius, email: dmytro.shyshkin@fchgf.stud.vu.lt

The production of hydrogen by electrolysis of water is now considered a promising and sustainable, carbon-neutral way to produce clean hydrogen for use as a feedstock, fuel and energy carrier. Electrolysis is the process of splitting water (H_2O) into oxygen (O_2) and hydrogen (H_2) by passing an electric current through the water. The focus is on the search for efficient and low-cost anode/cathode materials with high activity for hydrogen and oxygen evolution reactions (HER and OER). In this study, we investigate the deposition conditions of nickel-iron (NiFe) binary alloy coatings using low-cost and simple electroless metal deposition with morpholine borane (MB, $C_4H_8ONH \cdot BH_3$) as a reducing agent, with the aim of using them as anode/cathode catalysts for hydrogen production by water splitting. The morphology, structure, and composition of NiFe/Cu catalysts were investigated by scanning electron microscopy (SEM), energy dispersive X-ray spectroscopy (EDX), X-ray diffraction (XRD), and inductively coupled plasma optical emission spectroscopy (ICP-OES).

It has been determined that $Ni_{90}Fe_{10}$, $Ni_{80}Fe_{20}$, $Ni_{60}Fe_{40}$, and $Ni_{30}Fe_{70}$ coatings were deposited on the Cu surface, then the concentration of Fe^{2+} in the plating solution was 0.5 mM, 1 mM, 5 mM, and 10 mM, respectively. The deposition rate for the $Ni_{90}Fe_{10}$, $Ni_{80}Fe_{20}$, $Ni_{60}Fe_{40}$, and $Ni_{30}Fe_{70}$ coatings was approximately 2.6, 3.6, 1.1, and 1.4 $mg\ cm^{-2}\ h^{-1}$, respectively. It was found that nickel-iron produces a layer of granular nickel-iron particles up to two hundred nanometers in size. XRD analysis confirms the deposition of NiFe alloys. Hydrogen and oxygen evolution was investigated on the obtained catalysts in N_2 -de aerated 1 M KOH solution (Figs. 1 and 2).

The lowest onset potential (E_{onset}) of -0.0928 V exhibits the $Ni_{80}Fe_{20}$ catalyst compared to the $Ni_{90}Fe_{10}$, $Ni_{30}Fe_{70}$, and $Ni_{60}Fe_{40}$. In addition, this catalyst shows the highest current density at -0.45 V (Fig. 1). It was found that the $Ni_{80}Fe_{20}$ /Cu catalyst exhibited the lowest overpotential value of -202.7 mV for the HER to obtain a current density of 10 mA cm⁻² compared to $Ni_{90}Fe_{10}$ /Cu (-211.9 mV), $Ni_{60}Fe_{40}$ /Cu (-276.3 mV), $Ni_{30}Fe_{70}$ /Cu (-278.4 mV), and Ni (-303.4 mV).

The most promising composition of NiFe is Ni 80 at.% and Fe 20 at.% for efficient HER.

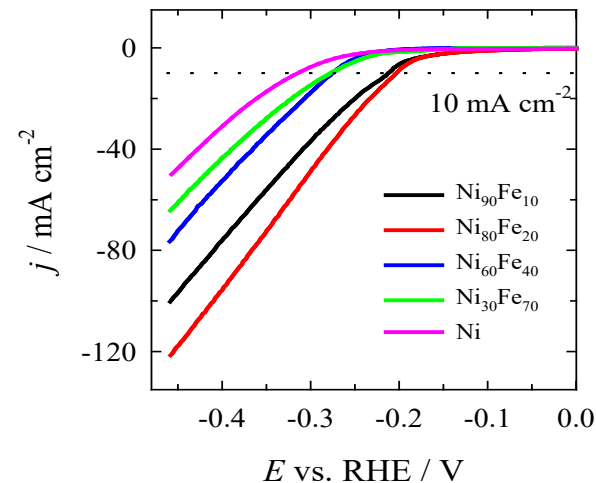


Fig. 1. HER polarization curves of Ni, $Ni_{90}Fe_{10}$, $Ni_{80}Fe_{20}$, $Ni_{60}Fe_{40}$, and $Ni_{30}Fe_{70}$ catalysts in N_2 -saturated 1 M KOH solution at a potential scan rate of $2\ mV\ s^{-1}$.

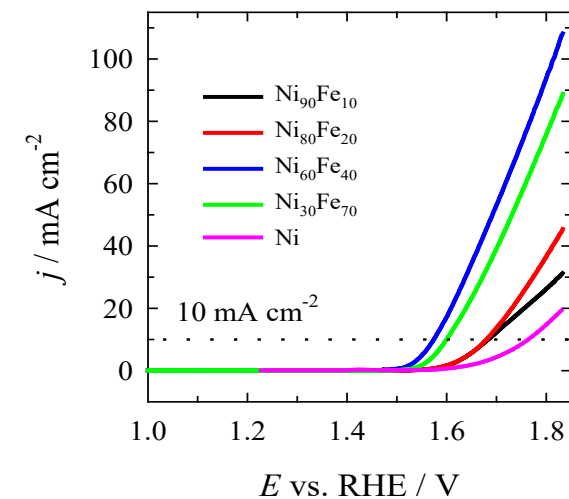


Fig. 2. OER polarization curves of $Ni_{90}Fe_{10}$, $Ni_{80}Fe_{20}$, $Ni_{60}Fe_{40}$, and $Ni_{30}Fe_{70}$ catalysts in N_2 -saturated 1 M KOH solution at a potential scan rate of $2\ mV\ s^{-1}$.

The lowest OER overpotential (344.7 mV) was observed for the $Ni_{60}Fe_{40}$ /Cu catalyst to obtain a current density of $10\ mA\ cm^{-2}$ as compared with the $Ni_{30}Fe_{70}$ /Cu catalyst (369.9 mV), $Ni_{80}Fe_{20}$ /Cu (450.2 mV), $Ni_{90}Fe_{10}$ /Cu (454.2 mV), and Ni (532.1 mV).

The obtained catalysts seem to be suitable flexible catalysts for HER and OER in alkaline media.

DI-TERT-ALKYLPHOSPHINE SYNTHESIS AND INVESTIGATION OF CHEMOENZYMIC REACTIONS OF THEIR PRECURSORS - TERTIARY ACETATES

Jonas Paukštys^{1,2,3}, Tomas Paškevičius¹, Ringailė Lapinskaite¹,
Nina Urbelienė², Linas Labanauskas¹, Rolandas Meškys²

¹Department of Organic Chemistry, Center for Physical Sciences and Technology,
Akademijos st. 7 LT-08412 Vilnius

²Department of Molecular Microbiology and Biotechnology, Institute of Biochemistry,
Life Sciences Centre, Vilnius University, Saulėtekio Ave 7, LT-10257 Vilnius

³Faculty of Chemistry and Geosciences, Vilnius University, Naugarduko st. 24, LT-03225 Vilnius

e-mail: jonas.paukstys@gmc.stud.vu.lt

Sterically hindered phosphine ligands are an essential part of transition metal catalysis in organic chemistry.¹ In particular, di-tert-alkyl phosphines serve as building blocks for these ligands. However, their synthesis remains cumbersome, involving highly reactive and hazardous reagents along with non-trivial laboratory techniques.^{2,3}

In an attempt to simplify this synthesis, we developed a new method for the preparation of di-tert-alkyl phosphonium triflate salts. In our approach phosphine nucleophile is generated from $\text{P}(\text{TMS})_3$ which reacts in an umpolung (P^-/C^+) manner with tertiary acetates to produce di-tert-alkyl phosphine triflates. Furthermore, final products are easily isolatable and air-stable, easing further ligand synthesis.



In recent years chemoenzymatic synthesis has proved to be a greener alternative to chemical synthesis in a lot of instances. Despite this, tertiary acetates are currently synthesized exclusively chemically, as only a small number of enzymes capable of recognizing tertiary acetates as substrates have been identified.⁵

Since the enzymatic esterification reaction is reversible, in this work various esterases were successfully tested in tertiary acetate hydrolysis reactions providing more insight in this limited area of research.



References

- Surry D.S.; Buchwald S.L. Biaryl phosphane ligands in palladium-catalyzed amination. *Angew Chem Int Ed Engl.* 2008;47(34),6338-61.
- Kendall, Alexander J.; Tyler, David R. (2015). The synthesis of heteroleptic phosphines. *Dalton Trans.*, 44(28), 12473-12483.
- Thomas Barber, Stephen P. Argent, and Liam T. Ball Expanding Ligand Space: Preparation, Characterization, and Synthetic Applications of Air Stable, Odorless Di-tert-alkylphosphine Surrogates *ACS Catalysis* 2020, 10 (10), 5454-5461.
- Roddan R.; Carter E.M.; Thair B.; Hailes H.C. Chemoenzymatic approaches to plant natural product inspired compounds. *Nat Prod Rep.* 2022, 39 (7),1375-1382.
- Hari Krishna, S.; Persson, M.; Bornscheuer, U. T. Enantioselective Transesterification of a Tertiary Alcohol by Lipase *a* from *Candida Antarctica*. *Tetrahedron: Asymmetry* 2002, 13 (24), 2693-2696.

STRUCTURED LIGHT BEAM SHAPING FOR TERAHERTZ IMAGING SYSTEM OPTIMIZATION

Kasparas Stanaitis^{1,2}, Augustė Bielevičiūtė¹, Karolis Redeckas¹, Linas Minkevičius¹

¹ Center for Physical Sciences and Technology, Department of Optoelectronics
Saulėtekio av. 3, LT-10257 Vilnius, email: kasparas.stanaitis@ftmc.lt

² Vilnius University, Faculty of Physics
Saulėtekio av. 9, LT-10222 Vilnius

Terahertz photonics is a rapidly developing optoelectronics area with an ability to penetrate dielectric materials. This enables detailed material and object analysis in the frequency range of 0.1 THz - 10 THz [1]. Traditional THz systems rely on Gaussian beam-forming components, where radiation is focused into a single spot. However, these systems are difficult to align and there is a lack of innovative optical component applications that could expand their capabilities. Here structured light components such as Airy and Bessel lenses come into the spotlight offering potential imaging system contrast improvements [2,3].

In this research THz structured light components were manufactured, characterized and employed in an imaging system. 3D printing method allowed to create highly customizable and easy-to-obtain optical components. Characterization showed the successful operation of the lenses, where for Gaussian lens the radiation was focused in one spot, Bessel lens created uniform light distribution along optical lenses, and Airy radiation had a parabolic trajectory. For imaging evaluation, three aforementioned lenses were arranged in different combinations for THz focusing and collection from object plane [Figure 1. a)].

It became evident, that Gaussian lenses are still the way to go in order to achieve the best contrast [Figure 1. b)]. Additionally, by using structured light components to collect the radiation, the image contrast was not affected greatly [Figure 1. b)], but such compositions allow for a system to be less sensitive for misalignments. For radiation focusing, structured light components were found out to not be as effective contrast-wise [Figure 1. b)], but the objects can still be distinguished, meaning such composition can still be used for detection and have the all benefits of structured light.

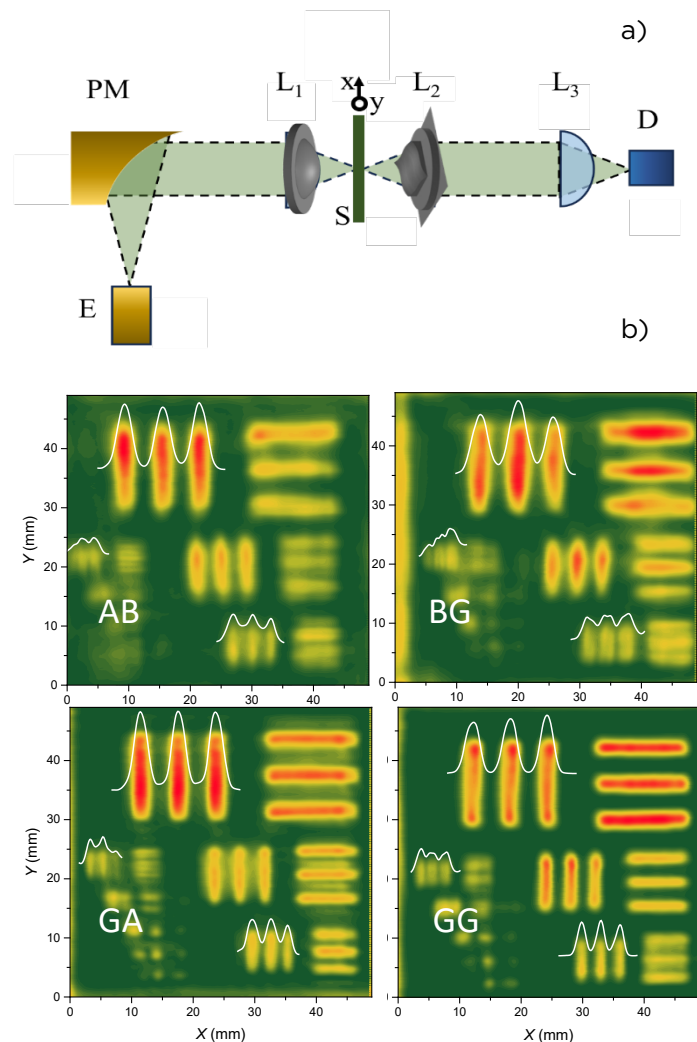


Figure 1. a) Measurement set-up: E – 253GHz CMOS emitter, PM – parabolic mirror, L – lenses, S – sample, D – CMOS detector (Colpitts oscillator) b) contrast evaluation for different lens combinations (two letters denote focusing and collecting lens respectively).

References

1. Valušis, G., et al. Sensors, **21**, 12 (2021).
2. Ivaškevičiūtė-Povilauskienė, R. et al. Light: Science & Applications, **11**, 1, (2022).
3. Orlov, S. et al, Laser & Photonics Reviews, **23**01197 (2024).

THZ METALENS DEVELOPMENT AND APPLICATION FOR OBJECT IMAGING

Karolis Redeckas^{1,2}, Kaspras Stanaitis^{1,2}, Vladislovas Čižas¹,
Rusnė Ivaškevičiute-Povilauskienė¹ and Linas Minkevičius¹

Center for Physical Sciences and Technology, Department of Optoelectronics
Saulėtekio av. 3, LT-10257 Vilnius, email: karolis.redeckas@ftmc.lt

Terahertz (THz) radiation consists of electromagnetic waves in the mm- μ m range, within the 0.1-10 THz spectrum [1]. It is low-energy, non-ionizing radiation, and its generation and detection rely on electronics and photonics methods due to its unique spectral position [2]. A key advantage of THz radiation is its ability to penetrate materials like paper, rubber, plastic, and textiles, enabling applications in security, manufacturing quality control, biological tissue analysis, and imaging [3]. Traditional THz imaging systems are bulky and costly, but miniaturization using flat diffractive optics and metamaterials has led to metalenses. These lenses, incorporating complementary split-ring resonators (CSRR), can focus light and rotate polarization [4][5].

This research focused on developing innovative 250 GHz metalens designs, followed by functionality testing, characterization, and integration into an imaging system. The design combines traditional Fresnel multi-step zone plate geometries with CSRR metaatoms of different sizes to provide the necessary phase delay for the lens. Suitable CSRR metaatoms were identified through numerical frequency-domain simulations using the CST Studio Suite with the EM Studio package, where different sizes and geometrical parameters were tested. Four CSRR combinations were selected for implementation in two- and four-zone diffractive lens geometries. The key feature of these combinations is the high transmission at 250 GHz and the coordinated phase delay, ensuring constructive interference at the lens focus.

The designed and simulated metalenses were manufactured using laser ablation technology [5] and experimentally characterized. The detected signal values along the optical axis and in the focal plane (Fig. 1) demonstrate the real focusing capabilities of the metalenses. The metalens of design D2 exhibited excellent focusing characteristics for rotated polarization ($F=30\text{mm}$, $\text{FWHM}_z=7.6\text{ mm}$; $\text{FWHM}_x=1.54\text{ mm}$). Metalens bending influence was also investigated. The uniaxial bending of the metalens was performed using a specially 3D-printed holder. The bending was measured by the ratio of the bent to flat metalens diameter, I/D . As this value decreases (i.e., as bending increases), the beam's focal width grows, and intensity decreases (Fig. 2).

Due to small focal spot achievable with D2 metalens, it was applied for object imaging. Results show that D2 is suitable for object imaging and achieves a resolution of 0.63λ .

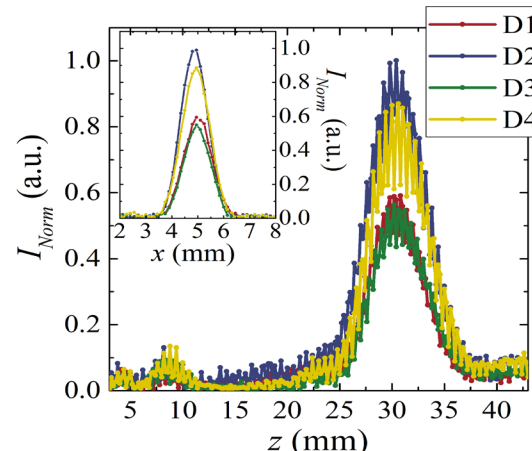


Fig. 1. Experimentally measured 1D images of the focused beam by the D1, D2, D3, and D4 design metaleenses were experimentally measured along the optical axis and in the focal plane.

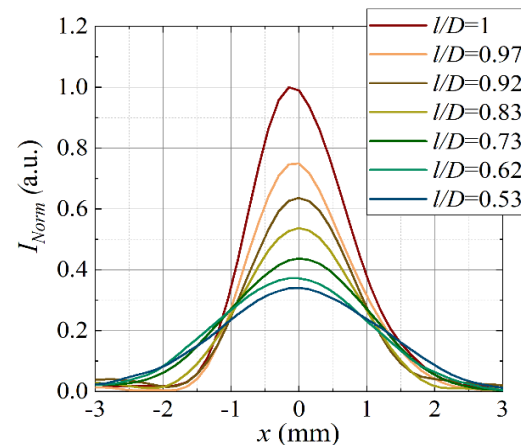


Fig. 2. Bending influence to intensity in focal point of D2 metalens. Bent ratio is I/D .

References

1. Nagatsuma, T., IEICE Electronics Express, 2011, 8, pp. 1127-1142.
2. Leitenstorfer, A., Moskalenko, A., et al., J. Phys. D: Appl. Phys., 2023, 56, pp. 223001.
3. Mittleman, D. M., Optics Express, 2018, 26, pp. 9417-9431.
4. Valušis, G., Lisauskas, A., et al., Sensors, 2021, 21(12), p. 4092.
5. Ivaškevičiūtė-Povilauskienė, R., Čižas, V., et al., Front. Phys., 2023, 11, 1196726.

SURFACE ROUGHNESS DEPENDENCE ON SPECIMEN POSITIONING

Danielius Ragoža, Ada Steponavičiūtė, Genrik Mordas

Center for Physical Sciences and Technology, Department of Laser Technologies
Saulėtekio av. 3, LT-10257 Vilnius, email: danieliusrag@gmail.com

Additive manufacturing (AM) is a novel technique intended for the production of 3D objects as it is possible to make complicated geometrical shaped components [1]. Of all the metal AM methods, Direct Metal Laser Sintering (DMLS) is the most widely used. DMLS employs metal powders that are selectively sintered and fused, layer upon layer, with the aid of a laser beam to fabricate objects [2]. Although many of the metals and alloys can be used, it is still difficult to achieve reliable and high standards with iron alloys. One of the other challenges confronted in DMLS is the management of energy density to determine porosity, microstructure and fabrication materials properties. In addition, incorrect specimen location can appreciably lessen the part quality particularly the surface quality.

This work considers the role of specimen placement on the surface finish of 17-4PH stainless steel parts produced using an EOSINT M280 machine. The relation between specimen

positions on the build platform and printed part surface qualities in terms of surface roughness was observed through the use of an optical profiler.

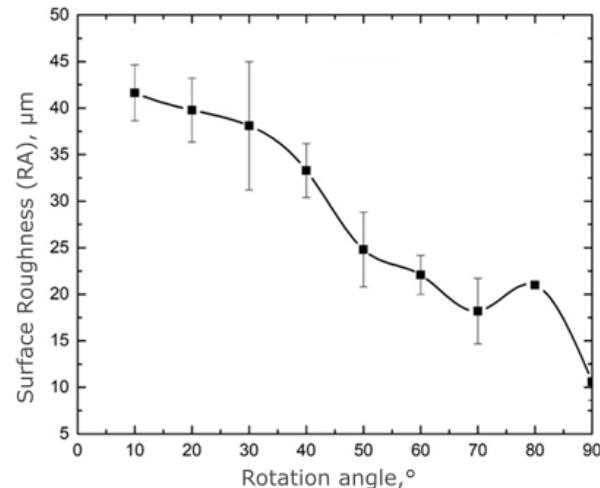


Fig. 1. Influence of specimen positioning angle on specimen top surface roughness.

References

1. O.Abdulhameed, A. Al-Ahmari, et al., Additive manufacturing: Challenges, trends, and applications (2019).
2. T.Peng, C. Chen, Influence of energy density on energy demand and porosity of 316L stainless steel fabricated by selective laser melting (2018).

AZURE A AND METHYLENE BLUE DYES REMOVAL USING ADSORPTION METHOD AND MXene NANOSTRUCTURES

Germantė Paulikaitė¹, Martynas Talaikis², Gediminas Niaura², Simona Ramanavičius²

¹Departament of Physical Chemistry, Vilnius University Faculty of Chemistry and Geoscience,
Naugarduko g. 24, 03225 Vilnius, email: germante.paulikaite@chgf.stud.vu.lt

²Center for Physical Sciences and Technology, Department of Organic Chemistry,
Saulėtekio av. 3, LT-10257 Vilnius

MXenes are new generation 2D material class which were discovered at Drexler University in 2011 and have huge scientific attraction due to unique plasmonic, hydrophilic, electrical and mechanical properties [1]. Moreover, these nanostructures possess unique and complex surface chemistry resulting in distinctive properties and applications.

The first and most studied MXene structure is $T_3C_2T_x$. Synthesis method includes selective etching method using HF acid and Ti_3AlC_2 precursor. By possessing this synthesis methodology sheet-like structure is obtained which is favourable by being most stable in various conditions and wide range us practical use.

MXenes are being studied both for their distinctive properties and for their potential use in a variety of applications. Nowadays MXenes are applied in Raman spectroscopy [2], biofuel elements [3], lithium and sodium ions batteries [4], and many other applications. Considering complex MXene surface and interaction with other organic molecules these structures are highly adaptable in adsorbents and wide range of sensors technologies. There is a growing body of research dedicated to creating diverse surface plasmon resonance sensors by leveraging the plasmonic properties of MXenes.

In this study, large surface area MXene nanostructures were obtained by using Ti_3AlC_2 precursor and selective etching in concentrated HF acid resulting in advantageous molecular interaction with other molecules. Methylene Blue and Azure A were chosen as model molecules to investigate interaction with MXenes. Because MXenes are highly effective at cation adsorption in aqueous solutions, a study was carried out using constant sodium ion concentration solution at a pH range of 3-6. This created steady conditions and resulted in changes in adsorption capacity that are related to pH levels. For adsorption capacity evaluation – spectrophotometric method was used to indicate Methylene Blue and Azure A absorption intensity peak change (Fig. 1).

It was determined that MXenes surface obtained by selective etching with HF acid is highly suitable for organic molecules adsorption. This feature cab be extensively utilized in different kinds of sensors and water treatment technologies.

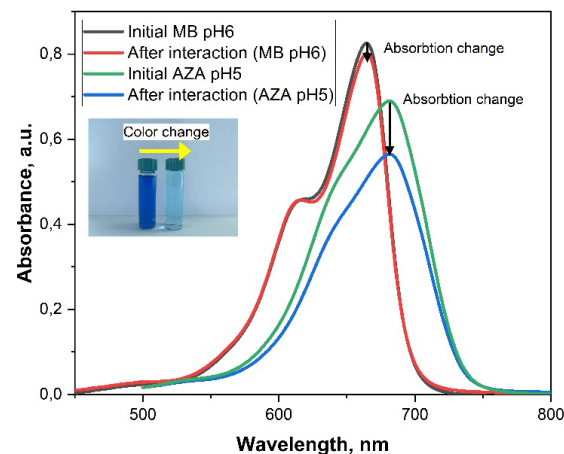


Fig. 1. Visible light absorption of Methylene Blue and Azure A before and after interaction with MXenes.

This project has received funding from the Research Council of Lithuania (LMTLT), agreement No. S-MIP-24-14.

References

- [1] Gogotsi Y, Anasori B. The Rise of MXenes. ACS Nano 2019; 13:8491-4. <https://doi.org/10.1021/acsnano.9b06394>.
- [2] Adomavičiūtė-Grabusovė S, Ramanavičius S, Popov A, Šablinskas V, Gogotsi O, Ramanavičius A. Selective enhancement of SERS spectral bands of salicylic acid adsorbate on 2D Ti_3C_2Tx -based MXene film. Chemosensors 2021; 9:223.
- [3] Ramanavicius S, Ramanavicius A. Progress and Insights in the Application of MXenes as New 2D Nano-Materials Suitable for Biosensors and Biofuel Cell Design. Int J Mol Sci 2020;21. <https://doi.org/10.3390/ijms21239224>.
- [4] Li X, Huang Z, Shuck CE, Liang G, Gogotsi Y, Zhi C. MXene chemistry, electrochemistry and energy storage applications. Nat Rev Chem 2022; 6:389-404. <https://doi.org/10.1038/s41570-022-00384-8>.

